Instytut Immunologii i Terapii Doświadczalnej im. Ludwika Hirszfelda Polskiej Akademii Nauk

ROZPRAWA DOKTORSKA

Wpływ białek transportowych na farmakokinetykę i efektywność fotodynamiczną pochodnych chlorofilu

Impact of transport proteins on pharmacokinetics and photodynamic efficacy of chlorophyll derivatives

Milena Julia Szafraniec

Promotor: dr hab. Łukasz Łaczmański

Wrocław, 2022

Spis treści

Wykaz publikacji wchodzących w skład osiągnięcia naukowego:

1. **Milena J. Szafraniec**, Leszek Fiedor. One ring is not enough to rule them all. Albumin-dependent ABCG2-mediated transport of chlorophyll-derived photosensitizers.
   European Journal of Pharmaceutical Sciences 167 (2021), 106001
   https://doi.org/10.1016/j.ejps.2021.106001
   IF = 4,38; 100 pkt. MEiN; 90% udziału

2. **Milena J. Szafraniec**. Interactions of chlorophyll-derived photosensitizers with human serum albumin are determined by the central metal ion.
   Journal of Biomolecular Structure and Dynamics (2021)
   https://doi.org/10.1080/07391102.2021.2007794
   IF = 3,39; 70 pkt. MEiN

3. **Milena J. Szafraniec**, Monika Toporkiewicz, Andrzej Gamian. Zinc-substituted pheophorbide a is a safe and efficient antivascular photodynamic agent.
   Pharmaceuticals 15 (2022), 235
   https://doi.org/ 10.3390/ph15020235
   IF = 5,86; 100 pkt. MEiN; 85% udziału

Publikacje powstały w ramach projektu Preludium pt. "Rola transporterów ksenobiotyków w odpowiedzi na efekt fotodynamiczny z udziałem pochodnych chlorofilu" finansowanego przez Narodowe Centrum Nauki, a zrealizowanego w Sieci Badawczej Łukasiewicz – PORT Polskim ośrodku Rozwoju Technologii we Wrocławiu.

I. Wstęp

1. Terapia fotodynamiczna

Terapia fotodynamiczna jest metodą leczenia szeregu schorzeń, m.in. litych guzów nowotworowych (rak skóry, piersi, głowy i szyi, prostaty, przewodu pokarmowego, płuc), zmian dermatologicznych (np. trądzik pospolity, łuszczyca, brodawczak wirusowy, rogowacenie słoneczne), malformacji naczyniowych, chorób oczu (neowaskularyzacja naczyniówki, zwyrodnienie plamki żółtej), a także infekcji bakteryjnych grzybiczych i wirusowych [1–6]. Polega ona na miejscowym lub systemowym podaniu pacjentowi światłoczułej substancji nazywanej fotouczulaczem (fotosensybilizatorem), a następnie miejscowym naświetleniu światłem o odpowiedniej długości fali (światło czerwone lub bliska podczerwień). Naświetlenie to, pod warunkiem obecności tlenu w środowisku, doprowadza do inicjacji przez fotouczulacz szeregu reakcji wolnorodnikowych, na skutek których dochodzi do zniszczenia chorej tkanki [1,7,8]. Zaletą tego typu terapii jest wysoka selektywność (ze względu na miejscowe naświetlanie, a czasem również selektywną akumulację fotouczulacza) minimalna toksyczność ogólnoustrojowa, bezbolesność oraz dobry efekt kosmetyczny.

Wzbudzony światłem fotouczulacz może ulec dwóm typom reakcji fotodynamicznej. W warunkach niskiego stężenia tlenu w otaczającym środowisku wymienia on elektrony bezpośrednio z otaczającymi go biomolekułami, co prowadzi do wytworzenia ich form wolnorodnikowych (reakcja fotodynamiczna typu I). Te z kolei, reagując z tlenem, generują wolne rodniki tlenowe, tj. anionorodnik ponadtlenkowy, rodnik wodoronadtlenkowy oraz rodnik hydroksylowy. W reakcji typu II fotouczulacz znajdujący się w stanie singletowym wzbudzonym przechodzi do stanu trypletowego (przejście międzysystemowe), w którym z łatwością reaguje z tlenem cząsteczkowym, co prowadzi do powstania wysoce reaktywnego tlenu singletowego. Formy tlenu powstałe w obu typach reakcji są bardzo aktywnymi utleniaczami, które reagując z nienasyconymi kwasami tłuszczowymi, zasadami azotowymi i cukrami w kwasach nukleinowych oraz resztami aminokwasowymi (Cys, Met, Tyr, His, Trp) w białkach , doprowadzają do destrukcji tkanek [9,10]. Uważa się, w przypadku większości stosowanych obecnie fotouczulaczy przeważa mechanizm reakcji fotodynamicznej typu II [11,12].

Rodzaj fotouczulacza zastosowany w terapii fotodynamicznej jest kluczowym czynnikiem decydującym o jej powodzeniu. Idealny fotouczulacz to substancja cechująca

się: 1) czystością chemiczną, 2) dobrą rozpuszczalnością w wodzie, 3) silną absorpcją światła w tzw. oknie terapeutycznym (600 – 800 nm), 4) wysoką wydajnością generacji reaktywnych form tlenu, 5) brakiem toksyczności ciemnej, 6) brakiem niepożądanej fototoksyczności wobec skóry, oczu i błon śluzowych, 7) stabilnością i łatwością przechowywania, 8) selektywnością akumulacji.

Funkcję fotouczulaczy mogą pełnić związki o różnorodnej strukturze, najczęściej jednak są to nienasycone, skoniugowane układy heterocykliczne, takie jak tetrapirole (porfiryny, chloryny, ftalocyjaniny), barwniki syntetyczne (błękit metylenowy, róż bengalski) lub naturalne (hiperycyna, kurkumina) [13,14]. Tradycyjne fotouczulacze porfirynowe, opracowane w latach 70 – 80. XX wieku, określa się mianem fotouczulaczy I generacji. Należy do nich pierwszy zaakceptowany przez amerykańską Agencję ds. Żywności i Leków (FDA) i stosowany obecnie w praktyce klinicznej Photofrin®. Stanowi on mieszaninę kilkudziesięciu związków makrocyklicznych z grupy porfiryn. Lek ten posiada szereg wad, do których należą: słaba absorpcja światła, aktywacja w obszarze widma słabo penetrującym tkankę, oraz długo utrzymującą się nadwrażliwość pacjenta na światło [15]. Z powodu tych ograniczeń stale poszukuje się fotouczulaczy o lepszych właściwościach (fotouczulacze II generacji). Fotouczulacze II generacji cechują się ściśle określonym składem chemicznym, korzystniejszymi własnościami spektralnymi oraz wyższą preferencyjnością lokalizacji w porównaniu z fotouczulaczami I generacji [16]. Wiele fotouczulaczy II generacji jest obecnie zaakceptowanych do użytku w praktyce klinicznej, m.in. w terapii nowotworów głowy i szyi (Foscan®, Photochlor®), zmian skórnych (Levulan®, Metvix®) oraz zwyrodnienia plamki żółtej (Visudyne®) [16]. Pracuje się także nad fotouczulaczami III generacji, stanowiącymi koniugaty fotouczulaczy II generacji z innymi cząstkami np. przeciwciałami, węglowodanami, aminokwasami, peptydami lub też poddanymi enkapsulacji w nośnikach np. liposomach, micelach czy nanocząstkach [13]. Takie modyfikacje mają na celu zwiększenie ich biodostępności oraz specyficzności akumulacji.

1. 1 Pochodne chlorofilu jako fotouczulacze

Mimo zdolności do wywołania efektu fotodynamicznego, chlorofile i bakteriochlorofile, ze względu na nierozpuszczalność w wodzie oraz niską stabilność, nie nadają się do zastosowań farmaceutycznych. Stanowią one jednak dobre substraty do syntezy fotouczulaczy o lepszych właściwościach [17]. Jedna z pochodnych bakteriochlorofili, palladowy bakteriofeoforbid została już zaakceptowana do użytku w wielu krajach pod handlową nazwą TOOKAD®. Stosowana jest ona w terapii nowotworów prostaty z grupy niskiego ryzyka [18]. Inny związek z tej grupy, 2-[1-heksyloksyetylo]-2-dewinylo-pirofeoforbid-a (HPPH, Photochlor®) jest obecnie poddawany badaniom klinicznym (faza I lub II w zależności od jednostki chorobowej) pod kątem zastosowania w terapii fotodynamicznej nowotworów i stanów przednowotworowych głowy i szyi oraz niedrobnokomórkowego raka płuc [19–21].

Obiecującymi fotouczulaczami są także podstawione metalami pochodne chlorofilu a: chlorofilid oraz cynkowy feoforbid. Ten pierwszy otrzymuje się z chlorofilu a w reakcji hydrolizy katalizowanej przez enzym chlorofilazę, która prowadzi do usunięcia silnie hydrofobowego podstawnika fitylowego z pozycji $C-17^3$ (Rys. 1) [17].
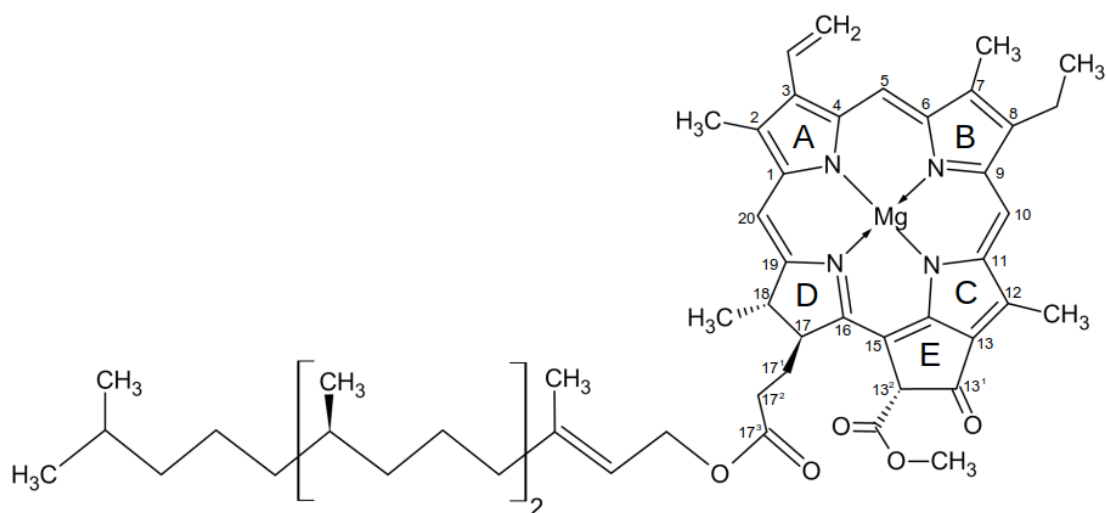
Rys. 1 Struktura cząsteczki chlorofilu a

Chlorofilid a można poddawać dalszym modyfikacjom, np. sprzęganiu z peptydami lub hormonami zwiększającymi selektywność ich akumulacji [22]. Można także usunąć w

środowisku kwaśnym centralny jon magnezu (produktem reakcji jest feoforbid a), a następnie zastąpić go jonem innego metalu, np. cynku, otrzymując cynkowy feoforbid a [23]. W porównaniu z chlorofilidem, feoforbid cynkowy cechuje się wyższą stabilnością, a także wyższą preferencyjnością lokalizacji w guzach nowotworowych (prawdopodobnie ze względu na silniejsze wiązanie z białkami) [24]. Zarówno chlorofilid a, jak i cynkowy feoforbid a posiadają wiele cech idealnych fotouczulaczy: cechują się niską toksycznością ciemną, długim czasem życia stanu trypletowego oraz silną absorpcją światła w regionie bliskiej podczerwieni, pokrywającym się z tzw. oknem terapeutycznym tkanek ludzkich [23,25]. Ponadto wykazują one silną fluorescencję, która umożliwia aplikację precyzyjnie odmierzonej dawki, a nawet ich detekcję *in vivo* [25].

Pozbawiona metalu centralnego pochodna chlorofilu jaką jest feoforbid a również wykazuje własności fotouczulające, jednakże w porównaniu z pochodnymi podstawionymi metalami cechuje się on niższym współczynnikiem absorpcji przy 660 nm oraz słabszą rozpuszczalnością w wodzie. Zaletą jego jest natomiast stosunkowo wysoka stabilność, zarówno w ciemności, jak i w obecności światła [17,26].

2. Oporność wielolekowa

Jedną z głównych przyczyn niskiej skuteczności chemioterapii przeciwnowotworowych jest tzw. zjawisko oporności wielolekowej, za którą odpowiada w dużej mierze aktywność błonowych białek transportowych z nadrodziny ABC (ang. ATP-Binding Casette). Białka te aktywnie usuwają z komórek leki wbrew gradientowi ich stężeń, przeciwdziałając w ten sposób ich akumulacji w stężeniach umożliwiających efektywne działanie. Nadrodzina ABC stanowi dużą grupę szeroko rozpowszechnionych w świecie żywym białek o wysoce konserwatywnej strukturze. Wszystkie transportery ABC wyposażone są w domenę wiążącą ATP i przeprowadzająca jego hydrolizę oraz w domenę transbłonową, której struktura decyduje o specyficzności substratowej białka [27]. Głównymi transporterami przyczyniającymi się do wystąpienia oporności wielolekowej u ludzi są: glikoproteina P (P-gp), białko oporności wielolekowej 1 (MRP1) oraz białko oporności raka piersi (ang. Breast Cancer Resistance Protein, BCRP) [28].

Ponieważ fotouczulacze, podobnie jak chemioterapeutyki, mogą być substratami transporterów przyczyniających się do oporności wielolekowej, zjawisko to dotyczy również terapii fotodynamicznej. Szczególnie istotna z punktu widzenia tej terapii wydaje

się być aktywność białka BCRP, jako transportera rozpoznającego i usuwającego z komórek związki o strukturze porfiryn i chloryn [29–32]. Białko BCRP (ABCG2) należy do rodziny G nadrodziny ABC. Jest ono tzw. półtransporterem, co oznacza że pojedyncza jego cząsteczka zawiera tylko jedną domenę transbłonową i jedną wiążącą ATP, dlatego do funkcjonowania wymaga dimeryzacji lub oligomeryzacji [33]. Transporter BCRP cechuje się bardzo szeroką specyficznością substratową, z nielicznymi tylko cechami wspólnymi dla jego substratów, takimi jak: obecność w strukturze regionów hydrofobowych i aromatycznych, możliwość przyjmowania konformacji płaskiej oraz obecność grup funkcyjnych zawierających tlen i azot, które mogą stanowić donory lub akceptory wiązań wodorowych [32]. Główna fizjologiczna funkcja BCRP polega na usuwaniu z komórek toksycznych substancji pochodzenia egzo- i endogennego. Z tego względu szczególnie wysoką jego ekspresją cechują się narządy narażone na bezpośrednią styczność z ksenobiotykami lub wymagające szczególnej ochrony, tj. odpowiadające za wchłanianie jelito cienkie, przeprowadzające procesy eliminacji wątroba i nerki oraz w warunkujące dystrybucję komórki śródbłonka, które tworzą barierę krew-mózg i barierę łożyskową [34]. Wysoka ekspresja BCRP jest także charakterystyczna dla komórek macierzystych, zarówno prawidłowych, jak i nowotworowych, stanowiąc w tych ostatnich marker tzw. populacji pobocznej (ang. side population) [35]. Z tego względu macierzyste komórki nowotworów cechują się szczególnie wysoką opornością na terapię z wykorzystaniem leków stanowiących substraty BCRP [14,35].

Udział transportera BCRP w transporcie fotouczulaczy został odkryty przypadkowo w roku 2003, kiedy okazało się, że u myszy z nokautem tego białka pojawiają się zmiany nekrotyczne indukowane światłem. Zmiany te okazały się być wynikiem akumulacji w organizmach zwierząt fotouczulaczy pochodnych chlorofilu pochodzących ze spożywanej przez nie karmy [29]. Późniejsze badania wykazały, że wiele innych fotouczulaczy także stanowi substraty transportera BCRP [14]. Analiza oddziaływań fotouczulaczy z białkiem BCRP stanowi zatem niezbędny element badań przedklinicznych, pozwalający przewidzieć ich farmakokinetykę, która jest niezwykle istotna, zarówno z punktu widzenia wydajności terapii, jak i bezpieczeństwa pacjenta.

II. Cel i zakres rozprawy

Cykl publikacji stanowiących niniejszą rozprawę dotyczy oddziaływania fotouczulaczy pochodnych chlorofilu a, tj. chlorofilidu a oraz cynkowego feoforbidu a z białkiem oporności raka piersi (BCRP, ABCG2) oraz albuminą, a także wpływu tych oddziaływań na efekt fotodynamiczny indukowany z udziałem badanych związków. W temacie pracy transporter BCRP oraz albuminę ujęto pod wspólną nazwą białek transportowych, mając na uwadze, iż mimo że rola tej ostatniej w organizmie wykracza daleko poza procesy transportu, pełni ona jednak niezmiernie istotną funkcję w farmakokinetyce i dystrybucji leków i ksenobiotyków w organizmie [36].

Chlorofilid a oraz cynkowy feoforbid a były już badane w kontekście ich zastosowania w terapii fotodynamicznej, zarówno *in vitro* jak i *in vivo* [23–25]. Badania farmakokinetyki *in vivo* wykazały, że metal centralny determinuje czas retencji fotouczulacza w organizmie [24]. Pochodna cynkowa okazała się pozostawać w tkankach o wiele dłużej niż magnezowa (okresy półtrwania odpowiednio ok. 44 godz. i 13,5 godz.). Przyczyna tego zjawiska nie została dotychczas wyjaśniona, jednak podejrzewano, że może mieć ono związek z aktywnością transportera BCRP, o którym wiadomo, że bierze udział w aktywnym usuwaniu z komórek feoforbidu a [29,37]. Przypuszczano, że pochodna cynkowa może być transportowana przez to białko wolniej niż chlorofilid, a być może nawet zupełnie przez nie nierozpoznawana. Zasadnym zatem było zbadanie oddziaływania podstawionych metalami feoforbidów z białkiem BCRP oraz porównanie tempa ich transportu. Uważa się, że transport substratów o strukturze porfiryn przez białko BCRP sprzężony jest z ich przekazaniem na albuminę (lub inne białko rozpuszczalne) [38]. Ponieważ jednocześnie wiele fotouczulaczy wiąże się do albuminy, białko to wydaje się pełnić w ich farmakokinetyce rolę podwójną tj. poprzez kompleksowanie fotouczulaczy regulować ich akumulację komórkową, ale również odbierać te związki z zewnątrzkomórkowej pętli transportera BCRP, tuż po ich usunięciu z wnętrza komórki (Rys.2). Charakterystyka oddziaływań pochodnych chlorofilu z albuminą była zatem niezbędna do zbadania ich transportu przez BCRP i stanowiła równoległy cel rozprawy.
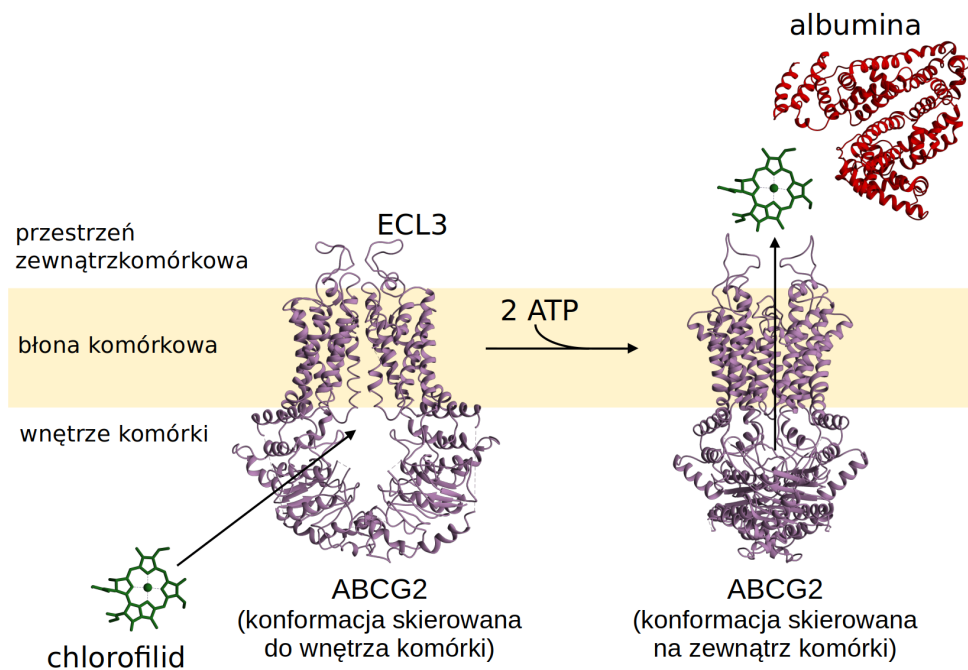
Rys. 2 Schemat transportu pochodnej chlorofilu przez białko ABCG2 z udziałem albuminy

W toku prowadzonych badań pochodna cynkowa, która ze względu na swój wysoki potencjał fotodynamiczny, brak toksyczności ciemnej i stabilność (wyższą niż w przypadku chlorofilidu) stanowi obiecujący do zastosowania w terapii fotouczulacz, okazała się stosunkowo silnie wiązać do albuminy (stała wiązania K_a rzędu 10^6 M^{-1}). Kompleksowanie to jest z jednej strony zjawiskiem korzystnym, ponieważ zapobiega przedwczesnemu wydaleniu fotouczulacza z organizmu, z drugiej jednak znacząco obniża wnikanie fotouczulacza do komórek nowotworowych, co w przypadku terapii guzów litych może wymuszać stosowanie wysokich dawek [39]. Z tego powodu postanowiono zbadać aktywność tej pochodnej wobec komórek śródbłonka naczyń krwionośnych, które z jednej strony cechują się ekspresją receptorów dla albuminy (gp18, gp30, gp60), z drugiej zaś są istotne z punktu widzenia terapii fotodynamicznej, nie tylko guzów nowotworowych ale i szeregu innych schorzeń [5,40–46]. Podejrzewano, że cynkowy feoforbid może indukować śmierć komórek śródbłonka w niskich stężeniach, nawet występując w formie kompleksów z albuminą. Weryfikacja tej hipotezy stanowiła trzeci, obok badania oddziaływań fotouczulaczy z BCRP i albuminą, cel rozprawy.

W ramach rozprawy wykonano następujące zdania badawcze:

1. Przygotowanie fotouczulaczy

2. Hodowla komórek (linie MCF-7 i HUVEC) i transfekcja ludzkim genem *ABCG2* (linia MCF-7)

3. Oznaczanie ekspresji białka BCRP w komórkach (cytometria przepływowa + reakcja PCR w czasie rzeczywistym)

4. Fluorescencyjna analiza akumulacji fotouczulaczy w komórkach

5. Eksperymenty transportowe na płytkach z wykorzystaniem linii MCF-7 o podstawowej i podwyższonej ekspresji transportera BCRP

6. Badanie transportu błonowego w komórkach linii MCF-7 metodą cytometrii przepływowej

7. Zależna od czasu analiza aktywności fotodynamicznej pochodnych chlorofilu (test MTT)

8. Analiza wpływu kompleksowania fotouczulaczy z albuminą na ich wnikanie do komórek nowotworowych (cytometria przepływowa)

9. Izolacja frakcji membranowej z komórek linii MCF-7 i oznaczanie aktywności ATP-azowej

10. Oznaczanie wiązania fotouczulaczy do albuminy ludzkiej (spektroskopia absorpcyjna i emisyjna)

11. Identyfikacja miejsc wiązania fotouczulaczy w strukturze albuminy poprzez analizę ich wypierania przez specyficzne markery

12. Analiza zmian konformacyjnych albuminy pod wpływem wiązania fotouczulaczy (synchroniczny pomiar fluorescencji)

13. Dokowanie molekularne pochodnych feoforbidu a do albuminy ludzkiej (analiza *in silico*)

14. Oznaczanie lokalizacji komórkowej cynkowego feoforbidu a (mikroskopia konfokalna)

15. Oznaczanie rodzaju śmierci komórkowej (mikroskopia, cytometria przepływowa)

16. Badanie transportu cynkowego feoforbidu a przez warstwę komórek śródbłonka naczyń krwionośnych

17. Oznaczanie ekspresji genów zaangażowanych w proces apoptozy w komórkach linii HUVEC (reakcja PCR w czasie rzeczywistym)

18. Statystyczna analiza wyników

Szczegółowa metodologia poszczególnych zadań opisana jest w odpowiednich publikacjach.

III. Wyniki

1. Oddziaływanie fotouczulaczy z transporterem ABCG2 (publikacja 1)

Transport fotouczulaczy (tj. zarówno pochodnych podstawionych metalami, jak i samego feoforbidu a, stanowiącego kontrolny substrat BCRP) badano w linii komórkowej MCF-7 (rak piersi) o podstawowej (podlinia MCF-7/mock) oraz podwyższonej (MCF-7/ABCG2) ekspresji transportera BCRP. Transport w komórkach o podwyższonej ekspresji BCRP badano zarówno przy braku, jak i w obecności specyficznego inhibitora białka BCRP, fumitremorginu C. Pierwszym etapem eksperymentu było wchłanianie fotouczulaczy do komórek w nieobecności surowicy. Następnie roztwory fotouczulaczy usuwano i zastępowano pożywką zawierającą 10% surowicy bydlęcej pozwalając na wypływ fotouczulaczy. Poziom fotouczulaczy oznaczano fluorymetrycznie w kolejnych punktach czasowych (0, 15 min, 30 min, 45 min, 1 godz., 2 godz., 3 godz., 4 godz., 5 godz., 6 godz., 12 godz., 16 godz., 20 godz i 24 godz.). Przy analizie wyników poziom fotouczulaczy w inhibowanych komórkach linii MCF-7/ABCG2 przyjęto za 100%, natomiast ich poziomy w kolejnych punktach czasowych obliczono proporcjonalnie.

Równolegle z eksperymentami transportowymi prowadzono zależne od czasu eksperymenty fotodynamiczne, w ramach których po odpowiednim czasie uwalniania fotouczulacza, komórki poddawano naświetlaniu, a następnie testowi żywotności MTT. Eksperymenty te prowadzone były zarówno w obecności, jak i przy braku surowicy na etapie uwalniania fotouczulacza. Porównanie żywotności komórek pomiędzy dwoma typami eksperymentów fotodynamicznych, jak również zestawienie z odpowiednimi poziomami fotouczulaczy wyznaczonym w opisanym wyżej eksperymencie transportowym, pozwoliło zaobserwować wpływ surowicy na tempo transportu fotouczulaczy.

Zauważono, że transport wszystkich fotouczulaczy (tj. zarówno pochodnych podstawionych metalami, jak i samego feoforbidu a), zachodzi już pod nieobecność surowicy w pożywce. Poziomy wszystkich fotouczulaczy w czasie zero były podobne i wynosiły ok. 85% dla linii MCF-7/mock oraz ok. 75% dla linii MCF-7/ABCG2. Usunięcie

fotouczulaczy i podanie pożywki zawierającej surowicę skutkowało dalszym obniżeniem ich poziomu, które było najszybsze w przypadku feoforbidu (spadek do ok. 40% w obu podliniach), nieco wolniejsze w przypadku pochodnej cynkowej (ok. 60% w MCF-7/mock i 44% w MCF-7/ABCG2), a najwolniejsze w przypadku chlorofilidu (70% w MCF-7/mock i 59 % w MCF-7/ABCG2).

Statystycznie istotną różnicę w poziomie feoforbidu a pomiędzy podliniami komórkowymi różniącymi się poziomem ekspresji BCRP zaobserwowano jedynie dla czasu zero. Dłuższe czasy inkubacji skutkowały zrównaniem poziomu tego fotouczulacza w obu podliniach. W przypadku pochodnych podstawionych metalami natomiast, obserwowane były znaczące różnice pomiędzy podliniami przez cały czas trwania eksperymentu. Wskazuje to, że transport metalopochodnych zachodzi wolniej niż transport feoforbidu a. Wypływ wszystkich fotouczulaczy z komórek był hamowany przez fumitremorgin C, jednakże inhibicja ta w przypadku żadnego z fotouczulaczy nie była kompletna (spadek poniżej 100%). Wyniki eksperymentu transportowego na płytkach zostały potwierdzone oznaczeniami cytometrycznymi przeprowadzonymi w puntach czasowych 0, 15 min, 3 godz. i 24 godz.

Tak jak przypuszczano, żywotność komórek poddanych traktowaniu fotodynamicznemu zwiększała się w miarę wydłużania czasu uwalniania fotouczulaczy. Wzrost żywotności był szybszy dla linii MCF-7/ABCG2 w porównaniu z linią MCF-7/mock, niezależnie od obecności surowicy w pożywce. Różnice w żywotności podlinii o różnej ekspresji BCRP traktowanych feoforbidem były większe w przypadku braku surowicy w pożywce niż w jej obecności. Wskazuje to na przyspieszenie transportu tego fotouczulacza przez surowicę. Fumitremorgin C zwiększał podatność komórek na traktowanie fotodynamiczne przy udziale wszystkich fotouczulaczy, przy czym jego działanie było bardziej efektywne w pożywce pozbawionej surowicy (zerowa żywotność komórek przez cały czas trwania eksperymentu) niż w jej obecności.

Wiązanie fotouczulaczy z albuminą wołową badano spektrofluorymetrycznie poprzez analizę wzmocnienia fluorescencji fotouczulacza przy wzrastającym stężeniu albuminy. Pozorne stałe dysocjacji wyznaczone w tym eksperymencie wnosiły: 26 µM dla feoforbidu, 5,5 µM dla chlorofilidu oraz 3,8 µM dla pochodnej cynkowej. Eksperyment cytometryczny wykazał, że kompleksowanie z albuminą znacząco obniża wchłania fotouczulaczy do komórek MCF-7.

Aktywność ATPazowa frakcji membranowej komórek MCF-7/ABCG2 była hamowana przez wszystkie fotoczulacze przy ich stężeniach równych ok. 100 μM. Najsilniejszą inhibicję wykazywał chlorofilid, nieco słabszą pochodna cynkowa, a najsłabszą feoforbid.

2. Wiązanie fotouczulaczy z albuminą ludzką (publikacja 2)

Oddziaływanie chlorofilidu oraz cynkowego feoforbidu a z albuminą ludzką analizowano metodami spektroskopowymi (absorpcja i fluorescencja w obszarze UV-Vis) oraz za pomocą dokowania molekularnego. Aby zbadać czy fotouczulacze tworzą kompleksy z albuminą, wykonano pomiary ich widm absorpcyjnych w buforze PBS z dodatkiem DMSO w obecności i przy braku albuminy. Zaobserwowane zmiany w widmach dowodzą powstawania kompleksów albumina-fotouczulacz. Widma kompleksów zmierzone przy różnych stężeniach DMSO (1, 5 i 15%) były identyczne, co świadczy o tym, że wiązanie z albuminą powoduje maksymalną dezagregację fotouczulaczy, zatem stałe dysocjacji kompleksów można wyznaczyć stosując 1% stężenie DMSO. Tworzenie kompleksów albumina-fotouczulacz potwierdził również eksperyment polegający na pomiarze wygaszenia fluorescencji białka w obecności fotouczulaczy. Wykazano, że związanie pochodnych chlorofilu prowadzi zarówno do wygaszenia fluorescencji reszt tyrozyny, które są rozproszone w strukturze białka, jak i fluorescencji reszty tryptofanu zlokalizowanej w subdomenie IIA.

Stałe wiązania wyznaczono na podstawie analizy wzmocnienia fluorescencji fotouczulaczy przy wzrastającym stężeniu albuminy. Krzywe wiązania o najlepszym dopasowaniu do wyników pomiarowych uzyskano zakładając obecność w strukturze albuminy dwóch klas miejsc wiążących fotouczulacze. Wartości stałych wiązania przedstawiono w Tabeli 1.

Tabela 1. Stałe wiązania fotouczulaczy do albuminy ludzkiej wyznaczone na podstawie pomiaru wzmocnienia fluorescencji fotouczulaczy.

Fotouczulacz	Stałe wiązania/10^6 [M^{-1}]
chlorofilid a	$K_d^1 = 0{,}40 \pm 0{,}08$
	$K_d^2 = 0{,}02 \pm 0{,}02$
cynkowy feoforbid a	$K_d^1 = 1{,}82 \pm 0{,}39$
	$K_d^2 = 0{,}05 \pm 0{,}02$

Miejsca wiązania fotouczulaczy zidentyfikowano za pomocą eksperymentu wypierania fotouczulaczy przez markery miejsc wiążących: heminę dla miejsca wiążącego hem (subdomena IB), warfarynę dla miejsca Sudlow I (subdomena IIA) oraz ibuprofen dla miejsca Sudlow II (subdomena IIIA). Oba fotouczulacze okazały się być wypierane przez wszystkie trzy markery przy czym wypieranie chlorofilidu było silniejsze niż pochodnej cynkowej, co świadczy o słabszym wiązaniu tego pierwszego.

Synchroniczny pomiar fluorescencji albuminy w obecności fotouczulaczy wykazał jedynie nieznaczne przesunięcie (2 nm) ku krótszym długościom fal widma generowanego przed reszty Tyr w obecności pochodnej cynkowej i brak takiego przesunięcia w obecności chlorofilidu. Wskazuje to, że cynkowy feoforbid, lecz nie chlorofilid a indukuje nieznaczną zmianę konformacyjną cząsteczki białka. Widma synchroniczne reszty Trp nie podlegały przesunięciu, co wskazuje, że konformacja białka w domenie IIA pozostaje niezmieniona w obecności fotouczulaczy.

Dokowanie molekularne potwierdziło, że pochodna cynkowa cechuje się silniejszym niż chlorofilid wiązaniem do albuminy. Wyższe stałe wiązania dla tego pierwszego uzyskano dla wszystkich trzech potencjalnym miejsc wiązania, tj. miejsca wiążącego hem, oraz miejsc Sudlow I i II. Ponadto w przypadku pochodnej cynkowej zidentyfikowano więcej niż w przypadku magnezowej reszt aminokwasowych wykazujących bezpośrednie wiązanie z fotouczulaczem. Zidentyfikowane oddziaływania miały głównie charakter hydrofobowy, w mniejszej liczbie występowały wiązania wodorowe. Nie zidentyfikowano natomiast wiązania reszt aminokwasowych w pozycji aksjalnej, jakie występuje pomiędzy cząsteczkami chlorofili i białek anten fotosyntetycznych, a także pomiędzy hemem i apoproteinami hemoglobiny i mioglobiny.

3. Aktywność fotodynamiczna cynkowego feoforbidu a wobec komórek śródbłonka naczyń krwionośnych (publikacja 3)

Komórki linii HUVEC, stanowiące model śródbłonka naczyń krwionośnych, zostały porównane z linią nowotworową MCF-7 pod względem akumulacji cynkowego feoforbidu a oraz wywoływanego przezeń efektu fotodynamicznego w obecności i przy braku albuminy ludzkiej. Akumulacja fotouczulacza przy braku albuminy w pożywce była w obu liniach podobna, a fotouczulacz w stężeniu 1 µM przy dawce światła 2J/cm^2

powodował śmierć blisko 100% komórek. W obecności wysycającego stężenia albuminy (250 µM) natomiast, akumulacja fotouczulacza w linii HUVEC była 2-krotnie wyższa niż w linii MCF-7, przeżywalność komórek natomiast wynosiła odpowiednio 100% w linii MCF-7 i ok. 20% w linii HUVEC.

Linia HUVEC (niezależnie od obecności albuminy) okazała się cechować wyższą podatnością na traktowanie fotodynamiczne z udziałem cynkowego feoforbidu a w porównaniu z linią MCF-7 (wartość współczynnika IC50 wynosiła ok. 20 nM dla linii HUVEC i ponad 500 nM dla linii MCF-7).

Ekspresja genu *ABCG2* oznaczona metodą real-time PCR okazała się ok. dwukrotnie niższa w linii HUVEC niż w linii MCF-7, co częściowo tłumaczy wyższą podatność tej pierwszej na traktowanie fotodynamiczne z udziałem cynkowego feoforbidu a.

Oznaczenie akumulacji cynkowego feoforbidu a równolegle z wywoływanym przezeń efektem fotodynamicznym przy różnych stężeniach albuminy pozwoliło stwierdzić, że kompleks albumina-fotouczulacz wnika do komórek śródbłonka i wykazuje działanie fotodynamiczne silniejsze niż wolny fotouczulacz. Analiza metodą mikroskopii konfokalnej wykazała z kolei, że kompleksowanie z albuminą zwiększa lizosomalną akumulację fotouczulacza.

Eksperyment z wykorzystaniem komórek linii HUVEC hodowanych na wkładach membranowych pozwolił stwierdzić, że fotouczulacz występuje w komórkach głównie w formie wolnej (nieskompleksowanej z albuminą), a jego wydajne usuwanie wymaga obecności surowicy/albuminy w przestrzeni zewnątrzkomórkowej.

Analiza śmierci komórkowej metodami mikroskopii konfokalnej oraz cytometrii przepływowej wykazała, że w obecności niskiego stężenia (100 nM) feoforbidu a, a także stężenia wyższego (1 µM) lecz w formie skompleksowanej z albuminą, komórki linii HUVEC podlegają głównie apoptozie. Z kolei 1 µM stężenie fotouczulacza w formie wolnej indukuje śmierć komórek głównie na drodze nekrozy.

IV. Dyskusja

Niniejsza praca poświęcona była badaniu oddziaływań regulujących farmakokinetykę fotouczulaczy pochodnych chlorofilu tj. ich transportu przez białko błonowe BCRP oraz wiązaniu z albuminą, a także wpływu tych oddziaływań na efektywność fotodynamiczną fotouczulaczy.

Analiza transportu i zależnej od czasu efektywności fotodynamicznej fotouczulaczy wykazała, że, podobnie jak sam feoforbid a, jego pochodne podstawione metalami, stanowią substraty transportera błonowego ABCG2, a tempo ich transportu zależne jest od stężenia albuminy w przestrzeni zewnątrzkomórkowej. Przyspieszenie transportu pochodnych chlorofilu przez albuminę może być interpretowane jako efekt ich wiązania z tym białkiem, które przeciwdziała ich zwrotnemu wchłanianiu, a tym samym przyczynia się do obniżenia ich poziomu w komórce. Znaczny jednak wzrost tempa transportu słabo wiążącego się z albuminą feoforbidu a w obecności tego białka, każe przypuszczać, że ograniczenie zwrotnego wchłaniania nie jest jedynym mechanizmem decydującym o przyspieszeniu transportu fotouczulaczy przez albuminę. Prawdopodobnie albumina bierze również bezpośredni udział w transporcie poprzez odbiór substratów BCRP z jego zewnątrzkomórkowej domeny ECL3, co postulowane jest także dla innych substratów tego białka o podobnej strukturze [38]. Albumina reguluje zatem biodostępność pochodnych chlorofilu w dwojaki sposób: poprzez ich kompleksowanie, które ogranicza wchłanianie fotouczulaczy do komórek, a także poprzez ich odbiór z zewnątrzkomórkowej domeny białka BCRP tuż po wytransportowaniu z komórki, choć mechanizm tego ostatniego zjawiska nie jest jeszcze dobrze poznany.

Ponieważ pochodna cynkowa wiąże się do albuminy silniej niż chlorofilid, a wiązanie to znacząco osłabia jej wnikanie do komórek, obserwowany we wcześniejszych badaniach *in vivo* efekt dłuższej retencji tej pierwszej w tkankach wynika najprawdopodobniej nie z jej szybszego transportu przez BCRP, ale z zalegania w płynie śródmiąższowym (interstitium) w formie kompleksu z albuminą. Przypuszczalnie zaleganie to może być dłuższe w obrębie guzów nowotworowych niż w zdrowych tkankach, ze względu na ich niedojrzałą, słabo zorganizowaną i nieszczelną sieć naczyń krwionośnych (efekt EPR) [47–49].

Wydajny transport fotouczulaczy zachodzi już przy bardzo niskich stężeniach albuminy, dlatego występująca przy różnych schorzeniach hipoalbuminemia prawdopodobnie nie będzie wpływać na tempo ich transportu. Prawdopodobnie jednak będzie miała ona wpływ na ogólnoustrojowy poziom fotouczulaczy, ponieważ związek wolny podlegać będzie szybszemu wydalaniu niż skompleksowany.

Ponadto farmakokinetyka podstawionych metalami feoforbidów będzie uzależniona od obecności innych ligandów albuminy. Hem, o silnym powinowactwie do albuminy

($K_a \sim 10^8$ M^{-1}) będzie wypierał związane z albuminą fotouczulacze z najsilniej wiążącego je miejsca zlokalizowanego w subdomenie IB [50]. Zjawisko to może mieć znaczenie u pacjentów z silną hemolizą, u których zdolność wiążąca głównego białka kompleksującego hem, jakim jest hemopeksyna, może być niewystarczająca, przez co znaczna jego frakcja będzie wiązać się z albuminą. Wypierania fotouczulaczy z miejsc wiążących albuminy nie będą jednak wywoływać naturalnie dostające się do organizmu pochodne chlorofilu (feofityna, feoforbid), których powinowactwo do albuminy jest niskie [51]. Stężenie wolnych form fotouczulaczy w surowicy będzie natomiast wzrastać u pacjentów przyjmujących leki silnie wiążące się z albuminą, np. ibuprofen. Silniejsze powinowactwo do albuminy cynkowego feoforbidu w porównaniu z chlorofilidem wskazuje, że różnice w farmakokinetyce obserwowane u zwierząt, najprawdopodobniej wystąpią również u ludzi.

Silne wiązanie z albuminą nie eliminuje możliwości zastosowania klinicznego cynkowej pochodnej feoforbidu a. Przeciwnie, może być ono postrzegane jako zaleta tego fotouczulacza, gdyż przeciwdziała jego przedwczesnemu wydaleniu z organizmu, zapewniając jego optymalny czas retencji w tkankach. Jednocześnie efektywność terapii wykorzystującej ten fotouczulacz może być zadowalająca dzięki wysokiej podatności komórek śródbłonka naczyń krwionośnych na traktowanie fotodynamiczne z jego udziałem.

Cynkowy feoforbid a potencjalnie może znaleźć zastosowanie w terapii fotodynamicznej skierowanej przeciwko naczyniom krwionośnym (ang. Vascular-Targeted Photodynamic therapy, VTP), zarówno w leczeniu guzów litych, jak i szeregu schorzeń naczyniowych. Jego kompleksowanie z albuminą jest silniejsze od stosowanego w praktyce klinicznej fotouczulacza o podobnej budowie, pochodnej palladowego bakteriofeoforbidu (nazwa handlowa TOOKAD®Soluble) [52]. Daje mu to pewną przewagę nad tym ostatnim, gdyż wydłuża czas retencji w organizmie umożliwiając, po pierwsze przezskórny monitoring jego koncentracji w organizmie, po drugie przeprowadzenie wielu naświetlań po jednej tylko aplikacji. Dodatkowo aktywność fotodynamiczna feoforbidu cynkowego wobec komórek śródbłonka jest wyższa niż bakteriofeoforbidu palladowego (wartość współczynnika IC50 równa odpowiednio 20 nM przy dawce światła 2 J/cm^2 dla pierwszego oraz 1 µM przy 12 J/cm^2 dla drugiego) [52]. Jednocześnie, feoforbid cynkowy, syntetyzowany z chlorofilu a, czyli związku taniego i dostępnego w praktycznie nieograniczonych ilościach, a ponadto niewymagający skomplikowanych modyfikacji chemicznych jest fotouczulaczem mniej kosztownym niż TOOKAD®Soluble [53].

V. Wnioski

1. Pochodne feoforbidu a podstawione w centrum pierścienia makrocyklicznego jonami magnezu i cynku są substratami transportera błonowego ABCG2. Obie pochodne transportowane są wolniej niż sam feoforbid, a ponadto pochodna magnezowa (chlorofilid) nieco wolniej niż cynkowa.

2. Wydajny transport pochodnych chlorofilu wymaga obecności w środowisku zewnątrzkomórkowym albuminy (lub innego białka rozpuszczalnego).

3. Przyspieszenie transportu pochodnych chlorofilu w obecności albuminy/surowicy obniża wydajność inhibicji z udziałem fumitremorginu C.

4. Różnice w farmakokinetyce fotouczulaczy obserwowane we wcześniejszych badaniach *in vivo* wynikają najprawdopodobniej nie z różnic w ich oddziaływaniu z BCRP, ale z albuminą.

5. Feoforbid a i jego pochodne w wysokich stężeniach (> 50 µM) hamują aktywność ATPazową transportera ABCG2.

6. Chlorofilid a oraz cynkowy feoforbid a wiążą się z albuminą ludzką ze stałymi wiązania odpowiednio rzędu 10^5 i 10^6 M^{-1}.

7. Główne miejsce wiązania podstawionych metalami feoforbidów w strukturze albuminy znajduje się prawdopodobnie w subdomenie IB (miejsce wiążące hem). Ponadto słabsze wiązanie występuje w subdomenach IIA I IIIA (miejsca wiążące Sudlow I Sudlow II).

8. Wiązanie feoforbidów do albuminy wynika głównie z oddziaływań hydrofobowych oraz tworzenia wiązań wodorowych przez podstawniki boczne ligandów.

9. Związanie pochodnej cynkowej, ale nie magnezowej, indukuje niewielką zmianę konformacyjną cząsteczki albuminy.

10. Komórki śródbłonka naczyń krwionośnych (HUVEC) są bardziej podatne na efekt fotodynamiczny z udziałem cynkowego feoforbidu a od komórek nowotworowych (MCF-7).

11. Kompleks cynkowego feoforbidu a z albuminą wnika do komórek śródbłonka i lokalizuje się w lizosomach, gdzie komponent białkowy najprawdopodobniej ulega degradacji, natomiast uwolniony fotouczulacz zachowuje swoją aktywność.

12. Lokalizacja lizosomalna sprzyja nasileniu efektu fotodynamicznego przy udziale cynkowego feoforbidu a w linii komórkowej HUVEC.

13. Efektywne usuwanie cynkowego feoforbidu a z komórek HUVEC jest zależne od obecności albuminy w przestrzeni zewnątrzkomórkowej.

14. Cynkowy feoforbid a w niskich stężeniach (~nM) i przy niskiej dawce światła (2 J/cm^2) indukuje śmierć komórek linii HUVEC na drodze apoptozy, stężenie 1 µM fotouczulacza przy tej samej dawce światła zabija te komórki na drodze nekrozy.

15. Wiązanie cynkowego feoforbidu a z albuminą, poprzez regulację jego poziomu komórkowego, ma wpływ na rodzaj śmierci komórkowej indukowanej traktowaniem fotodynamicznym z udziałem tego fotouczulacza.

VI. Literatura

[1]   P. Agostinis, K. Berg, K.A. Cengel, T.H. Foster, A.W. Girotti, S.O. Gollnick, S.M. Hahn, M.R. Hamblin, A. Juzeniene, D. Kessel, M. Korbelik, J. Moan, P. Mroz, D. Nowis, J. Piette, B.C. Wilson, J. Golab, Photodynamic therapy of cancer: an update, CA Cancer J. Clin. 61 (2011) 250–281. https://doi.org/10.3322/caac.20114.

[2]   Á. Juarranz, P. Jaén, F. Sanz-Rodríguez, J. Cuevas, S. González, Photodynamic therapy of cancer. Basic principles and applications, Clin. Transl. Oncol. 10 (2008) 148–154. https://doi.org/10.1007/s12094-008-0172-2.

[3]   X. Wen, Y. Li, M.R. Hamblin, Photodynamic therapy in dermatology beyond non-melanoma cancer: an update, Photodiagnosis Photodyn Ther. 19 (2017) 140–152. https://doi.org/doi:10.1016/j.pdpdt.2017.06.010.

[4]   Y. Liu, R. Qin, S.A.J. Zaat, E. Breukink, M. Heger, Antibacterial photodynamic therapy: overview of a promising approach to fight antibiotic-resistant bacterial infections, J. Clin. Transl. Res. 1 (2015) 140–167. https://doi.org/10.18053/jctres.201503.002.

[5]   K.H. Yuan, Q. Li, W.L. Yu, Z. Huang, Photodynamic therapy in treatment of port wine stain birthmarks-Recent progress, Photodiagnosis Photodyn. Ther. 6 (2009) 189–194. https://doi.org/10.1016/j.pdpdt.2009.08.001.

[6]   P. Calzavara-Pinton, M.T. Rossi, R. Sala, M. Venturini, Photodynamic antifungal chemotherapy, Photochem. Photobiol. 88 (2012) 512–522. https://doi.org/10.1111/j.1751-1097.2012.01107.x.

[7]   Y.N. Konan, R. Gurny, E. Allémann, State of the art in the delivery of photosensitizers for photodynamic therapy, J. Photochem. Photobiol. B Biol. 66 (2002) 89–106. https://doi.org/10.1016/S1011-1344(01)00267-6.

[8]   K. Plaetzer, M. Berneburg, T. Kiesslich, T. Maisch, New applications of photodynamic therapy in biomedicine and biotechnology, Biomed Res. Int. 2013 (2013) 1–3. https://doi.org/10.1155/2013/161362.

[9]   A.P. Castano, T.N. Demidova, M.R. Hamblin, Mechanisms in photodynamic therapy: Part one - Photosensitizers, photochemistry and cellular localization, Photodiagnosis Photodyn. Ther. 1 (2004) 279–293. https://doi.org/10.1016/S1572-1000(05)00007-4.

[10]   B. Joanna, A. Fabisiewicz, J. Siedlecki, Terapia fotodynamiczna – znaczenie w onkologii, (2015) 236–247.

[11]   S.A. McFarland, A. Mandel, R. Dumoulin-White, G. Gasser, Metal-based photosensitizers for photodynamic therapy: the future of multimodal oncology?, Curr. Opin. Chem. Biol. 56 (2020) 23–27. https://doi.org/10.1016/j.cbpa.2019.10.004.

[12]   L. Benov, Photodynamic therapy: Current status and future directions, Med. Princ. Pract. 24 (2015) 14–28. https://doi.org/10.1159/000362416.

[13]   I.S. Mfouo-Tynga, L.D. Dias, N.M. Inada, C. Kurachi, Features of third generation photosensitizers used in anticancer photodynamic therapy: Review, Photodiagnosis Photodyn. Ther. 34 (2021) 102091. https://doi.org/10.1016/j.pdpdt.2020.102091.

[14]   M.R. Hamblin, Drug efflux pumps in photodynamic therapy, Elsevier Inc., 2020. https://doi.org/10.1016/b978-0-12-816434-1.00008-5.

[15]   J. Zhang, C. Jiang, J.P. Figueiró Longo, R.B. Azevedo, H. Zhang, L.A. Muehlmann, An updated overview on the development of new photosensitizers for anticancer photodynamic therapy, Acta Pharm. Sin. B. 8 (2018) 137–146. https://doi.org/10.1016/j.apsb.2017.09.003.

[16]   R. Baskaran, J. Lee, S.G. Yang, Clinical development of photodynamic agents and therapeutic applications, Biomater. Res. 22 (2018) 1–8. https://doi.org/10.1186/s40824-018-0140-z.

[17]   A.S. Brandis, Y. Salomon, A. Scherz, Chlorophyll Sensitizers in Photodynamic Therapy, in: B. Grimm, R.J. Porra, W. Rüdiger, H. Scheer (Eds.), Chlorophylls Bacteriochlorophylls Biochem. Biophys. Funct. Appl., Springer Netherlands, Dordrecht, 2006: pp. 461–483. https://doi.org/10.1007/1-4020-4516-6_32.

[18]   A.R. Azzouzi, E. Barret, C.M. Moore, A. Villers, C. Allen, A. Scherz, G. Muir, M. De Wildt, N.J. Barber, S. Lebdai, M. Emberton, TOOKAD® Soluble vascular-targeted photodynamic (VTP) therapy: Determination of optimal treatment conditions and assessment of effects in patients with localised prostate cancer, BJU Int. 112 (2013) 766–774. https://doi.org/10.1111/bju.12265.

[19]   S.S. Dhillon, T.L. Demmy, S. Yendamuri, G. Loewen, C. Nwogu, M. Cooper, B.W. Henderson, A phase I study of light dose for photodynamic therapy using 2-[1-Hexyloxyethyl]-2 devinyl pyropheophorbide-a for the treatment of non-small cell carcinoma in situ or non-small cell microinvasive bronchogenic carcinoma: A dose ranging study, J. Thorac. Oncol. 11 (2016) 234–241. https://doi.org/10.1016/j.jtho.2015.10.020.

[20]   N. Rigual, G. Shafirstein, M.T. Cooper, H. Baumann, D.A. Bellnier, U. Sunar, E.C. Tracy, D.J. Rohrbach, G. Wilding, W. Tan, M. Sullivan, M. Merzianu, B.W. Henderson, Photodynamic therapy with 3-(10-hexyloxyethyl) pyropheophorbide a for cancer of the oral cavity, Clin. Cancer Res. 19 (2013) 6605–6613. https://doi.org/10.1158/1078-0432.CCR-13-1735.

[21]   H.R. Nava, S.S. Allamaneni, T.J. Dougherty, M.T. Cooper, W. Tan, G. Wilding, B.W. Henderson, Photodynamic therapy (PDT) using HPPH for the treatment of precancerous lesions associated with barrett's esophagus, Lasers Surg. Med. 43 (2011) 705–712. https://doi.org/10.1002/lsm.21112.

[22]   S. Avigdor, S. Yoram, F. Leszek, Chlorophyll and bacteriochlorophyll derivatives, their preparation and pharmaceutical compositions comprising them, 1993. http://europepmc.org/patents/PAT/EP0584552.

[23]   M. Jakubowska, M. Szczygieł, D. Michalczyk-Wetula, A. Susz, G. Stochel, M. Elas, L. Fiedor, K. Urbanska, Zinc-pheophorbide a-Highly efficient low-cost photosensitizer against human adenocarcinoma in cellular and animal models, Photodiagnosis Photodyn. Ther. 10 (2013) 266–277. https://doi.org/http://dx.doi.org/10.1016/j.pdpdt.2012.12.004.

[24]   M. Szczygieł, K. Urbańska, P. Jurecka, I. Stawoska, G. Stochel, L. Fiedor, Central metal determines pharmacokinetics of chlorophyll-derived xenobiotics, J. Med. Chem. 51 (2008) 4412–4418. https://doi.org/10.1021/jm7016368.

[25]   M. Szczygieł, B. Boroń, D. Szczygieł, M. Szafraniec, A. Susz, Z. Matuszak, K. Urbańska, L. Fiedor, Real-time Non-invasive Transdermal Monitoring of Photosensitizer Level in vivo for Pharmacokinetic Studies and Optimization of Photodynamic Therapy Protocol, J. Anal. Bioanal. Tech. 5 (2014). https://doi.org/10.4172/2155-9872.1000227.

[26] A.P. Gerola, T.M. Tsubone, A. Santana, H.P.M. De Oliveira, N. Hioka, W. Caetano, Properties of chlorophyll and derivatives in homogeneous and microheterogeneous systems, J. Phys. Chem. B. 115 (2011) 7364–7373. https://doi.org/dx.doi.org/10.1021/jp201278b.

[27] Z. Ni, Z. Bikadi, D.L. Shuster, C. Zhao, M.F. Rosenberg, Q. Mao, Identification of proline residues in or near the transmembrane helices of the human breast cancer resistance protein (BCRP/ABCG2) that are important for transport activity and substrate specificity, Biochemistry. 50 (2011) 8057–8066. https://doi.org/10.1021/bi200573t.

[28] T. Ozben, Mechanisms and strategies to overcome multiple drug resistance in cancer, FEBS Lett. 580 (2006) 2903–2909. https://doi.org/10.1016/j.febslet.2006.02.020.

[29] J.W. Jonker, M. Buitelaar, E. Wagenaar, M.A. Van der Valk, G.L. Scheffer, R.J. Scheper, T. Plösch, F. Kuipers, R.P.J. Oude Elferink, H. Rosing, J.H. Beijnen, A.H. Schinkel, The breast cancer resistance protein protects against a major chlorophyll-derived dietary phototoxin and protoporphyria, Proc. Natl. Acad. Sci. U. S. A. 99 (2002) 15649–15654. https://doi.org/https://doi.org/10.1073/pnas.202607599.

[30] P. Krishnamurthy, D.D. Ross, T. Nakanishi, K. Bailey-Dell, S. Zhou, K.E. Mercer, B. Sarkadi, B.P. Sorrentino, J.D. Schuetz, The stem cell marker Bcrp/ABCG2 enhances hypoxic cell survival through interactions with heme, J. Biol. Chem. 279 (2004) 24218–24225. https://doi.org/10.1074/jbc.M313599200.

[31] J.W. Jonker, S. Musters, M.L.H. Vlaming, T. Plösch, K.E.R. Gooijert, M.J. Hillebrand, H. Rosing, J.H. Beijnen, H.J. Verkade, A.H. Schinkel, Breast cancer resistance protein (Bcrp1/Abcg2) is expressed in the harderian gland and mediates transport of conjugated protoporphyrin IX, Am. J. Physiol. - Cell Physiol. 292 (2007) 2204–2212. https://doi.org/10.1152/ajpcell.00359.2006.

[32] M.J. Szafraniec, M. Szczygieł, K. Urbanska, L. Fiedor, Determinants of the activity and substrate recognition of breast cancer resistance protein (ABCG2), Drug Metab. Rev. 46 (2014) 459–474. https://doi.org/10.3109/03602532.2014.942037.

[33] C. Özvegy, T. Litman, G. Szakács, Z. Nagy, S. Bates, A. Váradi, B. Sarkadi, Functional characterization of the human multidrug transporter, ABCG2, expressed in insect cells, Biochem. Biophys. Res. Commun. 285 (2001) 111–117. https://doi.org/10.1006/bbrc.2001.5130.

[34] E.M. Leslie, R.G. Deeley, S.P.C. Cole, Multidrug resistance proteins: Role of P-glycoprotein, MRP1, MRP2, and BCRP (ABCG2) in tissue defense, Toxicol. Appl. Pharmacol. 204 (2005) 216–237. https://doi.org/10.1016/j.taap.2004.10.012.

[35] X. wei Ding, J. hua Wu, C. ping Jiang, ABCG2: A potential marker of stem cells and novel target in stem cell and cancer therapy, Life Sci. 86 (2010) 631–637. https://doi.org/10.1016/j.lfs.2010.02.012.

[36] R. Raoufinia, A. Mota, N. Keyhanvar, F. Safari, S. Shamekhi, J. Abdolalizadeh, Overview of albumin and its purification methods, Adv. Pharm. Bull. 6 (2016) 495–507. https://doi.org/10.15171/apb.2016.063.

[37] R.W. Robey, K. Steadman, O. Polgar, K. Morisaki, M. Blayney, P. Mistry, S.E. Bates, Pheophorbide a Is a Specific Probe for ABCG2 Function and Inhibition, Cancer Res. 64 (2004) 1242–1246. https://doi.org/10.1158/0008-5472.CAN-03-3298.

[38] E. Desuzinges-Mandon, O. Arnaud, L. Martinez, F. Huché, A. Di Pietro, P. Falson, A. Di Pietro, P. Falson, ABCG2 transports and transfers heme to albumin through its large extracellular loop, J. Biol. Chem. 285 (2010) 33123–33133. https://doi.org/10.1074/jbc.M110.139170.

[39] M.J. Szafraniec, L. Fiedor, One ring is not enough to rule them all. Albumin-dependent ABCG2-mediated transport of chlorophyll-derived photosensitizers., Eur. J. Pharm. Sci. 167 (2021) 106001. https://doi.org/10.1016/j.ejps.2021.106001.

[40] J.E. Schnitzer, gp60 is an albumin-binding glycoprotein expressed by continuous endothelium involved in albumin transcytosis, Am. J. Physiol. 262 (1992) H246-54. https://doi.org/10.1152/ajpheart.1992.262.1.H246.

[41] C. Tiruppathi, W. Song, M. Bergenfeldt, P. Sass, A.B. Malik, Gp60 activation mediates albumin transcytosis in endothelial cells by tyrosine kinase-dependent pathway, J. Biol. Chem. 272 (1997) 25968–25975. https://doi.org/10.1074/jbc.272.41.25968.

[42] J.E. Schnitzer, P. Oh, Albondin-mediated capillary permeability to albumin. Differential role of receptors in endothelial transcytosis and endocytosis of native and modified albumins, J. Biol. Chem. 269 (1994) 6072–6082.

[43] W. Jerjes, T. Upile, Z. Hamdoon, C.A. Mosse, S. Akram, S. Morley, C. Hopper, Interstitial PDT for vascular anomalies, Lasers Surg. Med. 43 (2011) 357–365. https://doi.org/10.1002/lsm.21058.

[44] V. Mashayekhi, C. Op't Hoog, S. Oliveira, Vascular targeted photodynamic therapy : A review of the efforts towards molecular targeting of tumor vasculature, J. Porphyrins Phtalocyanines. 23 (2019) 1229–1240. https://doi.org/doi:10.1142/s1088424619300180.

[45] L. Nogueira, A.T. Tracey, R. Alvim, P. Reisz, A. Scherz, J.A. Coleman, K. Kim, Developments in Vascular-Targeted Photodynamic Therapy for Urologic Malignancies, Molecules. 25 (2020) 1–12. https://doi.org/10.3390/molecules25225417.

[46] A.R. Azzouzi, S. Lebdai, F. Benzaghou, C. Stief, Vascular-targeted photodynamic therapy with TOOKAD® Soluble in localized prostate cancer: standardization of the procedure, World J. Urol. 33 (2015) 937–944. https://doi.org/10.1007/s00345-015-1535-2.

[47] P. Carmeliet, R.K. Jain, Angiogenesis in cancer and other diseases, Nature. 407 (2000) 249–257. https://www.nature.com/articles/35025220.

[48] A.M. Merlot, D.S. Kalinowski, D.R. Richardson, Unraveling the mysteries of serum albumin-more than just a serum protein, Front. Physiol. 5 (2014) 1–7. https://doi.org/10.3389/fphys.2014.00299.

[49] M. Welter, H. Rieger, Interstitial Fluid Flow and Drug Delivery in Vascularized Tumors: A Computational Model, PLoS One. 8 (2013) 1–23. https://doi.org/10.1371/ journal.pone.0070395.

[50] J.K.A. Kamal, D. V Behere, Binding of heme to human serum albumin: Steady-state fluorescence, circular dichroism and optical difference spectroscopic studies, Indian J. Biochem. Biophys. 42 (2005) 7–12.

[51] O.A. Chaves, A.P. de O. Amorim, L.H.E. Castro, C.M.R. Sant'Anna, M.C.C. De Oliveira, D. Cesarin-Sobrinho, J.C. Netto-Ferreira, A.B.B. Ferreira, Fluorescence and Docking Studies of the Interaction between Human Serum Albumin and Pheophytin, Molecules. 20 (2015) 19526–19539. https://doi.org/10.3390/molecules201019526.

[52] O. Mazor, A. Brandis, V. Plaks, E. Neumark, V. Rosenbach-Belkin, Y. Salomon, A. Scherz, WST11, A Novel Water-soluble Bacteriochlorophyll Derivative; Cellular Uptake, Pharmacokinetics, Biodistribution and Vascular-targeted Photodynamic Activity Using Melanoma Tumors as a Model, Photochem. Photobiol 81 (2005) 342. https://doi.org/10.1562/2004-06-14-ra-199.1.

[53] C.H. Yang, K.S. Huang, Y.T. Wang, J.F. Shaw, A review of bacteriochlorophyllides: Chemical structures and applications, Molecules. 26 (2021) 1–14. https://doi.org/10.3390/molecules26051293.

Streszczenie

Farmakokinetyka związków stosowanych jako fotouczulacze w terapii fotodynamicznej jest niezwykle istotna zarówno z punktu widzenia efektywności terapii, jak i bezpieczeństwa pacjenta. W niniejszej pracy poddano analizie dwa istotne dla dystrybucji w organizmie oddziaływania, tj. transport przez białko błonowe BCRP (ABCG2) oraz wiązanie z albuminą fotouczulaczy będących pochodnymi feoforbidu a, produktu degradacji chlorofilu a występującego w przyrodzie. Badane były dwie pochodne feoforbidu a podstawione w centrum pierścienia magnezem (chlorofilid a) oraz cynkiem (cynkowy feoforbid a). Oddziaływania pochodnych chlorofilu a z BCRP i albuminą badane były równolegle z analizą ich wpływu na efektywność fotodynamiczną fotouczulaczy.

Transport fotouczulaczy badano w linii komórkowej MCF-7 (rak piersi) o podstawowej oraz podwyższonej na drodze transfekcji ekspresji transportera BCRP. Równolegle z analizą transportu określano efekt fotodynamiczny wywoływany przez fotouczulacz pozostający w komórkach po określonym czasie transportu. Wykazano, że zarówno pochodna magnezowa, jak i cynkowa feoforbidu a są substratami transportera, jednak tempo ich transportu jest nieco niższe niż w przypadku feoforbidu a, będącego potwierdzonym wcześniej substratem białka BCRP. Dodatkowo, niższe tempo transportu zaobserwowano dla chlorofilidu niż dla pochodnej cynkowej. Wynika to najprawdopodobniej z różnic w sile ich wiązania z zewnątrzkomórkową pętlą ECL3 transportera. Jednocześnie zaobserwowano, że tempo transportu obu pochodnych, podobnie jak feoforbidu a, jest znacznie obniżone przy braku w środowisku zewnątrzkomórkowym surowicy/albuminy, podobnie jak obserwowano to w przypadku innych związków o podobnej budowie. Tempo transportu wzrasta ze wzrostem stężenia albuminy, osiągając poziom plateau przy stężeniu ok. 250 µM. Przyspieszenie transportu może wynikać ze związania fotouczulacza z albuminą, które powoduje, ze utworzony kompleks nie wnika zwrotnie do komórki. Możliwe jednak, że nie jest to jedyny mechanizm tego zjawiska, ponieważ nie zaobserwowano zależności pomiędzy tempem transportu fotouczulaczy a ich powinowactwem do albuminy. Zaobserwowano, że pochodne podstawione metalami wiążą się z albuminą znacznie silnej niż feoforbid a. Wiązanie to jest silniejsze dla pochodnej cynkowej niż dla magnezowej.

Najprawdopodobniej różnica ta, a nie jak wcześniej przypuszczano, różnica w tempie transportu przez BCRP, odpowiada za obserwowany we wcześniejszych badaniach wydłużony czas retencji w organizmie pochodnej cynkowej w porównaniu z chlorofilidem.

Aby szczegółowo scharakteryzować wiązanie fotouczulaczy z albuminą ludzką, przeprowadzono badania spektroskopowe oraz dokowanie molekularne. Stałe wiązania wyznaczono poprzez pomiar wzmocnienia fluorescencji fotouczulacza przy wzrastającym stężeniu albuminy. Prawdopodobne miejsca wiązania wskazano natomiast na drodze pomiaru wygaszenia fluorescencji albuminy przy wzrastających stężeniach fotouczulaczy oraz dokowania molekularnego. Badania te wykazały, że pochodne chlorofilu wiążą się najsilniej w miejscu wiążącym hem zlokalizowanym w subdomenie IB, słabiej natomiast w głównych miejscach wiązania albuminy tj. Sudlow1 i Sudlow2, zlokalizowanych odpowiednio w subdomenach IIA i IIIA. Wiązanie to jest oparte głównie o oddziaływania hydrofobowe, a w mniejszym stopniu wiązania wodorowe. Wyznaczone stałe wiązania są nieco niższe dla chlorofilidu niż dla cynkowego feoforbidu. Ponadto, liczba zidentyfikowanych reszt aminokwasowych zaangażowanych w wiązanie z albuminą jest dla tego pierwszego niższa niż dla drugiego. To pozwala przypuszczać, że różnice w ich farmakokinetyce zaobserwowane u zwierząt, będą występować również u ludzi.

Ze względu na stosunkowo silne wiązanie cynkowego feoforbidu z albuminą, które hamuje jego wnikanie do komórek nowotworowych, a z drugiej strony wysoką wydajność fotodynamiczną tej pochodnej, postanowiono zbadać, czy kompleks albumina-cynkowy feoforbid wnika do komórek śródbłonka naczyń krwionośnych. Komórki śródbłonka naczyń posiadają zdolność pobierania albuminy na drodze endocytozy, a jednocześnie stanowią istotny cel terapii fotodynamicznej skierowanej przeciwko różnym jednostkom chorobowym. Eksperymenty z udziałem modelowej linii HUVEC (komórki endotelium pozyskane z żyły pępowinowej) potwierdziły, że kompleks jest transportowany do komórek. Ponadto kompleksowanie fotouczulacza z albuminą podwyższa jego akumulację lizosomalną, wzmacniając tym samym indukowany efekt fotodynamiczny. Wykazano także, że linia HUVEC jest bardziej podatna na traktowanie fotodynamiczne z udziałem cynkowego feoforbidu niż nowotworowa linia MCF-7. Wartość współczynnika IC50 dla linii HUVEC przy dawce światła równej 2 J/cm^2 i 3-godzinnym czasie akumulacji wynosi ok. 20 nM, podczas gdy dla linii MCF-7 wartość ta jest ok. 25-krotnie wyższa. Wykazano

także, że rodzaj śmierci komórkowej indukowanej traktowaniem fotodynamicznym zależny jest od poziomu cynkowego feoforbidu a zakumulowanego w komórkach. Przy niskim poziomie fotouczulacza komórki podlegają apoptozie, a przy wysokim nekrozie. Ponieważ wysokie stężenia albuminy znacząco obniżają akumulację komórkową fotouczulacza, będą one także kierować komórki na szlak apoptozy, co może być efektem korzystnym, ze względu na ograniczenie stanu zapalnego.

Abstract

Pharmacokinetics of drugs used in photodynamic therapy is of crucial importance for both the efficacy of therapy and patient safety. In the present study, two factors critical for the distribution of chlorophyll-derived photosensitizers (PSs) in the body, i.e. their transport *via* the breast cancer resistance protein (BCRP, ABCG2) and binding to serum albumin, were analyzed. The investigated compounds were chlorophyllide a and zinc-pheophorbide a, differing only in central metal ion substituting the tetrapyrrole ring. Interactions of these drugs with BCRP and albumin were studied in parallel with the analysis of their impact on the photodynamic efficacy of the PSs.

Transport studies were performed using the MCF-7 cell line (breast cancer) with basal and transiently up-regulated expression of BCRP. In parallel, photodynamic effect induced by the PSs remaining in the cells after a defined period of transport was determined. It was shown that both magnesium- and zinc-substituted derivatives of pheophorbide a are substrates of the transporter, but their transport rate is lower than that of pheophorbide a, which is a previously confirmed substrate of BCRP. Additionally, lower transport rates were observed for chlorophyllide than for zinc pheophorbide. This is most likely due to differences in their affinity to the extracellular loop ECL3 of the transporter. At the same time, it was observed that the transport rate of both derivatives, like that of pheophorbide a, is significantly reduced in the absence of serum/albumin in the extracellular environment, similarly as for other compounds of similar structure. The rate of transport increases with increasing concentration of albumin, reaching a plateau at about 250 µM of the protein. The accelerated transport may be due to the binding of a PS to albumin, which prevents the complex from re-entering the cell. However, this might not be the only mechanism of this phenomenon, since no correlation was observed between the rate of PS transport and its affinity for albumin. It was observed that metal substituted derivatives bind to albumin much stronger than pheophorbide a. Additionally, this binding is stronger for the zinc-substituted derivative than for the magnesium one. Presumably, this difference, rather than the difference in the rate of transport by BCRP as previously speculated, is responsible for the prolonged retention time in the body of the zinc derivative compared to chlorophyllide observed in previous *in vivo* studies.

To thoroughly characterize the binding of the PSs to human serum albumin, spectroscopic and molecular docking studies were performed. Binding constants were determined by the measurement of the PSs fluorescence enhancement with increasing concentration of albumin. Probable binding sites, in turn, were identified by fluorescence quenching studies and molecular docking. These studies showed that chlorophyll derivatives bind most strongly at the heme binding site located in subdomain IB, and weaker at the major albumin binding sites, i.e. Sudlow1 and Sudlow2, located in subdomains IIA and IIIA, respectively. This binding is predominantly based on hydrophobic interactions and, to a lesser extent, hydrogen bonding. The determined binding constants were lower for chlorophyllide than for zinc pheophorbide. Moreover, the number of identified amino acid residues involved in the binding to albumin was lower for the former than for the latter. This suggests that the differences in their pharmacokinetics observed in animals are also likely to occur in humans.

Because of relatively strong binding of zinc pheophorbide a to albumin, which hinders its uptake by cancer cells, and on the other hand high photodynamic potential of this derivative, it was reasonable to investigate whether the complex of albumin with zinc pheophorbide enters vascular endothelial cells, which express the albumin receptor, gp60, involved in the uptake of this protein by endocytosis. The experiments performed using the HUVEC model cell line (endothelial cells isolated from the umbilical vein) confirmed that the complex is incorporated into the cells. Moreover, complexation of the PS with albumin increases its lysosomal accumulation, thus enhancing the induced photodynamic effect. It was also shown that HUVECs are much more susceptible to photodynamic treatment with zinc pheophorbide than MCF-7 cancer cells. The IC50 value for the HUVEC cell line at a light dose of 2 J/cm^2 and a 3-hour accumulation time was about 20 nM, while for the MCF-7 line this value is approx. 25 times higher. It was also shown that the type of cell death induced by photodynamic treatment depends on the level of zinc pheophorbide a accumulated in the cells. At low levels of the PS, cells undergo apoptosis and at high levels, necrosis. Since high concentrations of albumin significantly reduce cellular accumulation of the PS, they will also direct cells into the apoptosis pathway, which may be a beneficial effect, due to the reduction of inflammation.

Imię i nazwisko: Milena Szafraniec   Data: 15.02.2022

Afiliacja: Instytut Immunologii i Terapii Doświadczalnej PAN

Oświadczenie

Oświadczam, że mój udział w następującej pracy:

Milena J. Szafraniec, Leszek Fiedor. One ring is not enough to rule them all. Albumin-dependent, ABCG2-mediated transport of chlorophyll-derived photosensitizers. European Journal of Pharmaceutical Sciences 167 (2021), 106001, https://doi.org/10.1016/j.ejps.2021.106001

jest prawidłowo scharakteryzowany w poniższej tabeli.

Autor	Udział [%]	Opis udziału własnego
Milena Szafraniec	90	opracowanie koncepcji i metodyki badań, przeprowadzenie eksperymentów, analiza i interpretacja wyników, przygotowanie rycin, studia literaturowe i dyskusja wyników, przygotowanie manuskryptu, odpowiedź na recenzję, finalna edycja manuskryptu
Leszek Fiedor	10	opracowanie koncepcji badań, superwizja, edycja manuskryptu

Podpis współautora

Milena Szafraniec

Imię i nazwisko: prof. dr hab. Leszek Fiedor   Data: 3.02.2022

Afiliacja: Uniwersytet Jagielloński, Wydział Biochemii, Biofizyki i Biotechnologii

Oświadczenie

Oświadczam, że mój udział w następującej pracy:

Milena J. Szafraniec, Leszek Fiedor. One ring is not enough to rule them all. Albumin-dependent ABCG2-mediated transport of chlorophyll-derived photosensitizers. *European Journal of Pharmaceutical Sciences* 167 (2021), 106001. https://doi.org/10.1016/j.ejps.2021.106001

jest prawidłowo scharakteryzowany w poniższej tabeli.

Autor	Udział [%]	Opis udziału własnego
Milena Szafraniec	90	opracowanie koncepcji i metodyki badań, przeprowadzenie eksperymentów, analiza i interpretacja wyników, przygotowanie rycin, studia literaturowe i dyskusja wyników, przygotowanie manuskryptu, odpowiedź na recenzję, finalna edycja manuskryptu
Leszek Fiedor	10	opracowanie koncepcji badań, superwizja, edycja manuskryptu

Podpis współautora

Fiedor

Imię i nazwisko: Milena Szafraniec   Data: *15.02.2022*

Afiliacja: Instytut Immunologii i Terapii Doświadczalnej PAN

Oświadczenie

Oświadczam, że mój udział w następującej pracy:

Milena J. Szafraniec, Monika Toporkiewicz, Andrzej Gamian. Zinc-substituted pheophorbide a is a safe and efficient antivascular photodynamic agent. *Pharmaceuticals* (2022)

jest prawidłowo scharakteryzowany w poniższej tabeli.

Autor	Udział [%]	Opis udziału własnego
Milena Szafraniec	85	opracowanie koncepcji i metodyki badań, przeprowadzenie eksperymentów, analiza i interpretacja wyników, przygotowanie rycin, studia literaturowe i dyskusja wyników, przygotowanie manuskryptu, odpowiedź na recenzję, finalna edycja manuskryptu
Monika Toporkiewicz	10	przeprowadzenie eksperymentów, edycja manuskryptu
Andrzej Gamian	5	superwizja, edycja manuskryptu

Podpis współautora

Milena Szafraniec

Imię i nazwisko: Monika Toporkiewicz   Data: _15.02.2022_

Afiliacja: Sieć Badawcza Łukasiewicz – PORT Polski Ośrodek Rozwoju
Technologii we Wrocławiu

Oświadczenie

Oświadczam, że mój udział w następującej pracy:

Milena J. Szafraniec, Monika Toporkiewicz, Andrzej Gamian. Zinc-substituted pheophorbide a is a safe and efficient antivascular photodynamic agent. *Pharmaceuticals* (2022)

jest prawidłowo scharakteryzowany w poniższej tabeli.

Autor	Udział [%]	Opis udziału własnego
Milena Szafraniec	85	opracowanie koncepcji i metodyki badań, przeprowadzenie eksperymentów, analiza i interpretacja wyników, przygotowanie rycin, studia literaturowe i dyskusja wyników, przygotowanie manuskryptu, odpowiedź na recenzję, finalna edycja manuskryptu
Monika Toporkiewicz	10	przeprowadzenie eksperymentów, edycja manuskryptu
Andrzej Gamian	5	superwizja, edycja manuskryptu

Podpis współautora

Monika Toporkiewicz

Imię i nazwisko: prof. dr hab. Andrzej Gamian   Data: 15.02.2022

Afiliacja: Instytut Immunologii i Terapii Doświadczalnej im. Ludwika Hirszfelda PAN

Oświadczenie

Oświadczam, że mój udział w następującej pracy:

Milena J. Szafraniec, Monika Toporkiewicz, Andrzej Gamian. Zinc-substituted pheophorbide a is a safe and efficient antivascular photodynamic agent. *Pharmaceuticals* (2022)

jest prawidłowo scharakteryzowany w poniższej tabeli.

Autor	Udział [%]	Opis udziału własnego
Milena Szafraniec	85	opracowanie koncepcji i metodyki badań, przeprowadzenie eksperymentów, analiza i interpretacja wyników, przygotowanie rycin, studia literaturowe i dyskusja wyników, przygotowanie manuskryptu, odpowiedź na recenzję, finalna edycja manuskryptu
Monika Toporkiewicz	10	przeprowadzenie eksperymentów, edycja manuskryptu
Andrzej Gamian	5	superwizja, edycja manuskryptu

Podpis współautora

DYREKTOR INSTYTUTU

prof. dr hab. Andrzej Gamian

Contents lists available at ScienceDirect

European Journal of Pharmaceutical Sciences

One ring is not enough to rule them all. Albumin-dependent ABCG2-mediated transport of chlorophyll-derived photosensitizers

Milena J. Szafraniec [a,*], Leszek Fiedor [b]

[a] *Łukasiewicz Research Network – PORT Polish Center for Technology Development, Stabłowicka 147, 54-066 Wrocław, Poland*
[b] *Faculty of Biochemistry, Biophysics and Biotechnology, Jagiellonian University, Gronostajowa 7, 30-387 Kraków, Poland*

ABSTRACT

Breast cancer resistance protein (BCRP, ABCG2) is a member of the ATP-binding-cassette (ABC) superfamily of membrane transporters. It is involved in the efflux of a broad range of xenobiotics of highly diverse structures. BCRP activity greatly influences drug distribution in vivo and is often associated with cancer multidrug resistance, which is observed in the case of both chemotherapy and photodynamic therapy. The set of ABCG2 substrates includes porphyrins and chlorins such as heme, hemin, protoporphyrin IX, chlorin e6, pheophorbide a, and their derivatives. Here we provide an evidence that magnesium- and zinc-substituted derivatives of pheophorbide a, which are very promising photosensitizers for use in photodynamic therapy, are also recognized and transported by ABCG2. Interestingly, despite minor structural differences, they clearly differ in the transport rate, both between each other and compared to pheophorbide a. In addition, their transport rate, like those of other structurally similar compounds, is strictly dependent on the level of serum albumin in the extracellular environment. The results that we present here are crucial for the use of metal-substituted pheophorbides in clinical practice but also provide an important insight into the mechanism of porphyrin transport by ABCG2.

1. Introduction

Photodynamic therapy is based on the photoactivation of non-toxic drugs (photosensitizers, PSs) with visible or near-infrared light in order to generate cytotoxic reactive oxygen species in a selected treatment site. Originally developed as an anti-neoplastic therapy, it continues to expand its use in the treatment of benign skin lesions, age-related macular degeneration, as well as the inactivation of pathogenic microorganisms (Effron et al., 2015; Marcus and McIntyre, 2002; Plaetzer et al., 2013). Over last decades, a plethora of PSs have been developed and studied in preclinical and clinical trials (Bellnier et al., 2003; Brandis et al., 2007; Uchoa et al., 2015). Among them, several metal-substituted porphyrins, chlorins, bacteriochlorins and phthalocyanines have been shown to possess ideal photophysical properties for their use in clinics (Josefsen and Boyle, 2008; McFarland et al., 2020; Tuhl et al., 2012). One of them, palladium-metalated bacteriopheophorbide, known by its trade name TOOKAD® (Negma Lerads/-Steba Biotech), has already been approved in Europe and Israel for the treatment of low-risk prostate cancer (Gill et al., 2018). Also metal-substituted derivatives of pheophorbide a (Pheide),

chlorophyllide a (Chlide) and zinc-pheophorbide a (Zn-Pheide) have been thoroughly studied, which revealed their high potential in the treatment of human adenocarcinoma and mouse melanoma (Jakubowska et al., 2013; Szczygieł et al., 2014). Moreover, an in vivo pharmacokinetic study showed a prolonged retention of Zn-Pheide over Chlide in several animal tissues, which is of crucial importance from the point of view of both their therapeutic efficacy and patient safety (Szczygieł et al., 2014, 2008). It has been hypothesized that these differences in the pharmacokinetics of Pheide derivatives are due to the substrate specificity of the membrane transporter ABCG2, which recognizes Chlide but not Zn-Pheide (Szczygieł et al., 2008). This prompted us to further investigate the transport of these two PSs, particularly with regard to the activity of ABCG2, as it has been shown that both Pheide and structurally similar compounds were substrates of this transporter but not of other multidrug transporters, such as Pgp or MRP1 (Jonker et al., 2002; Robey et al., 2004, 2005). Thus, the aim of the present study was to investigate the ABCG2-mediated transport of Chlide and Zn-Pheide and its impact on the photodynamic effect induced with these compounds. For comparison, we used Pheide as a bona fide substrate of ABCG2, which allowed to confirm the functionality of the applied

---

* Corresponding author at: Łukasiewicz Research Network - PORT Polish Center for Technology Development: Siec Badawcza Lukasiewicz - PORT Polski Osrodek Rozwoju Technologii, Poland.
E-mail address: milena.szafraniec@protonmail.com (M.J. Szafraniec).

experimental system and to compare the transport rate of the metal-substituted pheophorbides with their related metal-free compound. We studied the transport and photocytotoxic activity of Pheide and its derivatives (structures shown in Fig. 1) in time-dependent experiments using the sublines of the human breast cancer cell line (MCF-7) differing in ABCG2 expression levels. We chose MCF-7 model, since breast cancer is one of photodynamic therapy targets and its multidrug resistance is primarily due to BCRP activity (Banerjee et al., 2017; Lamberti et al., 2014; Ross et al., 1999). We analyzed the levels of the PSs in the cells by fluorescence measurement and flow cytometry, and correlated them with the efficacy of photodynamic treatment (PDT), assessed by MTT assay. The light dose applied to the cells (2 J/cm^2) was relatively low, as our goal was not to obtain a maximal PDT efficacy, but to compare the PSs on the basis of their transport rate and the corresponding PDT effect. Both, efflux and PDT studies were performed in the presence or absence of the ABCG2-specific inhibitor, fumitremorgin C (FTC). Moreover, ATPase activity was measured in isolated membranes of MCF-7 cells overexpressing ABCG2, to analyze the behavior of the transporter in the presence of the PSs. We also confirmed that, like other compounds of similar structures, the effective transport of Chlide and Zn-Pheide by ABCG2 requires the presence of an extracellular partner which could be serum albumin (Desuzinges-Mandon et al., 2010; Ogino et al., 2011). On the other hand, the complexation with albumin greatly influences their cellular uptake, therefore it should be taken into account when analyzing the transport both inside and outside the cell. Our

findings provide an important insight into the factors regulating the pharmacokinetics of chlorophyll-derived PSs and should be considered when planning their application in clinical practice.

2. Materials and methods

2.1. Photosensitizers

Chlorophyll a was isolated from frozen spinach leaves according to a previously described method (Nowak et al., 2013). Chlide was prepared from chlorophyll a via enzymatic removal of phytol, using a plant enzyme chlorophyllase, according to a previously described procedure (Fiedor et al., 2003). Pheide, in turn, was obtained from Chlide via demetallation with trifluoroacetic acid, and Zn-Pheide was obtained from Pheide via direct metalation with zinc acetate in methanol. All compounds were purified as described earlier and their purity was at least 96% according to HPLC analysis (Szczygieł et al., 2008). The concentrations of the PSs were determined spectrophotometrically in ethanol, using the extinction coefficients at Q$_y$ bands equal to 44,500 M^{-1} cm^{-1} for Pheide and 71,500 M^{-1} cm^{-1} for Chlide and Zn-Pheide. Aliquots of the PSs were stored dry at -20°C under nitrogen atmosphere. For each experiment, fresh solutions of the PSs were prepared by dissolving them in appropriate volumes of DMSO. All experiments were carried out under dim light to prevent degradation of the PSs and uncontrolled photodamage of the cells.

2.2. Cells and transfection

The human breast carcinoma cell line MCF-7 was obtained from the American Type Culture Collection (ATCC, Manassas, VA, USA). The cells were maintained in Dulbecco's modified Eagle's medium (DMEM) supplemented with 10% (v/v) fetal bovine serum (FBS), 2 mM glutamine, 1 mM sodium pyruvate, penicillin (100 units/ml), and streptomycin (100 μg/ml) at 37°C in a humidified atmosphere containing 5% CO$_2$. The full length wild-type cDNA of human ABCG2 (IDT) was inserted into the pcDNA3.1(-) vector (Invitrogen) between the EcoRI and HindIII restriction sites. Then, the pcDNA3.1(-)/ABCG2 construct was subcloned in *E. coli* XL1-Blue and its presence and proper orientation to the CMV promoter was confirmed by sequencing. The cells were transfected with the pcDNA3.1(-)/ABCG2 using Lipofectamine^{TM}2000 Transfection Reagent (Invitrogen) according to the manufacturer's protocol. Selection of transfectants was performed using 500 μg/ml of G418 with further population enrichment by fluorescence-activated cell-sorting using a BD FACSAria cell sorter and cell staining with the anti-human ABCG2 Alexa Fluor 488-conjugated antibody, clone 5D3 (Bio-Techne). As a control, MCF-7 cells were also transfected with the empty pcDNA3.1(-) and selected by cultivation in medium containing 500 μg/ml of G418. The cell subline transfected with the ABCG2 gene was named MCF-7/ABCG2, and the one transfected with the empty vector, MCF-7/mock.

2.3. Cellular accumulation of the photosensitizers

For uptake studies, MCF-7 cells were seeded into a 96-well plate (3×10^4 cells per well) in complete growth medium and incubated overnight for attachment. Then, the PSs were applied to the cells at a concentration of 1 μM in 50 μl of serum-free medium, together with 2.5 μM FTC, to inhibit a potential efflux mediated by BCRP. The cells were incubated for 1, 2, 3, 4, 5, 6, 16 or 24 hours. Afterwards, the cells were rinsed with PBS, the accumulated PS was extracted with 100 μl of ethanol/DMSO mixture (1:1, v/v) and fluorescence emission was measured at 670 nm after the excitation at 430 nm. The measurement was performed using a Spectra Max i3 plate reader (Molecular Devices). The concentrations of the PSs were calculated on the basis of simultaneously obtained calibration curves.
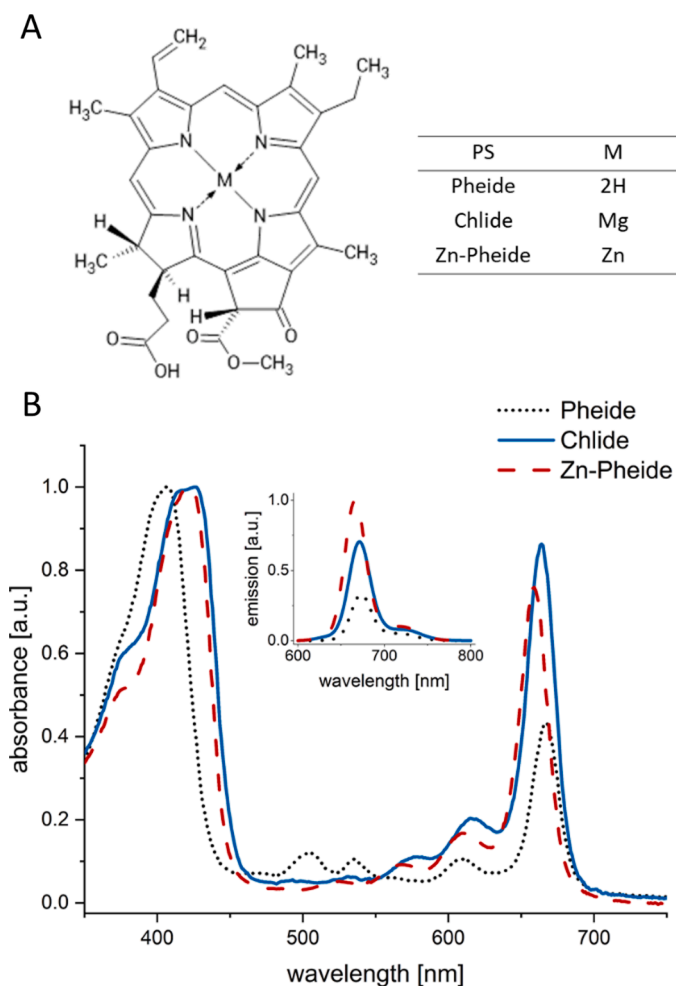

Fig. 1. Chemical structures and nomenclature of the investigated PSs (**A**). Normalized absorption and emission (inset) spectra of Pheide, Chlide and Zn-Pheide recorded in ethanol (**B**). The emission spectra were measured after excitation in the Soret band.

2.4. Plate-based and flow cytometry efflux studies

For efflux studies, MCF-7/mock and MCF-7/ABCG2 cells were seeded into 96-well plates (3 × 10⁴ cells per well) and incubated overnight for attachment. On the other day, the PSs were applied to the cells at a concentration of 1 μM in 50 μl of serum-free DMEM without phenol red and with or without 5 μM FTC. After 3 hours of uptake, the cells were rinsed with PBS and covered with 50 μl of fresh medium containing 10% charcoal-stripped FBS, with or without 5 μM FTC, respectively, and allowed to efflux the PSs. The efflux times were: 0, 0.25, 0.5, 1, 2, 3, 4, 5, 6, 12, 16, 20 and 24 hours. At the end of each efflux period, the cells were rinsed with PBS, the accumulated PS was extracted with 100 μL 1:1 (v/v) ethanol/DMSO mixture and its level was determined by fluorescence measurement using a Spectra Max i3 plate reader (Molecular Devices). All transport experiments were carried out at least twice and within a single experiment the measurements were performed in triplicates.

To examine the distribution of the PSs among the cells after various efflux periods, a flow cytometry experiment was performed. Briefly, MCF-7/mock and MCF-7/ABCG2 cells were seeded into 6-well plates (6 × 10⁵ cells per well) and cultured overnight. Transport of the PSs was analyzed under the same conditions as in the plate-based assay, except that the volume of medium was 1 ml. The efflux times were 0, 0.25, 3 and 24 hours. After the efflux, the cells were trypsinized, fixed with 4% paraformaldehyde and kept at 4°C in the dark until the analysis using a BD LSRFortessa flow cytometer.

To determine the impact of albumin concentration on the transport rate of the PSs, a plate-based efflux assay was performed using pure bovine serum albumin (BSA) at varying concentrations. In this case, after 3 hours of accumulation, MCF-7/ABCG2 cells were allowed to efflux the PSs for 1 hour into phenol-red free DMEM containing fatty acid-free BSA at concentrations of 0, 1, 5, 10, 25, 50 100, 250 or 500 μM. After that, the level of the PSs in cell extracts was measured as described above. The experiment was performed twice, in triplicates.

2.5. Photodynamic treatment and cell viability assessment

For photodynamic experiments, MCF-7/mock and MCF-7/ABCG2 cells were seeded into 96-well plates (3 × 10⁴ cells per well) and incubated overnight for attachment. On the other day, the PSs were applied to the cells at a concentration of 1 μM in serum-free DMEM without phenol red, and with or without 5 μM BCRP inhibitor, fumitremorgin C (FTC). After 3 hours of uptake, the cells were rinsed with PBS and covered with fresh DMEM containing 10% of charcoal-stripped FBS, with or without 5 μM FTC, respectively, and allowed to efflux the PSs. The efflux times were the same as in the plate-based efflux assay. At the end of each efflux period, the cells were rinsed with PBS, covered with 100 μl of HBSS and illuminated with 2 J/cm² using a 1.3 mW/cm² LED illuminator equipped with a 600 nm cut-off filter. After the treatment, the cells were covered with full growth medium and incubated for 48 h at 37°C in the dark. Then, photocytotoxicity (relative viability compared to PS-free cells) was determined by the MTT (3-[4,5-dimethylthiazol-2-yl]-2,5-diphenyltetrazoliumbromide) assay. The same experiment was also conducted in the absence of serum at the efflux stage. Similarly to the plate-based efflux assays, the viability assays were conducted at least twice, in triplicates. Dark cytotoxicity of the PSs was also examined using the MTT assay, after incubation for 3 h in serum-free medium, and after incubation for 24 h both in the presence and absence of 10% serum.

2.6. Albumin binding assay

To investigate the binding of the PSs to BSA, steady state fluorescence binding studies were carried out. Briefly, fatty-acid free BSA (Carl Roth) was dissolved in PBS, pH 7.4, at concentrations equal to 0, 0.125, 0.25, 0.5, 1, 2, 5, 10, 25, 50, 100, 250, 500 and 750 μM. Next, a PS solution in DMSO was added to obtain its concentration of 1 μM. The

final concentration of DMSO in the mixture was 1%. The samples were incubated for 15 min at 37°C to reach equilibrium. After that, fluorescence spectra of the PSs were recorded after excitation at 430 nm using a JASCO FP-8500 spectrofluorometer. The recorded fluorescence maxima were plotted against the concentration of BSA and fitted with rectangular hyperbola in the Origin software, version 2021.

2.7. Albumin-dependent flow cytometry uptake study

To examine whether the PS-BSA complexes are incorporated into the cells, a flow cytometric study was carried out. Briefly, the PSs at a concentration of 1 μM were incubated with 250 μM of fatty acid-free BSA in phenol red-free DMEM at 37°C for 15 min in order to achieve equilibrium. Next, solutions of either free PSs in DMEM or as PS-BSA complexes were applied to MCF-7 cells growing on 6-well culture plates and incubated for 3 hours. After that, the cells were rinsed with PBS containing 0.046% EDTA, trypsinized and collected in 1 mM benzamidine in PBS. Right after trypsinization, the cells were rinsed with cold PBS, fixed with 4% paraformaldehyde and kept at 4°C in the dark until the analysis using a BD LSRFortessa flow cytometer. The experiment was performed in triplicates with 10 000 of cells analyzed in each measurement.

2.8. Isolation of plasma membranes and ATPase assay

For the measurement of ATPase activity, plasma membrane fraction of MCF-7/ABCG2 cells was isolated. Briefly, cell monolayers from five 175 cm² culture flasks were rinsed with PBS, covered with hypotonic buffer (10 mM Tris-HCl pH 7.5, 10 mM KCl, 1 mM MgCl₂, 1 mM benzamidine, 5 μg/ml leupeptin, 5 μg/ml pepstatin A and 1 mM PMSF) and left on ice for ca. 20 minutes. After visible cell disruption, the lysate was harvested and homogenized with a Potter-Elvehjem homogenizer. After centrifugation at 2000 g, the supernatant was further centrifuged at 100,000 g for 30 min. The resulting pellet was suspended in 0.25 M sucrose containing 10 mM Tris-HCl, pH 7.4. The crude membrane fraction was layered over 40% (w/v) sucrose solution and centrifuged at 100,000g for 30 min. The turbid layer at the interface was collected, suspended in 0.25 M sucrose containing 10 mM Tris-HCl, pH 7.5 and centrifuged at 100,000 g for 30 min. The membrane fraction was collected and resuspended in 1 ml of 0.25 M sucrose containing 10 mM Tris-HCl, pH 7.5. Protein concentration was determined using Pierce™ 660nm Protein Assay Reagent (Thermo Fisher Scientific). ATPase activity of the isolated membranes (2.5 μg of total protein) was measured in ATPase assay buffer: 50 mM Tris-HCl pH 7.0, 50 mM KCl, 1 mM ouabain, 2 mM EGTA, 5 mM NaN₃. At first, the measurements were performed at various concentrations of ATP, and then in the presence of 1 mM ATP and various concentrations of the PSs. After the incubation at 37°C for 30 min, the reactions were terminated by the addition of equal volume of 5% SDS solution. The liberated inorganic phosphate (Pi) was measured by the colorimetric reaction with ammonium molybdate in the presence of ascorbic acid (Bartolommei and Tadini-Buoninsegni, 2016). Background samples were prepared by denaturation of the protein with SDS prior to the addition of ATP.

2.9. Statistical analysis

The unpaired Student's t-test was conducted to compare the cellular levels of the PSs and cell viabilities between MCF-7/mock and MCF/ABCG2 cells, as well as between inhibited and uninhibited MCF-7/ABCG2. The same test was used to examine the differences in cellular accumulation of the PSs in the presence and absence of BSA, determined by flow cytometry. The transport rates at various concentrations of BSA, were compared by the two-way Anova followed by Tukey post-hoc analysis to reveal the differences between the particular PSs. The inhibition of ATPase activity in the presence of 100 and 200 μM PSs, in turn, was analyzed for statistical significance using the one-way Anova, also

with Tukey post-hoc test. All statistical analyses were performed in Origin 2021 considering p-values below 0.05 as significant.

3. Results

3.1. Cell transfection

After the transfection and pre-selection with G418, the maximal number of ABCG2-positive cells obtained among various transfection protocols was 30% (according to flow cytometry measurement, data not shown). After further enrichment by FACS, the level of ABCG2-positive cells reached 94%. The cells were tested for ABCG2 activity using the standard ABCG2 substrates, Hoechst 33342 and Pheide (data not shown). The results of flow cytometric analysis of ABCG2 expression in MCF-7/ABCG2 and MCF-7/mock cells are shown in Fig. 2.

3.2. Cellular accumulation of the photosensitizers

The accumulation of the PSs in MCF-7 cells was examined to determine the optimal incubation time for efflux and PDT studies. Since FBS greatly affected the accumulation, the incubation was performed in serum-free medium. To obtain the maximal accumulation, the study was performed in the presence of a specific ABCG2 inhibitor, FTC, the concentration of which was previously optimized (Fig. S1). The amounts of the PSs accumulated in the cells were calculated on the basis of the respective calibration curves. The PSs differed significantly in their accumulation kinetics. Thus, after the first hour of incubation the highest cellular level was observed for Zn-Pheide, and the lowest for Pheide (Fig. 3). Longer incubation times, in turn, resulted in a significant increase in the level of Pheide, while the levels of its metal-substituted derivatives increased only slightly. Despite these differences, it could be observed that after 3 hours of incubation the amounts of the PSs accumulated in the cells were almost equal (Fig. 3). On the basis of this observation, a 3-hour incubation time was set for further experiments.

3.3. Efflux and PDT studies

ABCG2-mediated efflux of the PSs was studied in a 24-hour plate-based assay with fluorometric determination of the PSs after every efflux period. In this assay, the value of fluorescence (after the subtraction of background) recorded from the FTC-inhibited cells at zero time was set as 100% and the values for the subsequent time points were calculated proportionally. Additionally, flow cytometric analyses were performed for selected efflux periods, to visualize the distribution of the PSs among the cells. In parallel, PDT experiments were conducted, by
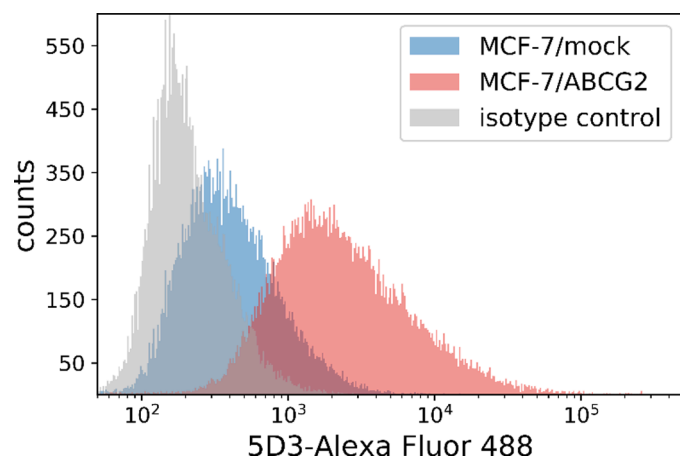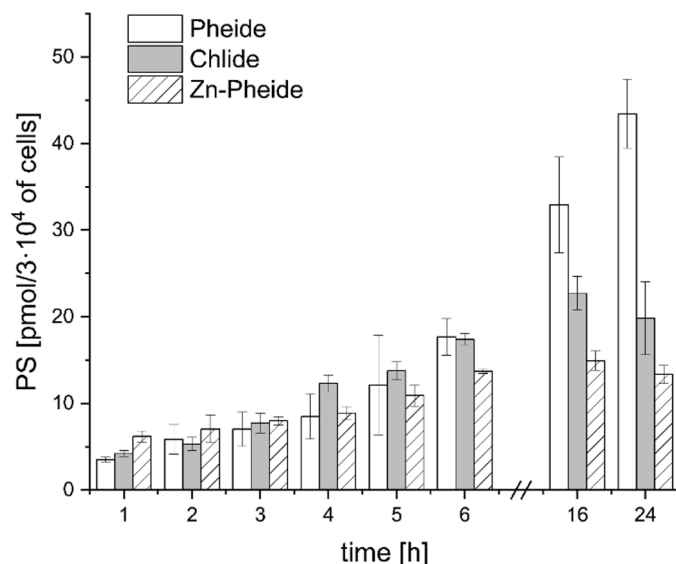

Fig. 3. Accumulation of the PSs in MCF-7 cells in the presence of 2.5 μM ABCG2 inhibitor, FTC.

illuminating the cells after the same efflux periods as in the plate-based efflux assay. The viability of the cells after PDT was assessed by MTT assay and calculated as % of control (PS-free cells). Since a constant number of cells was required to obtain reliable results, all types of experiments were performed with the use of charcoal-stripped FBS, in order to deprive the cells of steroid hormones and thus impair their proliferation (Villalobos et al., 1995; Wiese et al., 1992). For the same reason, phenol-red free DMEM was used, considering that phenol red can act as a weak estrogen, inducing breast cancer cells proliferation (Berthois et al., 1986). The transport in the absence of serum was not analyzed, since long-term serum deprival could lead to reduction of the overall cell viability, including the impairment of membrane transport. However, the results of PDT experiments performed in the absence of serum, when compared to the corresponding experiments with FBS, may serve as an indirect measure of the amount of the PSs in the cells. In these experiments, a separate control was prepared for each time point, which allowed the estimation of the effect induced by the PSs independently of the cell attenuation caused by the lack of serum. For a convenient comparison, the results of the plate-based efflux assays, as well as PDT experiments are summarized in a single panel (Fig. 4), whereas the results of flow cytometry study are presented in Fig. 5. As shown in Fig. S2, at a concentration of the PSs equal to 1 μM, their dark cytotoxicity was not observed for both 3 h and 24 h of incubation. Therefore, the reduction in cell viability in the PDT experiment is due solely to the photodynamic activity of the PSs.

3.3.1. Plate-based efflux assays

All three investigated PSs were to some extent effluxed from the cells in the absence of FBS, already at the accumulation step, as at time zero their levels in MCF-7/mock and uninhibited MCF-7/ABCG2 cells were ~85% and ~75%, respectively (Fig. 4A, B and C). A striking difference between Pheide and its metal-substituted derivatives was its very rapid transport in MCF-7/mock cells during the first 15 minutes after the addition of FBS (Fig. 4A). In this short period, the level of Pheide decreased almost by half, while the corresponding decrease was ~27% for Zn-Pheide and only ~17% for Chlide (Fig. 4B and C). Additionally, in contrast to the metal-substituted PSs, a significant difference in the level of Pheide between MCF-7/mock and MCF-7/ABCG2 cells was only noticeable at time zero. At longer efflux periods, the levels of Pheide in both sublines were virtually the same (Fig. 4A). Whereas, the levels of Chlide and Zn-Pheide, differed significantly between the sublines throughout the experiment (Fig. 4B and C). Approximate half-lives of

Fig. 2. Expression of ABCG2 on the surface of MCF-7/mock and MCF-7/ABCG2 cells. Analysis performed by flow cytometry with the usage of Alexa Fluor 488-conjugated anti-ABCG2 clone 5D3 antibody.
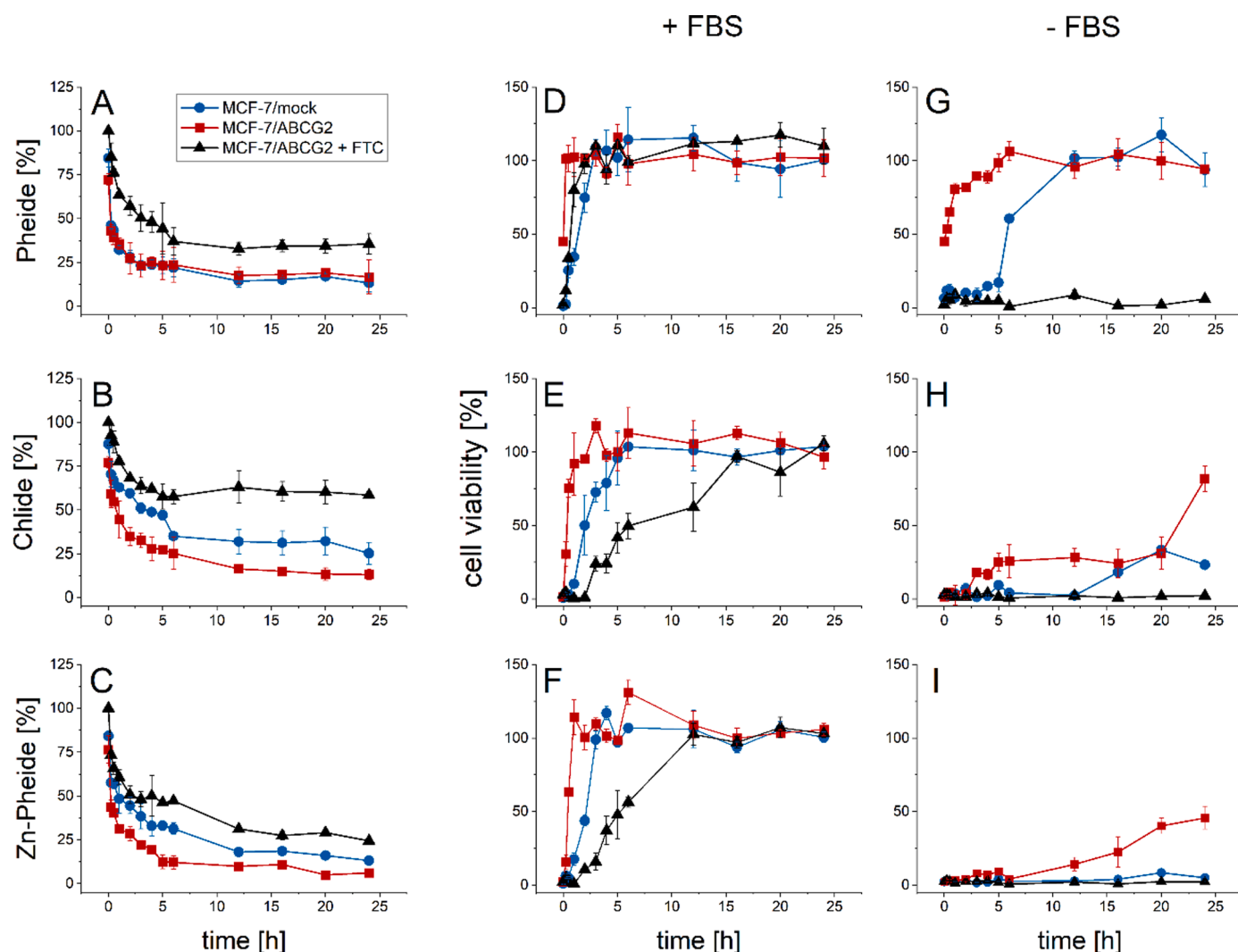
Fig. 4. Efflux (A, B, C) and time-dependent photocytotoxicity (D – I) of the PSs analyzed in MCF-7/mock and MCF-7/ABCG2 cells, with and without ABCG2 inhibitor, 5 μM FTC. The levels of the PSs in the efflux study are presented as a percentage of their initial accumulation (in the presence of 5 μM FTC). For photocytotoxicity study, before illumination the cells were allowed to export the PSs to the medium containing 10% of charcoal-stripped FBS (D, E, F) or to serum-depleted medium (G, H, I). Cell viability after the PDT was determined by MTT assay. The first row of graphs relates to Pheide, the second to Chlide, and the third to Zn-Pheide. The data are presented as mean ± SD from at least three values.

the PSs in MCF-7/mock cells were 15 minutes for Pheide, 3 hours for Chlide and 1 hour for Zn-Pheide. The half-lives in the ABCG2-ovexpressing subline, in turn, were below 15 minutes for Pheide and Zn-Pheide, and about 1 hour for Chlide. The levels of all PSs reached a plateau between 5 and 12 hours of the efflux. The plateau level established at about 18% of Pheide in both sublines (Fig. 4A). Whereas, for Chlide the plateau levels were ~ 30% and 10% and for Zn-Pheide ~18% and 7% in MCF-7/mock and MCF-7/ABCG2 cells, respectively. Importantly, the concentration of FTC used in the uptake study (2.5 μM) was not high enough to fully inhibit the efflux of the PSs in the presence of FBS. Even at 10 μM of FTC, the efflux of all PSs was still significant and did not differ much from that observed at 5 μM. Moreover, incomplete transport inhibition was observed even in the case of MCF-7/mock cells (data not shown). Therefore, 5 μM FTC was applied throughout the efflux and PDT studies. Similarly to the uninhibited cells, the PSs levels in the presence of FTC dropped relatively fast during the first 5 hours, and then reached a plateau which corresponded to ~35% of Pheide, ~60% of Chlide, and ~25% of Zn-Pheide. For most efflux periods, the differences between MCF-7/mock and MCF-7/ABCG2 cells affecting the transport of Chlide and Zn-Pheide were statistically significant (see Supplementary materials, Table S1, column A). Also, significant

differences were observed between the inhibited and uninhibited MCF-7/ABCG2 cells for all PSs (Table S1, column B).

3.3.2. Time-dependent PDT studies

As expected, the viability of the cells after PDT increased over time in the case of all three PSs (Fig. 4D – I). The MCF-7/ABCG2 subline was less susceptible to PDT than control cells, regardless of the PS, and both, in the presence and absence of FBS. However, in the case of Pheide, when FBS was present, the difference between the sublines was noticed only at short efflux periods, similarly as it was in the efflux assay (Fig. 4A and D). FTC increased the susceptibility of the cells to PDT in the case of all three PSs. The inhibition, however, was clearly more pronounced in the absence than in the presence of FBS, as in the former case nearly 100% of the cells were killed by all three PSs and at all efflux periods. The PDT experiments performed in the absence of FBS clearly show that the transport rate of all three PSs at serum-free conditions was reduced but not completely abolished. Importantly, a visible difference occurred between Pheide-treated MCF-7/mock and MCF-7/ABCG2 cells in the viability profiles obtained at FBS-free conditions, which was not observed when FBS was present (Fig. 4D and G). As shown in Supplementary materials, the differences between MCF-7/mock and MCF-7/
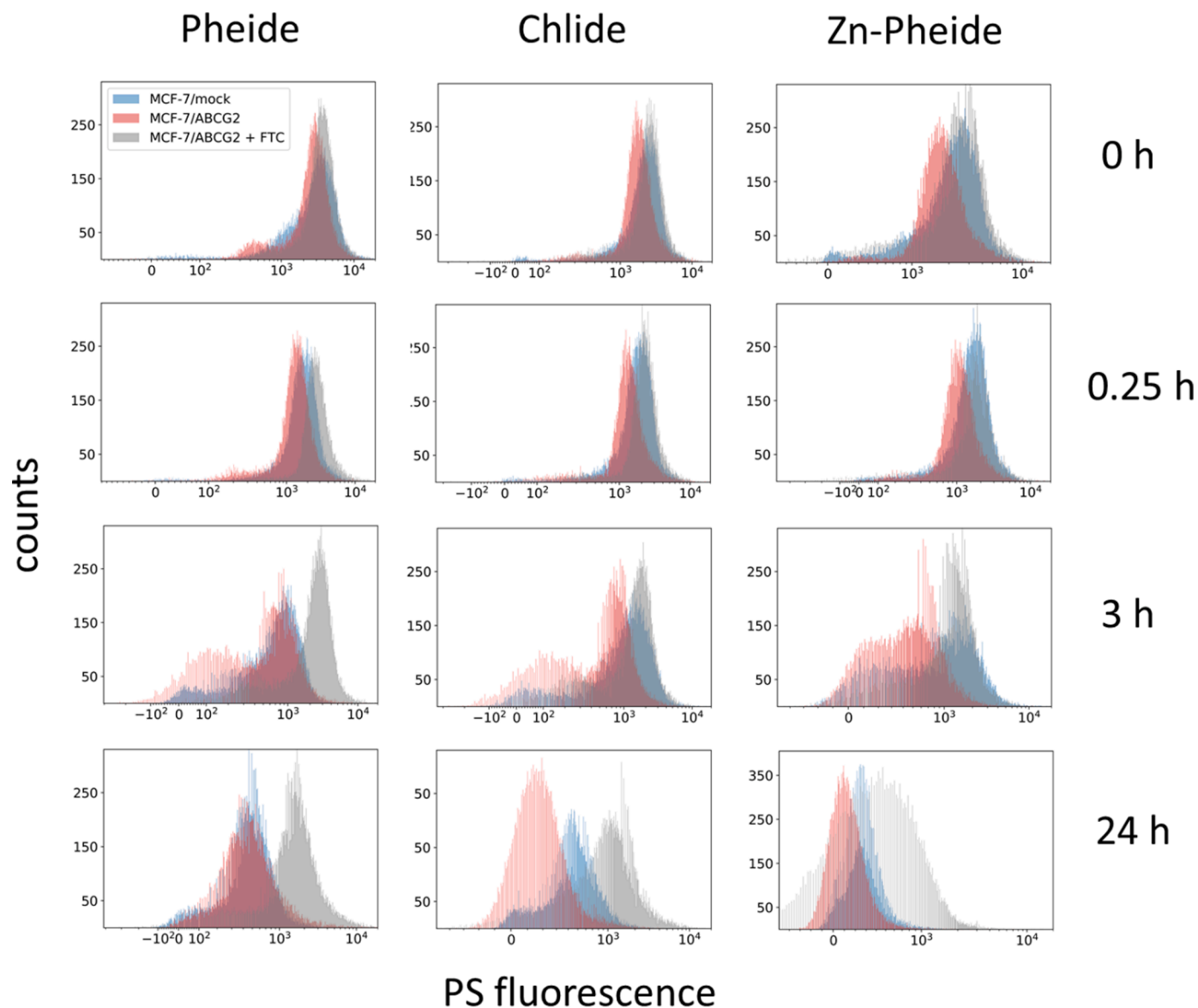
Fig. 5. Representative histograms from the flow cytometry transport study (see the text for details).

ABCG2 as well as between inhibited and uninhibited MCF-7/ABCG2 cells were statistically significant at shorter efflux periods in the presence of FBS and at longer efflux periods in the absence of FBS (Tables S2 and S3).

3.3.3. Flow cytometry transport studies

The results obtained by flow cytometry were largely consistent with the ones of the plate-based assay. Both MCF-7 sublines transported all three PSs and the transport was inhibited by FTC, though at longer incubation times, the efflux was noticed even in the inhibited cells. The populations of MCF-7/mock and MCF-7/ABCG2 transporting Pheide were to a large extent overlapping, while for Chlide and Zn-Pheide their separation was observed. After 3 hours of efflux, the slowly and rapidly-transporting subpopulations of both the MCF-7/mock and MCF-7/ABCG2 cells could be distinguished, which resulted from the uneven ABCG2 expression within the sublines (Fig. 5).

3.4. Albumin binding assay

Since we observed that both the uptake and efflux of the PSs depend on the concentration of BSA and this dependence is different for each PS,

we decided to describe the binding of the PSs to albumin quantitatively, by determining their apparent dissociation constants (K_{app}). We took advantage of the fact that the fluorescence of the PSs is enhanced upon their binding to the protein. This is because BSA promotes solubilization of PS aggregates formed in aqueous media. We measured the fluorescence spectra of the PSs in PBS, pH 7.4 at increasing concentrations of BSA and plotted the obtained fluorescence maxima against BSA concentration. Since Chlide and Zn-Pheide show a significant fluorescence in aqueous media even in their unbound form, to calculate the dissociation constants, the signal from their albumin-bound fraction had to be separated from that of free PS. We therefore performed a correction which is fully described in Supplementary materials. Since unbound Pheide in PBS emits only very weak fluorescence, it could be neglected. The corrected plots are shown in Fig. 6A. No non-specific binding was observed and the single binding site model was found to best approximate the obtained results ($R^2 > 0.99$, in each case). The calculated K_{app} are shown in Fig. 6A. Among the investigated PSs, Zn-Pheide showed the strongest affinity to BSA ($K_{app} = 3.8$ μM), Chlide bound moderately ($K_{app} = 5.5$ μM), while Pheide showed only a very weak binding ($K_{app} = 26$ μM). It should be noted, however, that these values of K_{app} can differ from the corresponding intrinsic dissociation constants, particularly for
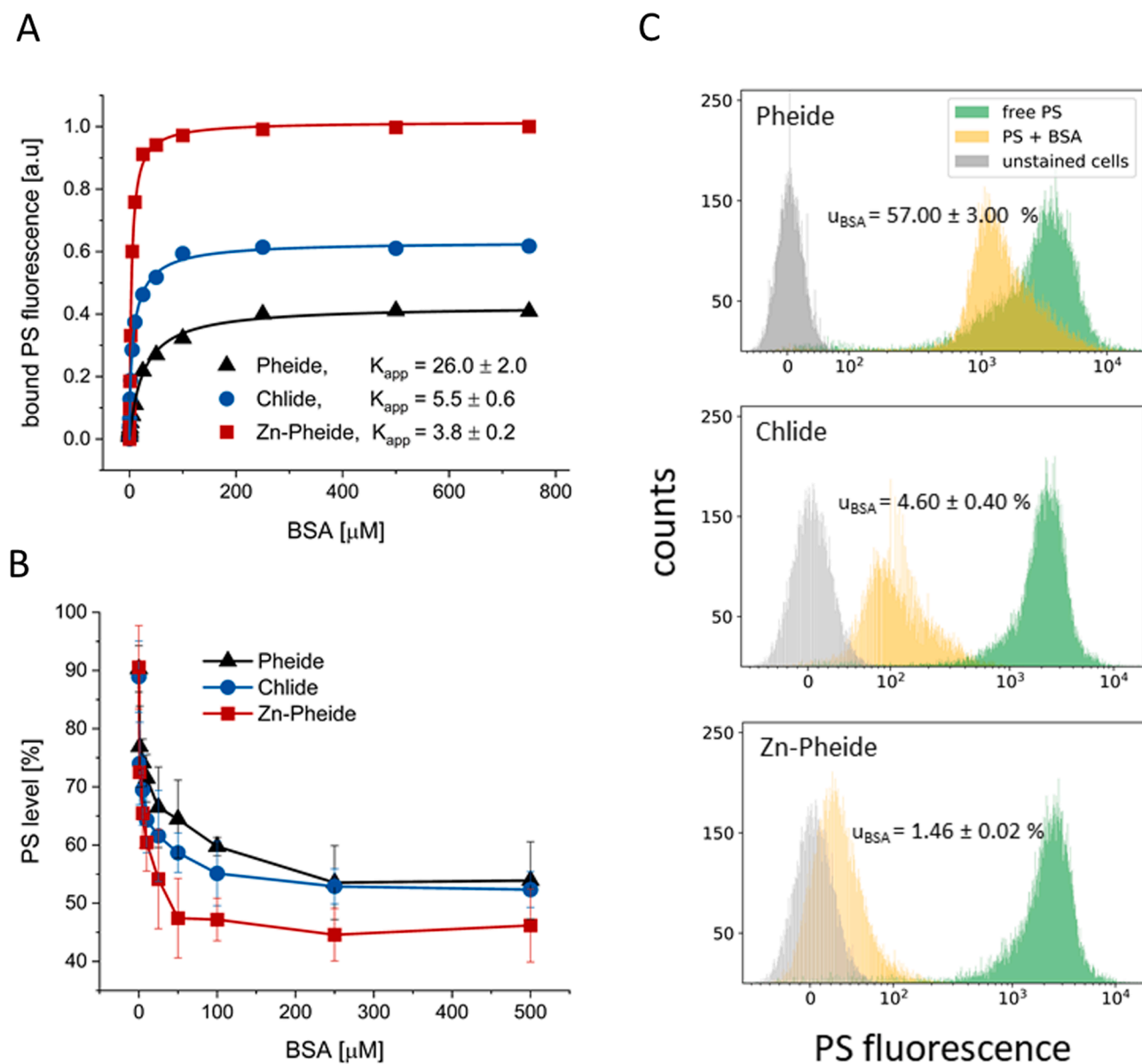
Fig. 6. A) Binding of the PSs to BSA and the calculated apparent dissociation constants (K_{app}). Solid lines are curve-fitting results assuming 1:1 binding. **B)** The levels of the PSs in MCF-7/ABCG2 cells after 1 hour of efflux in the presence of various concentrations of BSA. The values on y axis are calculated as a percentage of the initial PS content (at the end of 3-hour uptake). The data are presented as mean ± SD, $n = 6$. **C)** Representative histograms showing the cellular accumulation of the PSs (1 μM) in the presence (yellow histograms) and absence (green histograms) of 250 μM BSA in the culture medium. The percentage of the PS uptake in the presence of BSA compared to the uptake of free PS (100 %) was indicated as u_{BSA} and calculated on the basis of mean fluorescence intensity ($n = 3$). The differences between the BSA-containing and BSA-free samples were statistically significant ($p < 0.05$).

Pheide, as at physiological conditions (1% DMSO used in the binding assays) this PS may be more prone to self-association than to BSA binding.

3.5. Albumin-dependent efflux and uptake studies

The plate-based efflux assay carried out at various concentrations of BSA showed that the transport rate of all three PSs increases with increasing concentration of BSA and the maximal rate of transport is reached at ~250 μM of BSA for all of them (Fig. 6B). The decrease in the cellular level of all PSs with increasing concentration of BSA was found to be statistically significant. The greatest impact of BSA on the transport rate was observed in the case of Zn-Pheide, for which a ~44% decrease in 500 μM BSA-containing cells compared to BSA-free cells was observed. The corresponding values for Chlide and Pheide were close to

37%. The difference in the impact of albumin between Zn-Pheide and the other two PSs was also found to be statistically significant. A rapid increase in the transport rate was observed when BSA concentration increased from 0 to ~50 μM. Further increase of BSA concentration did not affect much the transport rate. This shows that the transport rates observed in the time-dependent transport studies were only slightly lower than the maximal rates, since BSA concentration in 10% FBS is about 50 – 65 μM. Flow cytometric uptake study, performed at the saturating concentration of BSA (250 μM) confirmed the notion that the affinity to albumin in inversely correlated to the cellular accumulation of the PSs (Fig. 6C).

3.6. ATPase activity

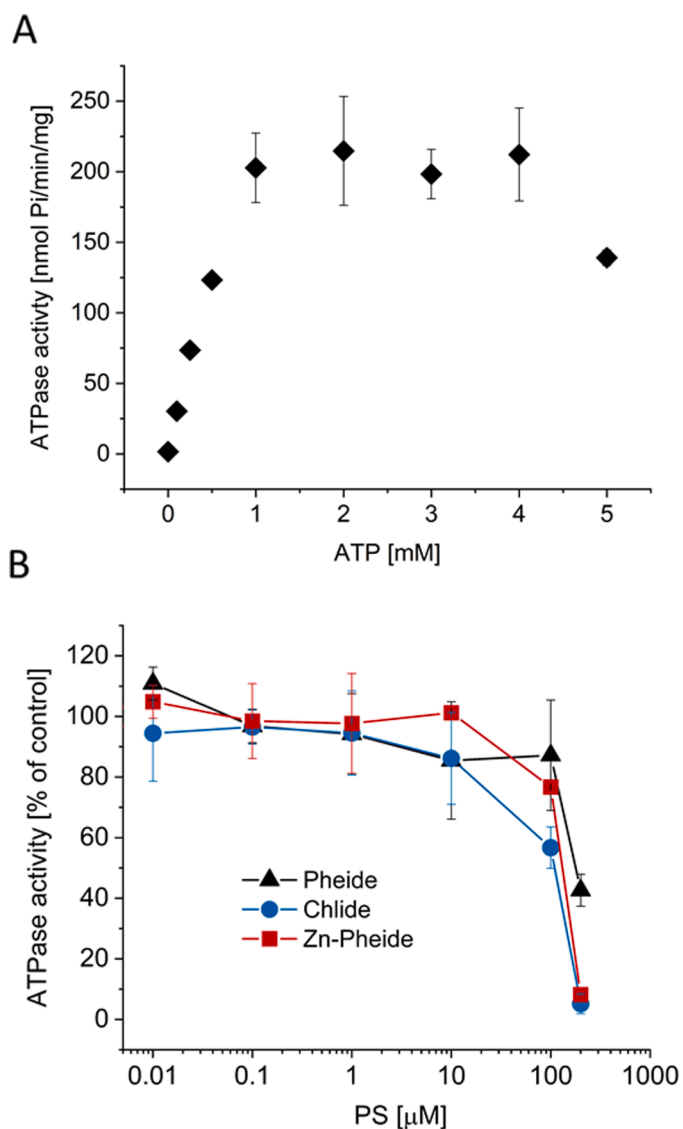As seen in Fig. 7A, the ATPase activity of isolated MCF-7/ABCG2

Fig. 7. ATPase activity of the isolated MCF-7/ABCG2 membranes. **A)** ATP-dependent ATPase activity. **B**) PS-dependent ATPase activity in the presence of 1 mM ATP. The data are presented as mean $\pm$ SD from three values.

membranes was a function of ATP concentration. The highest values of the ATPase activity were observed in the range 1 – 4 mM ATP, therefore to analyze the PS-dependent ATPase activity, the concentration of 1 mM ATP was chosen. Low concentrations of the PSs had virtually no effect on the ATPase activity, whereas at high concentrations (starting from 100 μM) a decrease was observed for all three PSs. Its values, expressed as % of the basal activity were 87% for Pheide, 57% for Chlide and 77% for Zn-Pheide. Further decrease of the ATPase activity was observed at 200 μM concentration of the PSs, reaching 43%, 5% and 8% for Pheide, Chlide and Zn-Pheide, respectively (Fig. 7B). Importantly, we did not observe a biphasic effect of Pheide on ABCG2 previously seen in the High Five insect cell membranes (Wu et al., 2007). In addition, the decrease in the activity was much slower than in that case. Statistical analysis revealed that at the concentration of 100 μM, Chlide inhibited the ATPase activity significantly stronger that the other two PSs. At the concentration of 200 μM, in turn, the metal-substituted PSs acted significantly stronger than Pheide.

4. Discussion

The present study demonstrates that, in spite of very similar

structures, the investigated chlorophyll derivatives differ significantly in their pharmacokinetics. This is due to differences in the kinetics of their cellular absorption, interaction with the ABCG2 transporter, as well as binding to serum albumin. Efflux and PDT assays performed in MCF-7 cells showed that all PSs are transported by ABCG2 and this transport depends on the concentration of albumin in the extracellular space. We took into account that the studied PSs might undergo metabolic conversion in the cells, which would interfere with both transport and PDT studies. However, numerous observations indicate that membrane transport rather than metabolic conversion is the determinant of intracellular PS level. Firstly, clear differences in viability between the Pheide-treated MCF-7/mock, uninhibited and inhibited MCF-7/ABCG2 sublines (Fig. 4G) demonstrate that degradation of the porphyrin ring over the course of the experiment is negligible. Secondly, since after reaching a plateau, the level of Chlide did not decrease further (Fig. 4B), apparently its demetallation inside the cells does not occur. And because Zn-Pheide is more resistant to demetallation than Chlide, it is reasonable to assume that also the former one remains in its unchanged form (Szczygieł et al., 2008).

Since there was virtually no difference in Pheide transport between MCF-7/mock and MCF-7/ABCG2 cells (Fig. 4A) and, moreover, transport of all PSs was not completely inhibited by FTC in the presence of FBS, the involvement of another membrane transporter could also be suspected. However, we consider this unlikely for two reasons. Firstly, Pheide has been shown to be a specific substrate of ABCG2, at least not transported by the other most common multidrug transporters, Pgp and MRP1 (Robey et al., 2004). Secondly, in the absence of FBS we observed no viability of the cells treated with FTC (Fig. 4G – I), even in the case of Pheide, which is a relatively weak PS. This suggests a complete inhibition, and since FTC is considered a specific inhibitor of ABCG2, this transporter is probably the only one involved (Rabindran et al., 2000). Therefore, we suggest that the equal transport of Pheide by the control and ABCG2-ovexpressing cells results simply from its very high transport rate, due to which ABCG2 is not saturated, even if its expression is low. At the same time, intracellular Pheide cannot drop below a certain level which is regulated by its binding to intracellular structures, e.g. mitochondria (Tang et al., 2006). In contrast to Pheide, significant differences were observed in the transport rates between MCF-7/mock and MCF-7/ABCG2 for the metal-substituted PSs (Fig. 4B and C). This demonstrates that ABCG2-mediated transport of Chlide and Zn-Pheide is slower than that of Pheide. The transport of all PSs was significantly accelerated by albumin. This acceleration was shown to be the same for Pheide and Chlide but significantly stronger for Zn-Pheide (Fig. 6B). However, taking into account the impaired reabsorption of the PSs due to their binding to albumin (Fig. 6C), we postulate that the impact of albumin on the transport process itself is the same for all studied compounds. The lack of difference between Chlide and Pheide, however, confirms that the former is transported much slower than the latter.

It is already known that the transport of porphyrin compounds by ABCG2 involves their transfer onto albumin via the large extracellular loop ECL3. Our studies confirm this notion, as the export of the PSs was diminished when the medium was deprived of serum, and greatly enhanced when serum was added. This was probably because in the absence of serum, PS molecules that occupied ECL3 could not be easily removed, and further transport through ABCG2 was blocked. The dissociation constant of Pheide to ECL3 has already been determined and is equal to 3.4 ± 0.5 μM (Desuzinges-Mandon et al., 2010). Also the interaction of Pheide with BSA has been analyzed, revealing the association constant at pH 7.4 and 37°C equal to 8.97×10^4 M^{-1}, which corresponds to $K_d = 11.1$ μM (Ye et al., 2013). It should be noted that the authors performed the binding experiments at ~17% dimethylformamide concentration, which ensured a complete disaggregation of Pheide, therefore they determined the intrinsic dissociation constant, which is lower from the apparent dissociation constant determined in the present study (26 μM), and which is probably more useful for efflux analysis, since in this case Pheide is likely to be received from ECL3 in its

monomer form. Still, however, the binding of Pheide to BSA is much weaker than to ECL3. Therefore, considering the fact that a great transport acceleration of Pheide is observed upon the addition of FBS, it appears that although the presence of albumin increases the rate of transport, the affinity of the PS to albumin is of minor importance to the transfer from ECL3 to albumin and that this transfer is not a competition. Rather the opposite can take place, namely, weaker albumin complexation promotes faster transport, as an easily dissociating albumin-PS complex gives a large number of free albumin molecules ready for the next transport round. Basing on this assumption, and considering only first 15 minutes of the transport studies, when the reabsorption of the PSs can be neglected, a conclusion arises that the binding to ECL3 is the strongest for Chlide, moderate for Zn-Pheide, and the weakest for Pheide. This is not surprising, since ECL3 region is hydrophilic in nature (Khunweeraphong et al., 2017). A similar situation was observed for zinc and cobalt-substituted derivatives of protoporphyrin IX (PPIX), which are bound to ECL3 much stronger than PPIX itself (Desuzinges-Mandon et al., 2010).

On the basis of the results obtained, we conclude that even in the cases of severe hypoalbuminemia (albumin level below 10 g/l = 151 μM), ABCG2-mediated transport of the PSs will remain virtually unchanged (Zemlin et al., 2009). However, significantly lowered albumin concentration in serum will result in an increase of free PS fraction, which can be easily absorbed by the cells either via passive diffusion or receptor-independent endocytosis. Obviously, the absorption will occur not only in lesions but throughout the body, also in the liver, where the PSs are likely to undergo metabolic conversion. This is particularly important while considering the application of the PSs in cancer treatment and in patients malnourished or with severe liver diseases, since albumin levels in these disorders can be significantly reduced (Carr and Guerra, 2017; Carvalho and Machado, 2018; Lee et al., 2015; Navalkele et al., 2016; Takaaki et al., 2020). It cannot be excluded that the PSs are transferred by ABCG2 not only to albumin but also to other serum components such as hemopexin or lipoproteins. Thus, their transport rates in a living organism may be somewhat different than observed in the present study. However, as albumin constitutes the bulk of serum proteins, we hypothesize that its role in the transport as well as in cellular accumulation of the PSs is predominant.

When analyzing the cellular transport *in vitro*, at some point an equilibrium occurs between the BCRP-mediated active transport and the backflow absorption, which is observed as a plateau in the transport profiles (Fig. 4 A-C). It may seem that in a living organism, where there is a constant flow of free (unbound) albumin and other blood proteins, the effluxed PSs can be easily expelled, without their reabsorption, therefore a complete removal of the PSs from the cell might be achieved in a relatively short time. On the other hand, however, it is well known that the majority of albumin is present not in the circulation but in the interstitial space, where its flow is not as intense as in the bloodstream and once entered the interstitium, albumin requires about 24 h to return to the plasma compartment (Levitt and Levitt, 2016, Prinsen and De Sain-Van Der Velden, 2004). Moreover, when it comes to solid tumors, they are commonly equipped with an immature, highly permeable vasculature with a concomitant poor and disorganized lymphatic network, which results in vascular leakage and the accumulation of macromolecules (> 40 kDa) within the interstitium. This is known as the enhanced permeation and retention phenomenon (Carmeliet and Jain, 2000; Merlot et al., 2014; Welter and Rieger, 2013). We postulate that such a microenvironment, at least partially resembles our model system of cultured cells, incubated for several hours without a medium exchange. The PS fraction bound to albumin will remain in the interstitium for a long time, and only its free fraction will be able to diffuse back into the circulation and get expelled from the organism. And as we show, even at saturating concentration of albumin, the PSs are still able to enter the cells, therefore the inward and outward transport cycles will repeat, and the PS level inside the cell will remain in equilibrium. We also postulate that the previously observed long retention of Zn-Pheide

in the tissues results exactly from its accumulation in interstitium in an albumin-complexed form, not as previously hypothesized, from being unrecognized by ABCG2 (Szczygieł et al., 2008). Free fraction of a weaker albumin binder, Chlide, is larger than that of Zn-Pheide, therefore the former is more likely to leave the interstitium and be excreted from the organism than the latter.

According to the recently proposed mechanism of ABCG2 activity, there are two substrate-binding cavities in the structure of the transporter: the larger central cavity formed primarily by the transmembrane helices and the smaller upper cavity, being a part of the extracellular polar lid, in which ECL3 is a major structural element. These two cavities are separated by a di-leucine valve, which determines substrate access to the upper cavity (Khunweeraphong et al., 2019; Orlando and Liao, 2020). Both, the valve and the lid are elements that control the rate of substrate transport. Since no correlation was observed between the affinity of the PSs to albumin and their transport rates, it is likely that albumin not only receives the substrate from BCRP but also participates directly in the transport by influencing the conformation of the transporter. This hypothesis is very plausible because, firstly, albumin has been shown to bind directly to ECL3 and, secondly, it also accelerates the transport of substrates that do not bind to it (Deng et al., 2016; Desuzinges-Mandon et al., 2010). An issue worth considering is also the inhibition of ABCG2 by FTC in the presence of serum. The observed weak inhibition of chlorophyll derivatives efflux by FTC in the presence of FBS might simply result from the fact that the concentration of the inhibitor was not high enough to block all ABCG2 molecules. However, since no significant increase in inhibition was observed with increasing concentrations of FTC, it is suspected that the inhibitory activity of FTC in the presence of serum is diminished. The mechanism of action of Ko143, a BCRP inhibitor closely related to FTC, has already been revealed. It is bound to the central inward-facing cavity of ABCG2, blocking access for substrates and preventing conformational changes required for ATP hydrolysis (Jackson et al., 2018). Assuming that the mechanism of FTC inhibition is similar to that of Ko143, it seems likely that albumin counteracts the inhibitory activity of FTC by promoting the outward-facing conformation of the transporter. However, contradictory results were obtained by examining the inhibition of PPIX transport by FTC in the presence of albumin, as the efflux of PPIX was inhibited completely (Ogino et al., 2011). This aspect therefore requires further detailed research.

The fastest decrease of ATPase activity with PS concentration was found for Chlide, slightly slower for Zn-Pheide, and the slowest for Pheide (Fig. 7B). Interestingly, this order of inhibitory activities (Chlide > Zn-Pheide > Pheide) corresponds with the order of putative affinities to ECL3. This can also give an insight into the studies on the mechanism of porphyrin transport by BCRP, which is so far poorly understood.

CRediT authorship contribution statement

Milena J. Szafraniec: Conceptualization, Methodology, Investigation, Formal analysis, Writing – original draft, Writing – review & editing, Visualization. **Leszek Fiedor:** Conceptualization, Supervision.

Centre (2015/19/N/NZ1/00578).

Supplementary materials

Supplementary material associated with this article can be found, in the online version, at doi:10.1016/j.ejps.2021.106001.

References

Banerjee, S.M., MacRobert, A.J., Mosse, C.A., Periera, B., Bown, S.G., Keshtgar, M.R.S., 2017. Photodynamic therapy: Inception to application in breast cancer. The Breast 31, 105–113. https://doi.org/10.1016/j.breast.2016.09.016.

Bartolommei, G., Tadini-Buoninsegni, F., 2016. Antimony-phosphomolybdate ATPase assay. In: Bublitz, M. (Ed.), P-Type ATPases Methods Protoc. Springer New York, New York, NY, pp. 111–120. https://doi.org/10.1007/978-1-4939-3179-8_12.

Bellnier, D.A., Greco, W.R., Loewen, G.M., Nava, H., Oseroff, A.R., Pandey, R.K., Tsuchida, T., Dougherty, T.J., 2003. Population pharmacokinetics of the photodynamic therapy agent 2-[1-hexyloxyethyl]-2-devinyl pyropheophorbide-a in cancer patients. Cancer Res. 63, 1806–1813. https://cancerres.aacrjournals.org/content/63/8/1806.

Berthois, Y., Katzenellenbogen, J.A., Katzenellenbogen, B.S., 1986. Phenol red in tissue culture media is a weak estrogen: Implications concerning the study of estrogen-responsive cells in culture. Proc. Natl. Acad. Sci. U. S. A. 83, 2496–2500. https://www.jstor.org/stable/27311.

Brandis, A.S., Salomon, Y., Scherz, A., 2007. Chlorophyll Sensitizers in Photodynamic Therapy. Chlorophylls and Bacteriochlorophylls. Springer Netherlands, pp. 461–483. https://doi.org/10.1007/1-4020-4516-6_32. https://doi.org/10.1007/1-4020-4516-6_32.

Carmeliet, P., Jain, R.K., 2000. Angiogenesis in cancer and other diseases. Nature 407, 249–257. https://www.nature.com/articles/35025220.

Carr, B.I., Guerra, V., 2017. Serum albumin levels in relation to tumor parameters in hepatocellular carcinoma patients. Int. J. Biol. Markers. 32, e391–e396. https://doi.org/10.5301/ijbm.5000300.

Carvalho, J.R., Machado, M.V., 2018. New insights about albumin and liver disease. Ann. Hepatol. 17, 547–560. https://doi.org/10.5604/01.3001.0012.0916.

Deng, F., Sjöstedt, N., Kidron, H., 2016. The effect of albumin on MRP2 and BCRP in the vesicular transport assay. PLoS One 11, 1–15. https://doi.org/10.1371/journal.pone.0163886.

Desuzinges-Mandon, E., Arnaud, O., Martinez, L., Huché, F., Di Pietro, A., Falson, P., Di Pietro, A., Falson, P., 2010. ABCG2 transports and transfers heme to albumin through its large extracellular loop. J. Biol. Chem. 285, 33123–33133. https://doi.org/10.1074/jbc.M110.139170.

Effron, J.S., Aliazzi, H., Garcia-Zuazaga, J., 2015. Current evidence and applications of photodynamic therapy in dermatology: Part 1: Cutaneous neoplasms. J. Dermatol. Nurses. Assoc. 7, 145–151. https://doi.org/10.1097/JDN.0000000000000128.

Fiedor, L., Stąsiek, M., Myśliwa-Kurdziel, B., Strzałka, K., 2003. Phytol as one of the determinants of chlorophyll interactions in solution. Photosynth. Res. 78, 47–57. https://doi.org/10.1023/A:1026042005536.

Gill, I.S., Azzouzi, A.R., Emberton, M., Coleman, J.A., Coeytaux, E., Scherz, A., Scardino, P.T., 2018. Randomized trial of partial gland ablation with vascular targeted phototherapy versus active surveillance for low risk prostate cancer: extended followup and analyses of effectiveness. J. Urol. 200, 786–793. https://doi.org/10.1016/j.juro.2018.05.121.

Jackson, S.M., Manolaridis, I., Kowal, J., Zechner, M., Taylor, N.M.I., Bause, M., Bauer, S., Bartholomaeus, R., Bernhardt, G., Koenig, B., Buschauer, A., Stahlberg, H., Altmann, K.H., Locher, K.P., 2018. Structural basis of small-molecule inhibition of human multidrug transporter ABCG2. Nat. Struct. Mol. Biol. 25, 333–340. https://doi.org/10.1038/s41594-018-0049-1.

Jakubowska, M., Szczygieł, M., Michalczyk-Wetula, D., Susz, A., Stochel, G., Elas, M., Fiedor, L., Urbanska, K., 2013. Zinc-pheophorbide a-Highly efficient low-cost photosensitizer against human adenocarcinoma in cellular and animal models. Photodiagnosis Photodyn. Ther. 10, 266–277. https://doi.org/10.1016/j.pdpdt.2012.12.004 https://doi.org/.

Jonker, J.W., Buitelaar, M., Wagenaar, E., Van der Valk, M.A., Scheffer, G.L., Scheper, R.J., Plösch, T., Kuipers, F., Oude Elferink, R.P.J., Rosing, H., Beijnen, J.H., Schinkel, A.H., 2002. The breast cancer resistance protein protects against a major chlorophyll-derived dietary phototoxin and protoporphyria. Proc. Natl. Acad. Sci. U. S. A. 99, 15649–15654. https://doi.org/10.1073/pnas.202607599.

Josefsen, L.B., Boyle, R.W., 2008. Photodynamic therapy and the development of metal-based photosensitisers. Met. Based. Drugs. 2008 https://doi.org/10.1155/2008/276109.

Khunweeraphong, N., Stockner, T., Kuchler, K., 2017. The structure of the human ABC transporter ABCG2 reveals a novel mechanism for drug extrusion. Sci. Rep. 7, 1–15. https://doi.org/10.1038/s41598-017-11794-w.

Khunweeraphong, N., Szöllősi, D., Stockner, T., Kuchler, K., 2019. The ABCG2 multidrug transporter is a pump gated by a valve and an extracellular lid. Nat. Commun. 10, 1–14. https://doi.org/10.1038/s41467-019-13302-2.

Lamberti, M.J., Rumie Vittar, N.B., Rivarola, V.A., 2014. Breast cancer as photodynamic therapy target: Enhanced therapeutic efficiency by overview of tumor complexity. World J. Clin. Oncol. 5, 901–907. https://doi.org/10.5306/wjco.v5.i5.901.

Lee, J.L., Oh, E.S., Lee, R.W., Finucane, T.E., 2015. Serum Albumin and Prealbumin in Calorically Restricted, Nondiseased Individuals: A Systematic Review. Am. J. Med. 128, 1023.e1–1023.e22. https://doi.org/10.1016/j.amjmed.2015.03.032.

Levitt, D.G., Levitt, M.D., 2016. Human serum albumin homeostasis : a new look at the roles of synthesis, catabolism, renal and gastrointestinal excretion, and the clinical value of serum albumin measurements. Int. J. Gen. Med. 9, 229–255. https://doi.org/10.2147/IJGM.S102819.

Marcus, S.L., McIntyre, W.R., 2002. Photodynamic therapy systems and applications. Expert Opin. Emerg. Drugs. 7, 321–334. https://doi.org/10.1517/14728214.7.2.321.

McFarland, S.A., Mandel, A., Dumoulin-White, R., Gasser, G., 2020. Metal-based photosensitizers for photodynamic therapy: the future of multimodal oncology? Curr. Opin. Chem. Biol. 56, 23–27. https://doi.org/10.1016/j.cbpa.2019.10.004.

Merlot, A.M., Kalinowski, D.S., Richardson, D.R., 2014. Unraveling the mysteries of serum albumin-more than just a serum protein. Front. Physiol. 5, 1–7. https://doi.org/10.3389/fphys.2014.00299.

Navalkele, P., Belgrave, K., Altinok, D., Bhambhani, K., Taub, J.W., Wang, Z.J., 2016. Hypoalbuminemia associated with neuroblastoma : a single institution experience. Ann. Pediatr. Child Heal. 4, 1–5. https://www.jscimedcentral.com/Pediatrics/pediatrics-4-1115.pdf.

Nowak, P., Michalik, M., Fiedor, L., Woźniakiewicz, M., Kościelniak, P., 2013. Capillary electrophoresis as a tool for a cost-effective assessment of the activity of plant membrane enzyme chlorophyllase. Electrophoresis 34, 3341–3344. https://doi.org/10.1002/elps.201300304.

Ogino, T., Kobuchi, H., Munetomo, K., Fujita, H., Yamamoto, M., Utsumi, T., Inoue, K., Shuin, T., Sasaki, J., Inoue, M., Utsumi, K., 2011. Serum-dependent export of protoporphyrin IX by ATP-binding cassette transporter G2 in T24 cells. Mol. Cell. Biochem. 358, 297–307. https://doi.org/10.1007/s11010-011-0980-5.

Orlando, B.J., Liao, M., 2020. ABCG2 transports anticancer drugs via a closed-to-open switch. Nat. Commun. 11, 1–11. https://doi.org/10.1038/s41467-020-16155-2.

Plaetzer, K., Berneburg, M., Kiesslich, T., Maisch, T., 2013. New applications of photodynamic therapy in biomedicine and biotechnology. Biomed Res. Int. 2013, 1–3. https://doi.org/10.1155/2013/161362.

Prinsen, B.H.C.M.T., De Sain-Van Der Velden, M.G.M., 2004. Albumin turnover: experimental approach and its application in health and renal diseases. Clin. Chim. Acta. 347, 1–14. https://doi.org/10.1016/j.cccn.2004.04.005.

Rabindran, S.K., Ross, D.D., Doyle, L.A., Yang, W., Greenberger, L.M., 2000. Fumitremorgin C reverses multidrug resistance in cells transfected with the breast cancer resistance protein. Cancer Res. 60, 47–50. https://cancerres.aacrjournals.org/content/60/1/47.

Robey, R.W., Steadman, K., Polgar, O., Bates, S.E., 2005. ABCG2-mediated transport of photosensitizers. Cancer Biol. Ther. 4, 187–194. https://doi.org/10.4161/cbt.4.2.1440.

Robey, R.W., Steadman, K., Polgar, O., Morisaki, K., Blayney, M., Mistry, P., Bates, S.E., 2004. Pheophorbide a is a specific probe for ABCG2 function and inhibition. Cancer Res 64, 1242–1246. https://doi.org/10.1158/0008-5472.CAN-03-3298.

Ross, D.D., Yang, W., Abruzzo, L.V., Dalton, W.S., Schneider, E., Lage, H., Dietel, M., Greenberger, L., Cole, S.P.C., Doyle, L.A., 1999. Atypical Multidrug Resistance: Breast Cancer Resistance Protein Messenger RNA Expression in Mitoxantrone-Selected Cell Lines. J. Natl. Cancer Inst. 91, 429–433. https://doi.org/10.1093/jnci/91.5.429.

Szczygieł, M., Boroń, B., Szczygieł, D., Szafraniec, M., Susz, A., Matuszak, Z., Urbańska, K., Fiedor, L., 2014. Real-time non-invasive transdermal monitoring of photosensitizer level in vivo for pharmacokinetic studies and optimization of photodynamic therapy protocol. J. Anal. Bioanal. Tech. 5 https://doi.org/10.4172/2155-9872.1000227.

Szczygieł, M., Urbańska, K., Jurecka, P., Stawoska, I., Stochel, G., Fiedor, L., 2008. Central metal determines pharmacokinetics of chlorophyll-derived xenobiotics. J. Med. Chem. 51, 4412–4418. https://doi.org/10.1021/jm7016368.

Takaaki, F., Tokuda, S., Nakazawa, Y., Kurozumi, S., Obayashi, S., Yajima, R., Shirabe, K., 2020. Implications of low serum albumin as a prognostic factor of long-term outcomes in patients with breast cancer. In Vivo 34, 2033–2036. https://doi.org/10.21873/invivo.12003.

Tang, P.M.K., Chan, J.Y.W., Au, S.W.N., Kong, S.K., Tsui, S.K.W., Waye, M.M.Y., Mak, T.C.W., Fong, W.P., Fung, K.P., 2006. Pheophorbide a, an active compound isolated from Scutellaria barbata, possesses photodynamic activities by inducing apoptosis in human hepatocellular carcinoma. Cancer Biol. Ther. 5, 1111–1116. https://doi.org/10.4161/cbt.5.9.2950.

Tuhl, A., Makhseed, S., Zimcik, P., Al-Awadi, N., Novakova, V., Samuel, J., 2012. Heavy metal effects on physicochemical properties of non-aggregated azaphthalocyanine derivatives. J. Porphyr. Phthalocyanines 16, 817–825. https://doi.org/10.1142/S1088424612500800.

Uchoa, A.F., Konopko, A.M., Baptista, M.S., 2015. Chlorophyllin derivatives as photosensitizers: Synthesis and photodynamic properties. J. Braz. Chem. Soc. 26, 2615–2622. https://doi.org/10.5935/0103-5053.20150290.

Villalobos, M., Olea, N., Brotons, J.A., Olea-Serrano, M.F., Ruiz de Almodovar, J.M., Pedraza, V., 1995. The E-screen assay: A comparison of different MCF7 cell stocks. Environ. Health Perspect. 103, 844–850. https://doi.org/10.1289/ehp.95103844.

Welter, M., Rieger, H., 2013. Interstitial fluid flow and drug delivery in vascularized tumors: a computational model. PLoS One 8, 1–23. https://doi.org/10.1371/journal.pone.0070395.

Wiese, T.E., Kral, L.G., Dennis, K.E., Butler, W.B., Brooks, S.C., 1992. Optimization of estrogen growth response in MCF-7 cells. Vitr. Cell. Dev. Biol. 28A, 595–602. https://doi.org/10.1007/BF02631033.

Wu, C.P., Shukla, S., Calcagno, A.M., Hall, M.D., Gottesman, M.M., Ambudkar, S.V., 2007. Evidence for dual mode of action of a thiosemicarbazone, NSC73306: A potent

substrate of the multidrug resistance-linked ABCG2 transporter. Mol. Cancer Ther. 6, 3287–3296. https://doi.org/10.1158/1535-7163.MCT-07-2005.

Ye, Y., Chen, X., Guo, Y., 2013. Research on the interaction between pheophorbide and bovine serum albumin. Adv. Mater. Res. 749, 471–476. https://doi.org/10.4028/www.scientific.net/AMR.749.471.

Zemlin, A.E., Burgess, L.J., Engelbrecht, A., 2009. Two cases of severe hypoalbuminemia (< 10 g /L). Nutrition 25, 1006–1010. https://doi.org/10.1016/j.nut.2008.12.017.
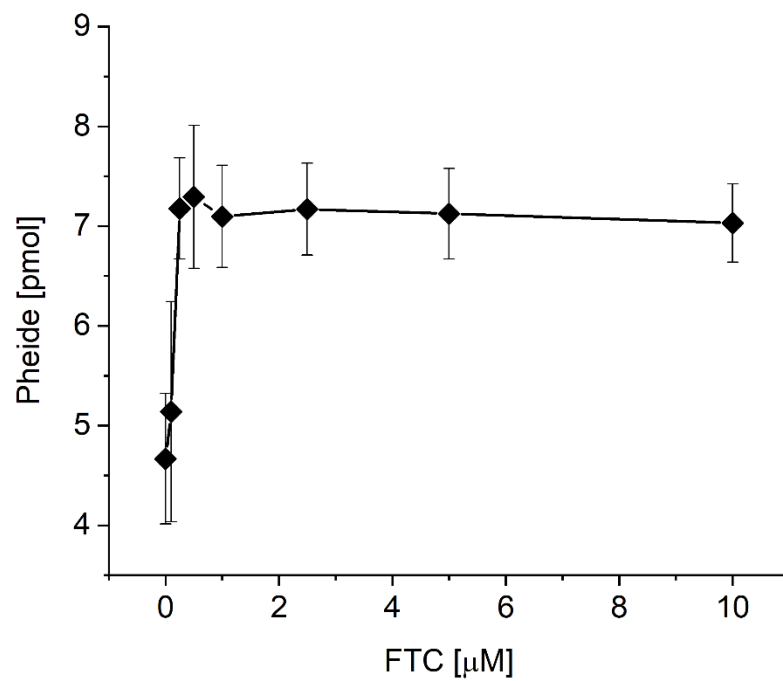
Figure S1. Optimization of FTC concentration used in the uptake and efflux studies. The MCF-7/ABCG2 cells were incubated in serum-free medium with various concentrations of FTC, for 3 hours. Then, Pheide concentration was determined in cell lysates by fluorescence measurement.
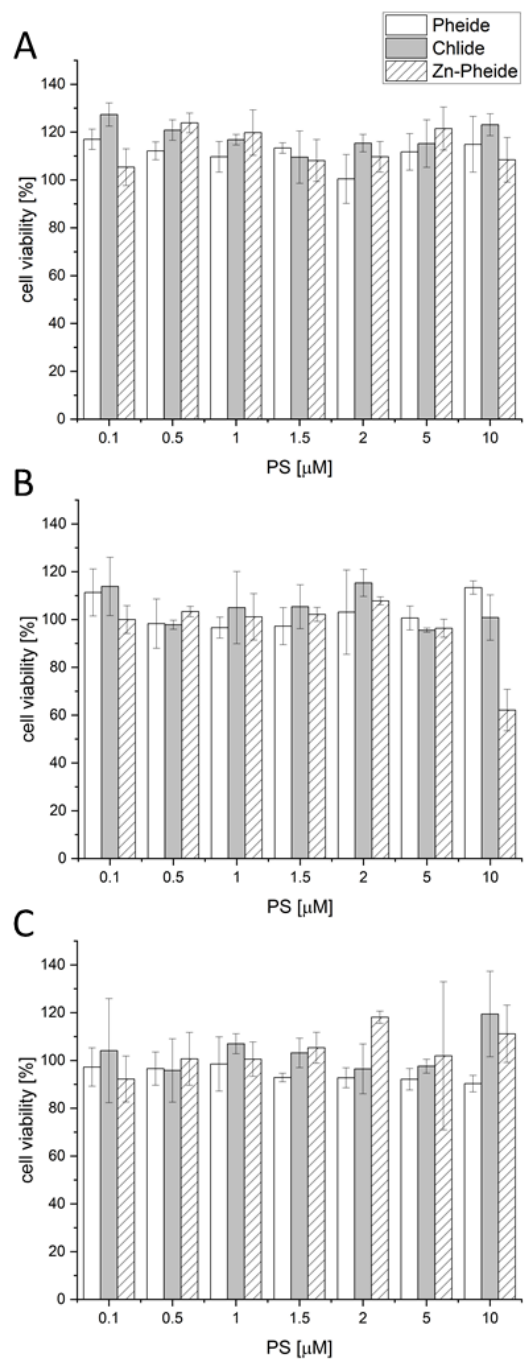
Figure S2. Dark cytotoxicity of the PSs towards MCF-7 cells after 3 h (**A**) and 24 h (**B**) of incubation in the absence of serum and after 24 h of incubation in the presence of 10% FBS (**C**). The results are presented as means ± SD for n = 3.

Calculation of the apparent dissociation constants of the PSs to BSA

For calculation of the K_{app} of Chlide and Zn-Pheide to BSA, we assumed that the fluorescence of a PS measured at a given concentration of BSA is given as:

$$F = F_b \cdot B + F_f \cdot (T - B), \tag{1}$$

where F is the experimentally determined fluorescence at a given concentration of BSA, F_b is the specific molar fluorescence intensity of bound PS, B is the concentration of bound PS, F_f is the specific molar fluorescence intensity of free PS, and T is the total PS concentration (equal to1 µM in the present study).

The equation (1) can be written as:

$$F = F_b \cdot B + F_f \cdot T - F_f \cdot B, \tag{2}$$

or when we substitute $F_0 = F_f \cdot T$ as a PS fluorescence in the absence of BSA:

$$F = F_b \cdot B + F_0 - \frac{F_0}{T} \cdot B \tag{3}$$

We checked that up to 1 µM of the PSs, their fluorescence signals are linearly dependent on the concentration, therefore F_f has a constant value, which can be easily determined from an appropriate calibration curve.

Thus:

$$\frac{F}{F_0} = \frac{F_b}{F_0} \cdot B + 1 - \frac{1}{T} \cdot B \tag{4}$$

And rearranging yields:

$$\frac{F}{F_0} - 1 = \left(\frac{F_b}{F_0} - \frac{1}{T} \right) \cdot B \tag{5}$$

Therefore:

$$B = \frac{\dfrac{F}{F_0} - 1}{\dfrac{F_b}{F_0} - \dfrac{1}{T}} \tag{6}$$

At sufficiently high BSA concentrations a saturation of the fluorescence signal was observed. As upon saturation all the ligand is bound ($B = T$), the maximal obtained fluorescence signal, F_{max}, is equal to:

3

$$F_{max} = F_b \cdot T \, , \tag{7}$$

therefore:

$$F_b = \frac{F_{max}}{T} \, , \tag{8}$$

and:

$$B = \frac{\dfrac{F}{F_0} - 1}{\dfrac{F_{max}}{F_0 \cdot T} - \dfrac{1}{T}} \tag{9}$$

or:

$$B = \frac{\left(\dfrac{F}{F_0} - 1\right) \cdot T}{\dfrac{F_{max}}{F_0} - 1} \tag{10}$$

And the fluorescence of bound ligand fraction, *F(B),* equals to:

$$F(B) = \frac{\left(\dfrac{F}{F_0} - 1\right) \cdot T}{\dfrac{F_{max}}{F_0} - 1} \cdot F_{max} \tag{11}$$

The calculated $F(B)$ values were plotted against the corresponding BSA concentrations and fitted with rectangular hyperbolas, according to the equation:

$$y = \frac{B_{max} \cdot x}{K_{app} + x} \, , \tag{12}$$

from where the values of K_{app} were read.

4

Table S1. Statistical significance of differences in the levels of the PSs after particular efflux periods between MCF-7/mock and MCF-7/ABCG2 sublines (column A) and between inhibited and uninhibited MCF-7/ABCG2 cells (column B). Analysis performed by the two-sample Student's t-test in Origin 2021. Asterisks represent significant differences ($p < 0.05$).

time [h]	Pheide		Chlide		Zn-Pheide	
	A	B	A	B	A	B
0	*	*	*	*	*	*
0.25		*	*	*		*
0.5		*	*	*	*	*
1		*	*	*	*	*
2		*	*	*	*	*
3		*	*	*	*	*
4		*	*	*		
5		*	*	*	*	*
6				*	*	*
12		*	*	*	*	*
16	*	*	*	*	*	*
20		*	*	*	*	*
24		*	*	*	*	*

Table S2. Statistical significance of differences in the viability of MCF-7/mock and MCF-7/ABCG2 cells (column A) and inhibited and uninhibited MCF-7/ABCG2 cells (column B) recorded after particular efflux periods in serum-containing medium. Analysis performed by the two-sample Student's t-test in Origin 2021. Asterisks represent significant differences ($p < 0.05$).

time [h]	Pheide A	Pheide B	Chlide A	Chlide B	Zn-Pheide A	Zn-Pheide B
0	*	*	*			
0.25	*	*	*	*	*	*
0.5	*	*	*	*	*	*
1	*		*	*	*	*
2			*	*	*	*
3			*	*		*
4				*		*
5				*		*
6				*		*
12				*		
16						
20						
24						

Table S3. Statistical significance of differences in the viability of MCF-7/mock and MCF-7/ABCG2 cells (column A) and inhibited and uninhibited MCF-7/ABCG2 cells (column B) recorded after particular efflux periods in serum-free medium. Analysis performed by the two-sample Student's t-test in Origin 2021. Asterisks represent significant differences ($p < 0.05$).

time [h]	Pheide A	Pheide B	Chlide A	Chlide B	Zn-Pheide A	Zn-Pheide B
0	*	*				
0.25	*	*				
0.5	*	*				
1	*	*				
2	*	*				
3	*	*	*	*		
4	*	*	*	*		
5	*	*	*	*		
6	*	*	*	*		
12		*	*	*	*	*
16		*		*	*	*
20		*		*	*	*
24		*	*	*	*	*

Interactions of chlorophyll-derived photosensitizers with human serum albumin are determined by the central metal ion

Milena J. Szafraniec

View supplementary material

Published online: 29 Nov 2021.

Submit your article to this journal

View related articles

View Crossmark data

Taylor & Francis
Taylor & Francis Group

Check for updates

Interactions of chlorophyll-derived photosensitizers with human serum albumin are determined by the central metal ion

Milena J. Szafraniec

Łukasiewicz Research Network – PORT Polish Center for Technology Development, Wrocław, Poland

Communicated by Ramaswamy H. Sarma

ABSTRACT

Two structurally similar derivatives of chlorophyll a, chlorophyllide a (Chlide) and zinc-pheophorbide a (Zn-Pheide), differing only in central metal ion (Mg^{2+} or Zn^{2+}, respectively) substituting the tetrapyrrole ring, were investigated with regard to their binding to human serum albumin (HSA). Chlide and Zn-Pheide are very promising photosensitizers with potential application in photodynamic therapy, therefore it is desirable to investigate their interactions with serum proteins. The studies included absorption and steady-state fluorescence spectroscopy, as well as molecular docking. It was found that both investigated compounds form complexes with HSA. Experimental data revealed two classes of binding sites for each compound. The affinities (K_a) for the first class were in the range of 10^5 and 10^6 M^{-1} for Chlide and Zn-Pheide, respectively, while the second class was characterized by the affinities of the order of 10^4 M^{-1} for both derivatives. Molecular docking simulations together with displacement studies revealed that the primary binding site of the studied compounds is the heme site, localized in the subdomain IB, however the best characterized binding sites of HSA, namely the Sudlow's sites I and II are also involved. The interactions between the derivatives of chlorophyll and HSA were found to be predominantly hydrophobic and to a lesser extent hydrogen bonding. Our results demonstrate that the centrally bound metal ion determines both the affinity and mode of binding to HSA, which may be a feature differentiating these compounds in terms of their pharmacokinetics.

Introduction

Chlorophyllide a (Chlide) and zinc-pheophorbide a (Zn-Pheide) are semi-synthetic derivatives of chlorophyll a with potential application in photodynamic therapy. They possess several features of ideal photosensitizers (PSs), including strong light absorption in the part of visible spectrum, coinciding with the therapeutic window of human tissue, and a high efficiency of reactive oxygen species generation. Both, in vitro and in vivo studies have demonstrated a high photodynamic potential of Chlide and Zn-Pheide, making them good candidates for clinical use (Jakubowska et al., 2013; Szczygieł et al., 2014). Since the application of the PSs involves their direct administration into the bloodstream, the first issue to be taken into account when analyzing their pharmacokinetics is the interaction with the components of circulating blood. This involves binding to proteins, lipids and lipoproteins as well as to cell membranes of erythrocytes and leukocytes. Chlide and Zn-Pheide are relatively well water-soluble molecules, therefore they are expected to be transported by albumins and globulins rather than by lipoproteins and cell membranes (Mazière et al., 1991). And since albumin constitutes a bulk of serum proteins, it is predicted to be the main binder of the PSs, acting right after their application. In our previous studies, we observed a significant difference between Chlide and Zn-Pheide regarding their binding to bovine serum albumin (Szafraniec & Fiedor, 2021). This prompted us to thoroughly investigate the interaction of these compounds with HSA, which is of crucial importance from the point of view of their potential application as intravenously administered drugs. Binding to HSA is likely to significantly affect the pharmacokinetics and pharmacodynamics of the PSs and, as a consequence, an ultimate photodynamic effect resulting from their application. It can also attenuate the undesirable effect of dark cytotoxicity, which can occur at high doses of the PSs, and regulate the bioavailability of other drugs present in the organism simultaneously with the PSs.

Human serum albumin consists of a single chain with three structurally similar domains (I, II and III), each containing two subdomains, A and B (Carter et al., 1989). The subdomains IIA and IIIA are recognized as the principal sites of ligand binding (Sudlow et al., 1975; Sudlow et al., 1976; Kragh-Hansen et al., 2002). HSA is equipped with one Trp residue (Trp214), located in subdomain IIA, which, being its dominant intrinsic fluorophore, is often used in the association studies of HSA with endo- and exogenous ligands by fluorescence spectroscopy techniques (Lakowicz, 2006; Roufegarinejad et al., 2019). In the present study,

spectroscopic analyses on the binding of chlorophyll-derived PSs to HSA were performed together with molecular docking studies in order to determine their binding affinities and binding sites. Absorption as well as fluorescence enhancement and quenching studies revealed the formation of complexes between the PSs and HSA. Additionally, fluorescence quenching and displacement studies showed the existence of at least two binding sites for the investigated compounds, which was further confirmed by molecular docking. The obtained comprehensive data were applied to explain the binding mechanism between chlorophyll derivatives and HSA, which may contribute to a better understanding of their transportation, distribution and metabolism and as a consequence their efficacy as PSs applied in vivo.

Materials

Human serum albumin (fatty acid free) was obtained from PAN-Biotech (Aidenbach, Germany). The protein was dissolved daily in PBS (10 mM phosphate, 140 mM NaCl, 2.68 mM KCl, pH 7.4). Chlorophyllide a was kindly provided by Prof. Leszek Fiedor and Dr. Małgorzata Szczygieł (Faculty of Biochemistry, Biophysics and Biotechnology, Jagiellonian University, Kraków, Poland). Zn-Pheide was obtained from pheophorbide a (Cayman Chemical, Ann Arbor, MI, USA) by direct metalation with zinc acetate, as described previously (Szczygieł et al., 2008). The purity of both compounds determined by HPLC analysis was at least 96%. The concentrations of the PSs were determined spectrophotometrically in their ethanol solutions, using the extinction coefficient at the Q_y band 71,500 M^{-1}cm^{-1}. For each experiment, fresh solutions of the PSs were prepared by their suspension in appropriate volumes of DMSO. The structure of the PSs is shown in Figure 1.

Methods

Absorption measurements

Absorption spectra in the ultraviolet-visible region (UV-Vis) were obtained using an Evolution 201 spectrophotometer (Thermo Scientific, Waltham, MA, USA) equipped with xenon flash lamp. The spectra were recorded in the range $230 - 800$ nm at room temperature, using a 1 cm pathlength quartz cuvette. The concentrations of HSA and PSs were 50 and 25 μM, respectively. The spectra were recorded for the protein and ligands separately, as well as for their complexes. The measurements were carried out in PBS (pH 7.4) at three concentrations of DMSO: 1%, 5% and 15%. In each measurement, the reference sample was the dissolution medium: PBS with appropriate concentration of DMSO.

Fluorescence measurements

Steady-state fluorescence spectra were recorded using a Jasco FP-8500 spectrofluorometer (Jasco, Pfungstadt, Germany) equipped with a 150 W xenon lamp. The measurements were performed in a Hellma fluorescence cuvette with 100 μL chamber volume. Each sample was incubated for 10 minutes at

desired temperature to reach equilibrium before the measurement. The temperature was controlled using an ETC-815 water-cooled Peltier thermostatic cell holder (Jasco). In all measurements, the excitation and emission slits were set to 5 and 10 nm, respectively. Each spectrum was measured twice, using a fresh aliquot of the same sample, in order to avoid a potential photodamage of HSA resulting from a PS excitation. Two types of fluorometric experiments were performed:

a. Fluorescence enhancement of 1 μM PSs at increasing concentrations of HSA (0, 0.125, 0.25, 05, 1, 2, 5, 10, 25, 50, 100, 250 and 500 μM), with excitation at 430 nm and emission collection between 600 and 800 nm, at 310 K. In these experiments the samples were prepared in PBS, pH 7.4 containing 1% DMSO.
b. HSA (1 μM) fluorescence quenching after excitation at two different wavelengths, 280 nm (for Trp, Tyr and Phe residues) and 295 (for Trp only), and emission collection between 305 and 500 nm or 320 and 500 nm for these two excitation wavelengths, respectively. The PSs were added to HSA at concentrations of 0, 0.5, 1, 2.5, 5, 10, 25, 50 and 100 μM and the measurements were performed at two temperatures, 298 and 310 K. The final concentration of DMSO was 5%. The recorded fluorescence intensities were corrected for the inner filter effect, according to the equation:
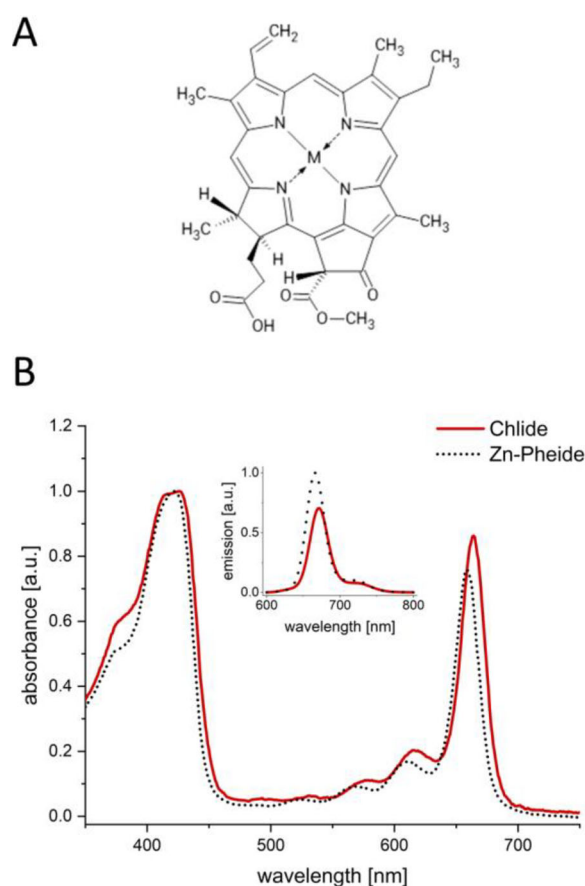

Figure 1. (A) General structure of the investigated compounds. M = Mg for Chlide and Zn for Zn-Pheide. (B) Normalized absorption and emission (inset) spectra of Chlide and Zn-Pheide recorded in ethanol. The emission spectra were measured after excitation in the Soret band.

$$F_{corr} = F_{obs} \times e^{(A_{ex}+A_{em})/2} \qquad (1)$$

where F_{corr} is the corrected fluorescence intensity, F_{obs} is the measured fluorescence intensity, and A_{ex} and A_{em} are the absorbances of the measured solutions at the excitation and emission wavelengths, respectively (Lakowicz, 2006). For the calculation of dissociation constants, the fluorescence maxima corresponding to the bound fractions of the PSs recorded in the PSs fluorescence enhancement study were plotted against HSA concentration and fitted with two-site binding curve (birectangular hyperbola) in the Origin 2021 (Origin, Version, 2021).

Synchronous fluorescence measurements

Synchronous fluorescence spectra of HSA in the presence or absence of the PSs were collected using a FS5 spectrofluorometer (Edinburgh Instruments Ltd., Livingston, UK) equipped with a 150 W xenon lamp. The excitation and emission slits were set at 3 nm. The interval between the excitation end emission wavelength was set at 15 or 60 nm to observe the spectral behavior of Tyr and Trp residues, respectively. The measurements were performed in 1 cm quartz cell in PBS pH 7.4, at 310 K, maintained by a SC-20 water bath regulated thermostatic sample holder (Edinburgh Instruments Ltd.). In each assay, HSA (1 μM) was titrated with a PS at concentrations of 5, 10, 25 and 50 μM. The obtained fluorescence spectra were corrected for the inner filter effect using the Equation (1).

Displacement studies

Competitive binding studies were performed using three different site probes: hemin, warfarin and ibuprofen (all from Pol-Aura, Poland) for sites IB, IIA and IIIA, respectively. The concentrations of HSA (100 μM) and PS (1 μM) were kept constant and various concentrations of the site probes (0.5, 1, 2, 5 and 10 μM) were added to the system. After every addition of a probe, the sample was incubated for 10 min at 310 K to reach equilibrium. Fluorescence measurements were carried out using a FS5 spectrofluorometer (Edinburgh Instruments Ltd.) using 430 nm excitation wavelength and $600 - 800$ nm emission range. The excitation and emission slit widths were set at 2 nm. The measurements were performed in PBS pH 7.4, at 310 K.

Molecular docking

The three-dimensional coordinates of HSA (PDB ID: 1AO6) were downloaded from the RSCB Protein Data Bank. Only the monomer chain A was retained and solvent molecules were deleted. ChemSketch 2020.1.2 software was used to draw the structures and pre-optimize them in 3 dimensions (ACD/ChemSketch, version 2.1, 2020). Further 3D structure optimization, as well as the calculation of partial (Mulliken) charges were performed in the ORCA 4.2 software using the
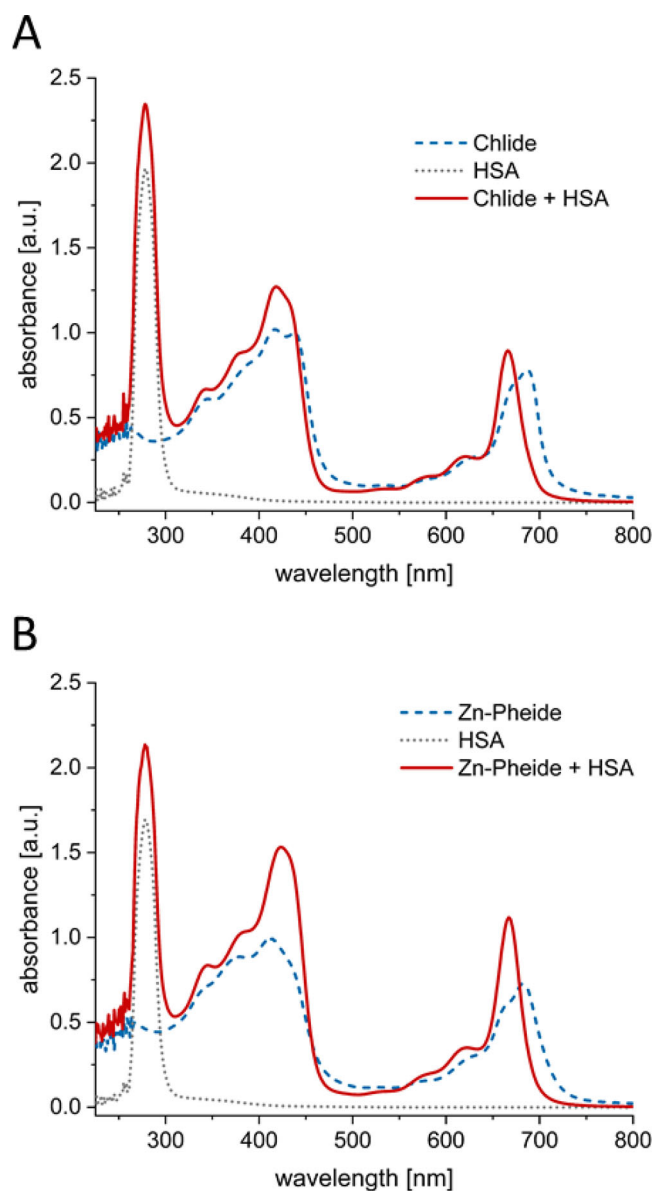

Figure 2. Absorption spectra of 25 μM Chlide (A) and Zn-Pheide (B) in PBS pH 7.4 containing 1% DMSO matched with the corresponding spectra with the addition of 50 μM HSA and the spectrum of sole HSA. The spectra were normalized to obtain the absorption of free PS equal to 1 in the Soret band.

BP86 functional with ZORA relativistic approximation and def2-SVP SARC/J basis set (Neese et al., 2020). The calculated charges were manually introduced into the pdbqt files. For each PS, eight active torsions in the side chains were included, and the tetrapyrrole ring was considered rigid. The protonation state corresponding to pH of 7.4 was set for HSA using OpenBabel 3.0.0 and Kollman charges were added to it in the AutoDock 4.2 (Morris et al., 2009; O'Boyle et al., 2011). A grid box covering the amino acid residues specific either to Sudlow's I, Sudlow's II or heme site was generated using the AutoGrid 4. Docking simulations were carried out in the AutoDock 4.2 using the Lamarckian Genetic Algorithm with at least 100 iterations for every binding site. Other AutoDock parameters were used with default values. Visualization of docking results was performed in the PyMOL
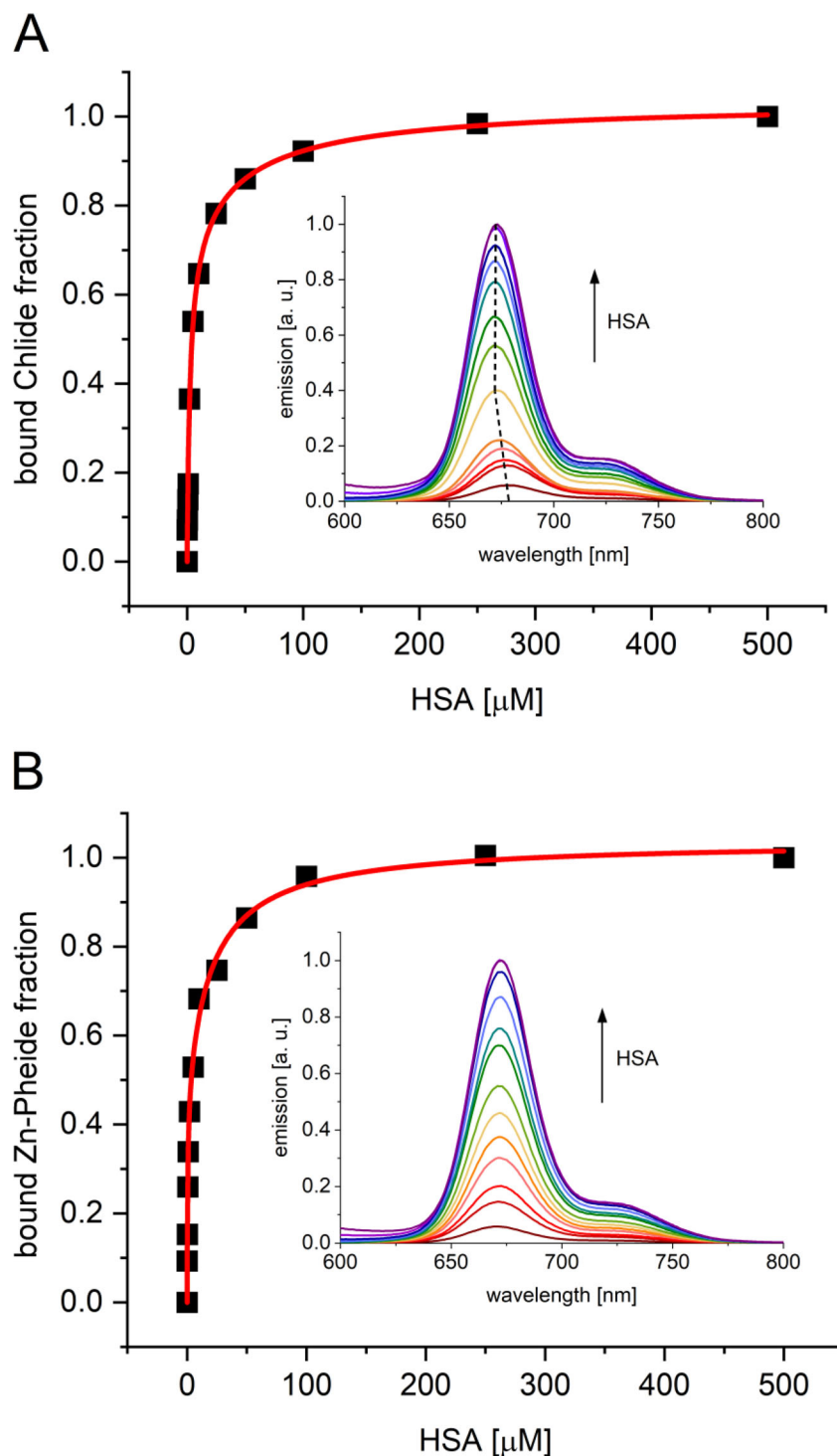
Figure 3. Fluorescence enhancement of Chlide (A) and Zn-Pheide (B) in the presence of HSA. The experimental points of the binding curves correspond to the fluorescence maxima of the bound PS fraction. The spectra originating from total (free + bound) PS fluorescence are shown in the insets. Solid lines are curve-fitting results assuming 2:1 (PS: HSA) binding.

and BIOVIA Discovery Studio Visualizer using the conformations with the lowest binding free energy (BIOVIA, 2021; Schrödinger, LLC., 2010). The association constants (K_a) for protein−ligand interactions were calculated from the obtained free energy change (ΔG) of docking using the equation:

$$\Delta G = -RT\ln K_a \qquad (2)$$

Table 1. Summary of the dissociation constants (K_d) determined on the basis of the fluorescence enhancement experiments and the binding constants (K_a) calculated as their reciprocals.

Compound	K_d (µM)	$K_a/10^6$ (M^{-1})
Chlide	2.50 ± 0.50	0.40 ± 0.08
	50.42 ± 41.81	0.02 ± 0.02
Zn-Pheide	0.55 ± 0.12	1.82 ± 0.39
	21.15 ± 5.45	0.05 ± 0.02
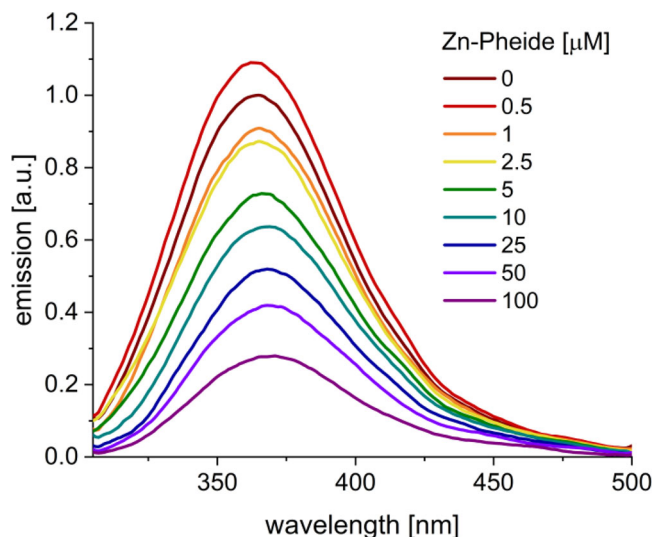
Figure 4. Representative (uncorrected) set of spectra showing HSA fluorescence quenching in the presence of Zn-Pheide. HSA (1 μM) in PBS pH 7.4 containing 5% of DMSO, $\lambda_{ex} = 280$ nm, $T = 298$ K.

where R (8.314 J mol^{-1} K^{-1}) is the gas constant and T is the absolute temperature.

Results and discussion

The absorption spectra of the PSs in the presence of HSA differed significantly from the corresponding spectra of free PSs, which indicates the formation of complexes (Figure 2). The increase in absorbance was connected with the blue shift of Q_y maxima for both Chlide and Zn-Pheide, while in the Soret band blue shift was observed for Chlide and red shift for Zn-Pheide. Importantly, the increase in absorption maxima observed after the addition of HSA was larger for Zn-Pheide than for Chlide. Thus, in the Soret band we observed the increase of 0.27 for Chlide and 0.53 for Zn-Pheide. In Q_y bands, in turn, the increase for Chlide was

Table 2. Stern–Volmer quenching constants (K_{SV}) and the quenching rate constants (k_q) of HSA fluorescence in the presence of Chlide and Zn-Pheide after the excitation at 295 nm.

Compound	T (K)	K_{SV1} (M^{-1})	k_{q1} (M^{-1} s^{-1})	K_{SV2} (M^{-1})	k_{q2} (M^{-1} s^{-1})
Chlide	298	23,809	2.381×10^{12}	13,122	1.312×10^{12}
	310	27,753	2.775×10^{12}	9,119	0.912×10^{12}
Zn-Pheide	298	48,931	4.893×10^{12}	16,836	1.684×10^{12}
	310	40,648	4.065×10^{12}	13,621	1.362×10^{12}
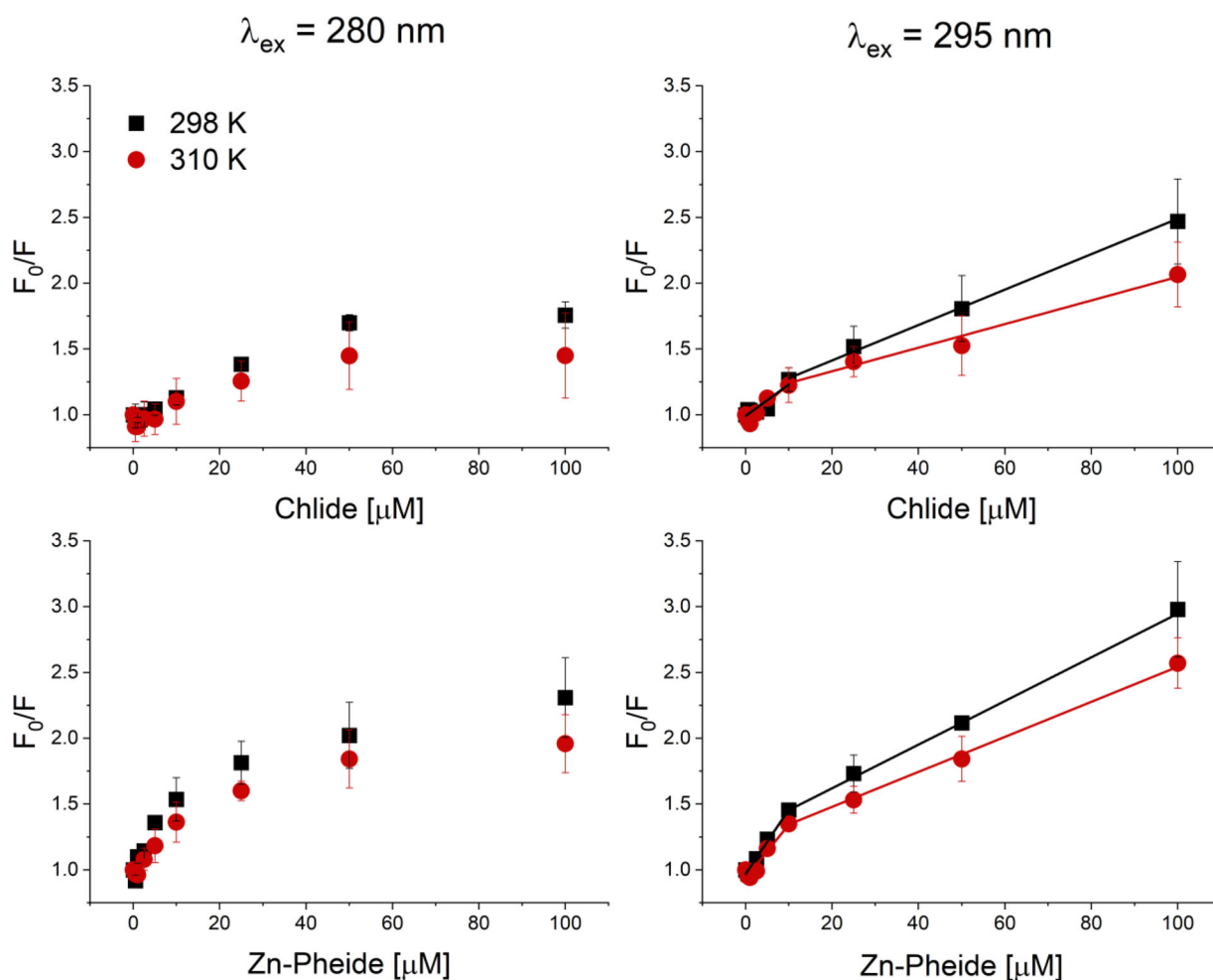
Figure 5. Stern-Volmer plots of HSA fluorescence quenching by Chlide and Zn-Pheide at 298 (black squares) and 310 K (red dots). HSA concentration was 1 μM in all experiments. The straight lines represent fitted curves. The left panel corresponds to the quenching observed after HSA excitation at 280 nm, and the right panel after excitation at 295 nm.
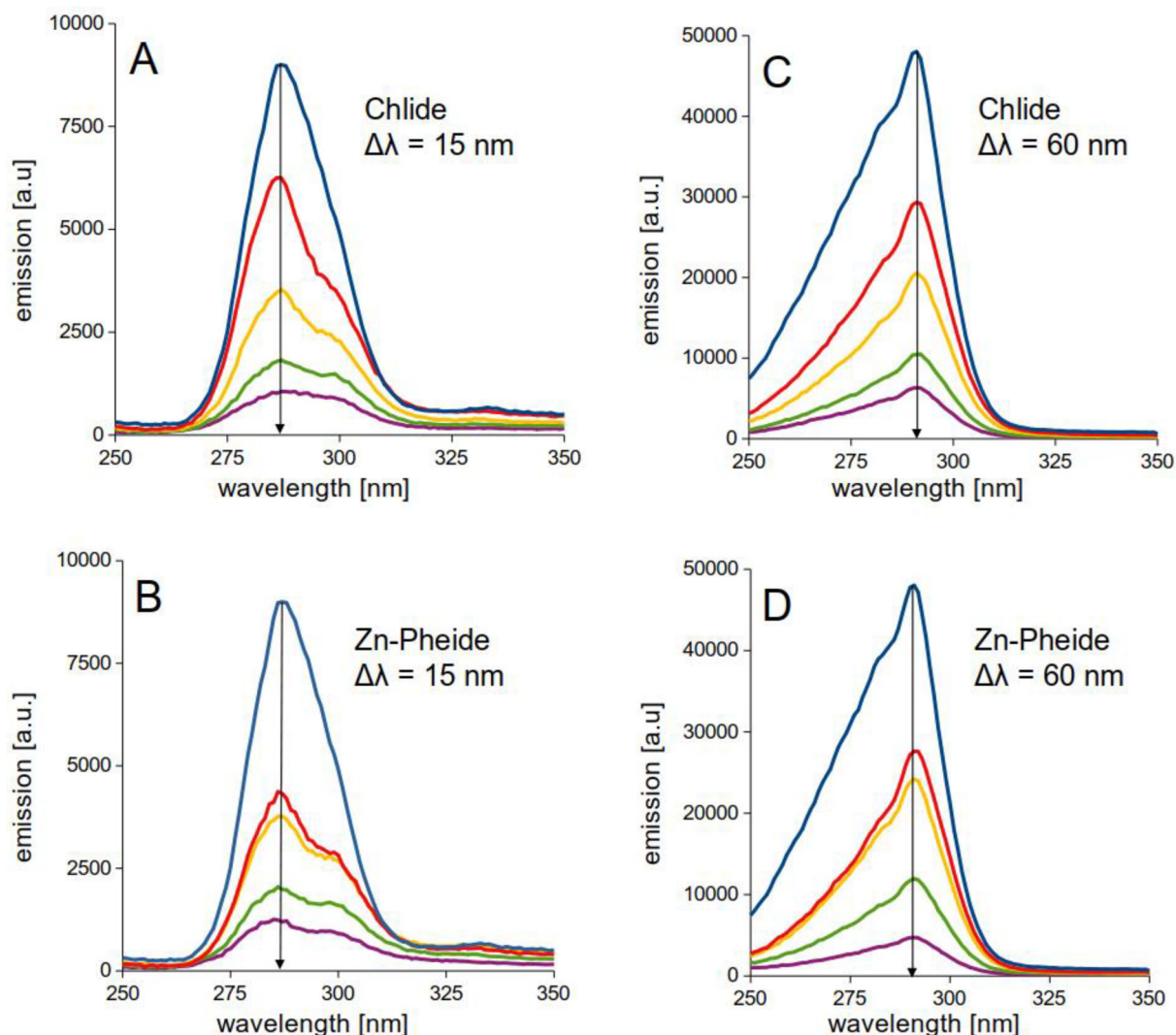
Figure 6. Synchronous fluorescence spectra of HSA (1 μM) in the presence of Chlide (A and C) and Zn-Pheide (B and D) measured at emission offset $\Delta\lambda = 15$ (A and B) and 60 nm (C and D), at pH 7.4 and 310 K. The concentrations of the PSs were equal to 5, 10, 25 and 50 μM. The arrows indicate the increase in PS concentration.

equal to 0.12, while for Zn-Pheide 0.39. Taking into account that DMSO concentrations below 20% do not influence the structure of HSA, we measured the absorption spectra at three concentrations of DMSO: 1%, 5% and 15% (Batista et al., 2014). We observed that the absorption spectra of PS-HSA complexes measured at various DMSO concentrations were exactly the same, though the free PSs showed a progressive disaggregation with increasing DMSO concentration (data not shown). This indicates that HSA causes the maximal possible disaggregation of the PSs already at 1% of DMSO, and further increase in DMSO concentration is not necessary to increase the efficiency of binding. The subsequent fluorescence enhancement studies were therefore performed at 1% DMSO.

The fluorescence of both Chlide and Zn-Pheide was found to substantially increase with increasing concentration of HSA, which can be explained by the fact that HSA acted as a solubilizer for PSs aggregates, as these compounds, though relatively hydrophilic, are not completely soluble in aqueous media (Figure 3, insets). In the case of Chlide, apart from the increase in fluorescence signal, about 6 nm blue shift of

fluorescence maximum was observed (Figure 3(A), inset). This effect is most likely due to the loss of axially coordinated water molecules and a consequent change in the conformation of the tetrapyrrole ring (Bonnett, 2003; Fiedor et al., 2008; Szczygieł et al., 2008). No spectral shift was observed for Zn-Pheide (Figure 3(B), inset), probably due to stronger chelation of Zn^{2+}, ion and different coordination properties (Hartwich et al., 1998; Szczygieł et al., 2008).

Since both PSs show a significant fluorescence in aqueous media even in their unbound state, to calculate their dissociation constants, the signal from their albumin-bound fraction had to be separated from that of free PS fraction. We therefore performed a correction of the obtained fluorescence signal which is fully described in Supplementary materials. To obtain the binding curves, the calculated bound PS fraction was plotted against corresponding HSA concentration (Figure 3). We observed that the obtained binding curves are much better fitted with two-binding site model than with a single binding site model ($R^2 = 0.95$ vs. 0.99, respectively). Further increasing the number of binding sites did not improve the fit, but increased the inaccuracy of the
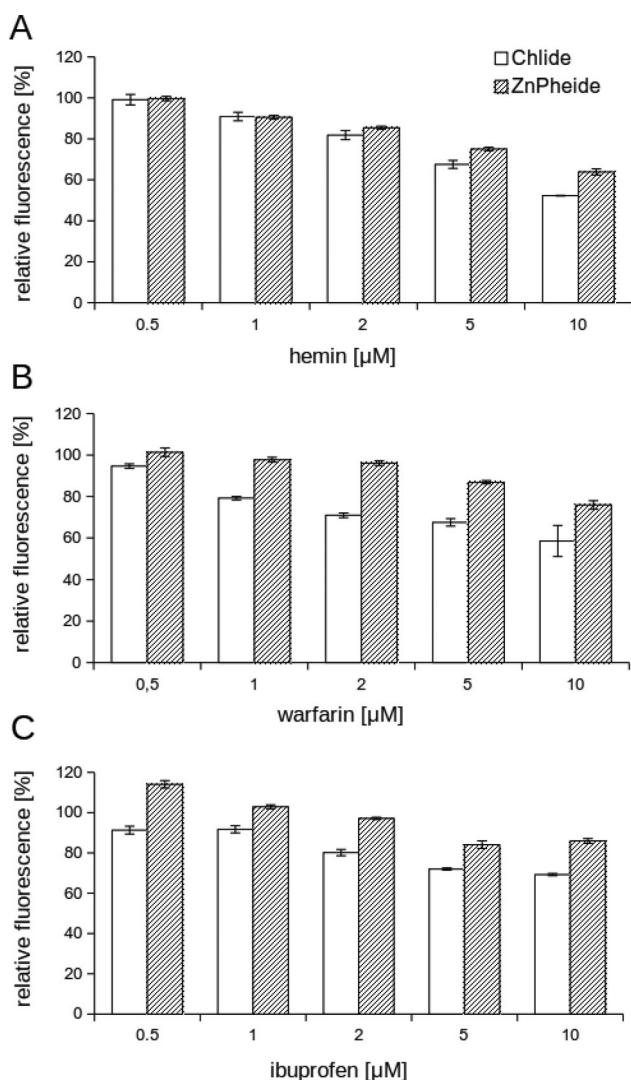
Figure 7. Relative fluorescence intensities at 670 nm (compared to the controls measured without the site markers) of 1 μM PSs in the presence of 100 μM HSA and various concentrations of hemin (A), warfarin (B) and ibuprofen (C). The results are presented as means ± SD from three measurements.

determined coefficients. The dissociation constants determined on the basis of the fluorescence enhancement study are presented in Table 1.

To further investigate the interactions between HSA and the PSs, we measured the intrinsic HSA fluorescence before and after the addition of the ligands at variable concentrations. In HSA there are three types of fluorescent residues: tryptophan (Trp), phenylalanine (Phe) and tyrosine (Tyr), of which the strongest signal is obtained from Trp, due to its higher molar absorptivity and intrinsic fluorescence quantum yield (Jahanban-Esfahlan et al., 2017, 2021). The contribution of Phe residues to the intrinsic fluorescence of protein is negligible by virtue of its low absorptivity and a very low quantum yield (Lakowicz, 2006; Roufegarinejad et al., 2019). In the structure of HSA, there is only one Trp residue (Trp214), localized in its subdomain IIA, while Tyr residues are dispersed within all three domains (Hosainzadeh et al., 2012). In order to determine the participation of Trp214 and other fluorescent residues in the formation of the PS–HSA complexes, we performed the quenching experiments using

two excitation wavelengths, $\lambda_{ex} = 280$ nm for all fluorescent residues and $\lambda_{ex} = 295$ nm for Trp only. The maximum of free HSA fluorescence, irrespectively of the excitation wavelength, was recorded at 363 or 364 nm. At very low concentrations of the PSs (up to 0.5 μM) we observed a slight increase in HSA fluorescence signal and the quenching started from 1 μM of the PSs (Figure 4). This biphasic effect is probably due to aggregation of HSA in the presence of DMSO and its disaggregation upon binding of ligands.

The quenching of HSA fluorescence can result from the transfer of energy between its fluorescent residues and the chromophores present in the PSs molecules. Such a transfer is possible when the distance between the donor and acceptor does not exceed 10 nm, which can result from complex formation (Ghisaidoobe & Chung, 2014). The quenching mechanism between the PSs and HSA can be described by the Stern-Volmer equation:

$$\frac{F_0}{F} = 1 + K_{SV} \cdot [Q] \tag{3}$$

where F and F_0 are the fluorescence emission intensities in the presence and absence of the quencher, respectively, K_{SV} is the Stern–Volmer constant and $[Q]$ is the concentration of quencher (Lakowicz, 2006). The Stern–Volmer quenching constant K_{SV} is given by $K_{SV} = k_q \times \tau_0$, where k_q is the bimolecular quenching constant (or the efficiency of quenching), and τ_0 is the lifetime of the fluorophore in the absence of quencher. The value of τ_0 for biopolymers is reported to be 10^{-8} s (Cui et al., 2009). The quenching described by the Stern-Volmer equation may be both static and dynamic. It is considered that the threshold value of k_q below which the quenching is predominantly diffusion-controlled equals to 2×10^{10} M^{-1} s^{-1} (Ge et al., 2010).

For the measurements of quenching performed after the excitation at 280 nm, we obtained non-linear, downward facing Stern-Volmer plots in the case of both PSs (Figure 5, left panel). This shape is characteristic for fractional accessibility of fluorophores to a quencher (Lakowicz, 2006). Corresponding plots obtained after the excitation at 295 nm were linear but biphasic, which shows that two binding classes of binding sites are responsible for the quenching (Figure 5, right panel). These results show that a part of Tyr residues present in HSA is not accessible to the PSs. The Trp214 residue, in turn, is quenched by the ligands bound to two classes of binding sites. Possibly, these are Sudlow's site I and the heme site as they are closest to the Trp214 residue (Kamal & Behere, 2005; Sudlow et al.,1975). In each case, the quenching decreased with increasing temperature, which ensures the static type of quenching, resulting from complex formation (Figure 5).

The Stern–Volmer constants for the quenching of HSA after the excitation at 295 nm were determined as the slopes of the curves fitted to the Stern–Volmer plots (Figure 5, right panel). The obtained values of K_{SV} and corresponding k_q are summarized in Table 2.

Since all calculated k_q values are of the order of 10^{12} M^{-1} s^{-1}, and, additionally, their decrease with increasing temperature is observed, we suggest that in the investigated systems the quenching of Trp214 was not primarily
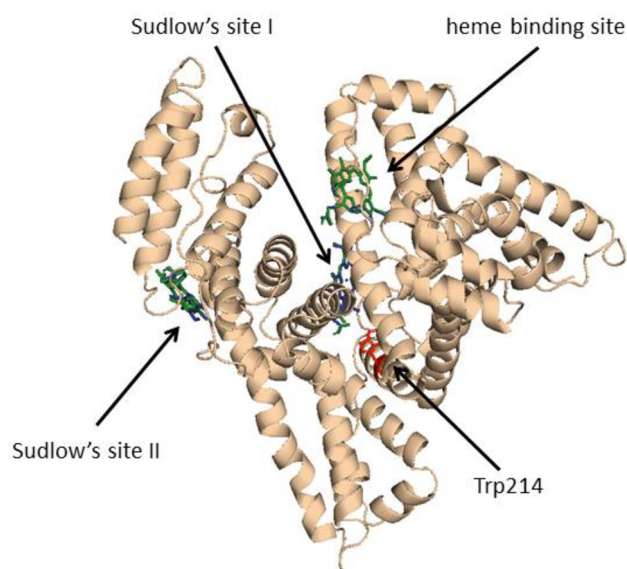
Figure 8. Superimposition of the best score docking poses in the HSA structure obtained for Chlide (green) and Zn-Pheide (blue) by molecular docking (the structures are to a large extent overlapping). The Trp214 residue is marked in red. Figure generated with the PyMOL software.

caused by dynamic collision, but resulted from the formation of non-fluorescent ground-state complexes (Ouameur et al., 2005). The quenching was in each case weaker for Chlide than for Zn-Pheide, which suggests the stronger binding of the latter. However, we did not use the fluorescence quenching data to determine the exact binding constants, because due to the fluorescence enhancement at low concentrations of the PSs, these results could be inaccurate.

To investigate the conformational changes of HSA induced by the PSs, we performed synchronous fluorescence measurements. Synchronous fluorescence spectroscopy is a useful method enabling the characteristics of polarity changes in the microenvironment of the chromophores (Hosainzadeh et al., 2012; Jahanban-Esfahlan et al., 2015). Synchronous spectra are collected through the simultaneous scanning of excitation and emission at a constant wavelength interval ($\Delta\lambda$), which equals to 15 nm for Tyr and 60 nm for Trp residues (Jahanban-Esfahlan et al., 2015, 2017). Figure 6 presents the impact of the PSs on the synchronous fluorescence spectra of HSA at $\Delta\lambda$ values of 15 and 60 nm. At low concentration (5 μM), Zn-Pheide quenched Tyr fluorescence visibly stronger and Trp fluorescence slightly stronger than Chlide. At higher concentrations, both PSs similarly reduced the fluorescence signal. No shift in the maximum emission wavelength was observed in the case of Trp (Figure 6(C,D)), while slight blue shift (2 nm) was observed in the emission of Tyr residues in the presence of Zn-Pheide (Figure 6(B)), indicating a decrease in polarity and increase in hydrophobicity near these chromophores (Barakat & Patra 2013; Hosainzadeh et al., 2012; Jahanban-Esfahlan et al., 2006). Interestingly, no such shift was observed for Chlide. Therefore, binding of Zn-Pheide but not Chlide leads to slight conformational changes in HSA.

As probable binding sites for the PSs, we targeted the Sudlow's sites I and II, being the major binding sites of HSA,

and the heme site, chosen due to the structural similarity between the PSs and heme. The Sudlow's sites I and II are localized in the subdomains IIA and IIIA, respectively, while the heme site is in the subdomain IB (Nicoletti et al., 2008; Sudlow et al., 1975, 1976). In order to determine the binding sites of the PSs in HSA structure and compare the affinities of Chlide and Zn-Pheide, a displacement study was performed, using site-specific markers: hemin, warfarin and ibuprofen for subdomains IB, IIA and IIIA, respectively (Ascenzi et al., 2005; Baroni et al., 2001; Poór et al., 2013). Since the fluorescence intensity strongly differs between free and bound forms the PSs (Figure 3), and, at the same time, the applied site markers do not give any fluorescent signal in the range of PS emission (600 − 800 nm), molecular displacement of the PSs from HSA can be investigated by monitoring a decrease in their emission intensity. As can be seen from Figure 7, fluorescent signals of both PSs were reduced in the presence of all the site markers, though relatively high concentrations of the markers were required to significantly decrease the emission of the PSs, particularly Zn-Pheide. The most prominent displacement was observed in the case of hemin, which indicates that heme site is probably the main binding site of the investigated compounds. However, taking into account that hemin affinity to HSA is of nanomolar order, at 10 μM concentration of hemin almost all its binding sites would be occupied (Zunszain et al., 2003). At the same time, the fluorescence of the PSs still significantly exceeded that of their free forms. This confirms the assumption that several binding sites are involved in the binding of the PSs. Indeed, the emission of the PSs decreased also in the presence of two other site markers, though their relatively high concentrations were required to obtain a significant decrease. At low concentrations of warfarin and ibuprofen (≤2 μM) the fluorescence of Zn-Pheide was not reduced. Interestingly, low concentrations of ibuprofen even increased the emission of Zn-Pheide (Figure 7(C)). This effect could be explained by the fact that ibuprofen induces significant structural alteration in the heme binding cavity (subdomain IB), which may increase the affinity of Zn-Pheide to this site, similarly as it is in the case of heme (Nicoletti et al., 2008). Importantly, the decrease of the fluorescence signal was in each case higher for Chlide than for Zn-Pheide, confirming that the binding of the latter is stronger. The largest difference between the PSs were observed in their displacement by warfarin, suggesting that they considerably differ in the affinities of binding to Sudlow's site I.

Molecular docking studies were performed using the AutoDock 4.2 software to structurally investigate possible interactions sites between the PSs and HSA. Similarly to the displacement study, three probable binding sites were chosen, based on literature reports in the field of binding porphyrin-like compounds to albumin (Chaves et al., 2015; Sułkowski et al., 2016, 2020). These were Sudlow's sites I and II, as well as the heme site. The study revealed favorable interactions ($\Delta G < 0$) of both PSs with all binding sites. The cluster with the lowest binding energy was in each case the most numerous cluster. The obtained docking poses with the lowest binding energies are shown in Figure 8, and the
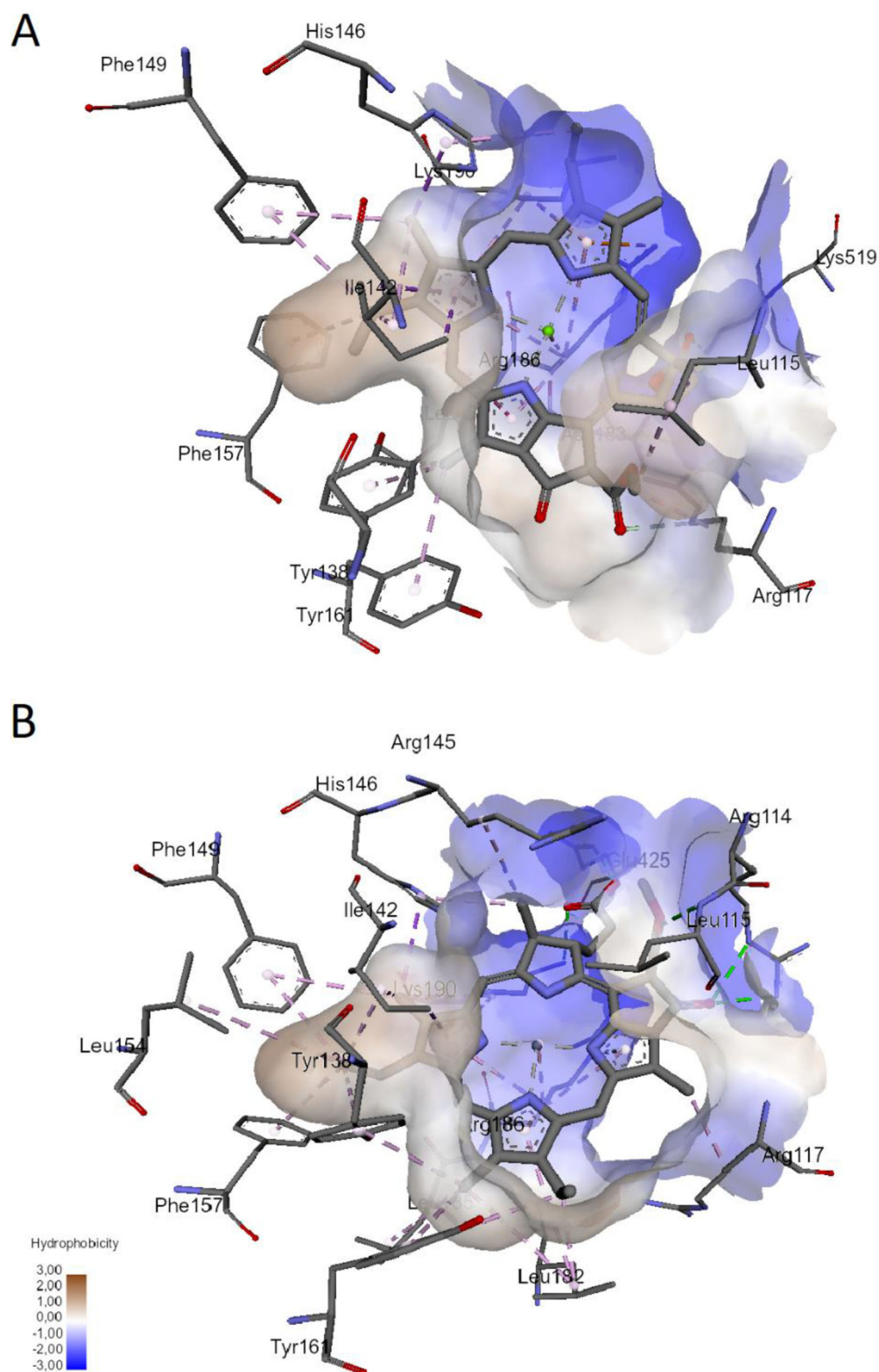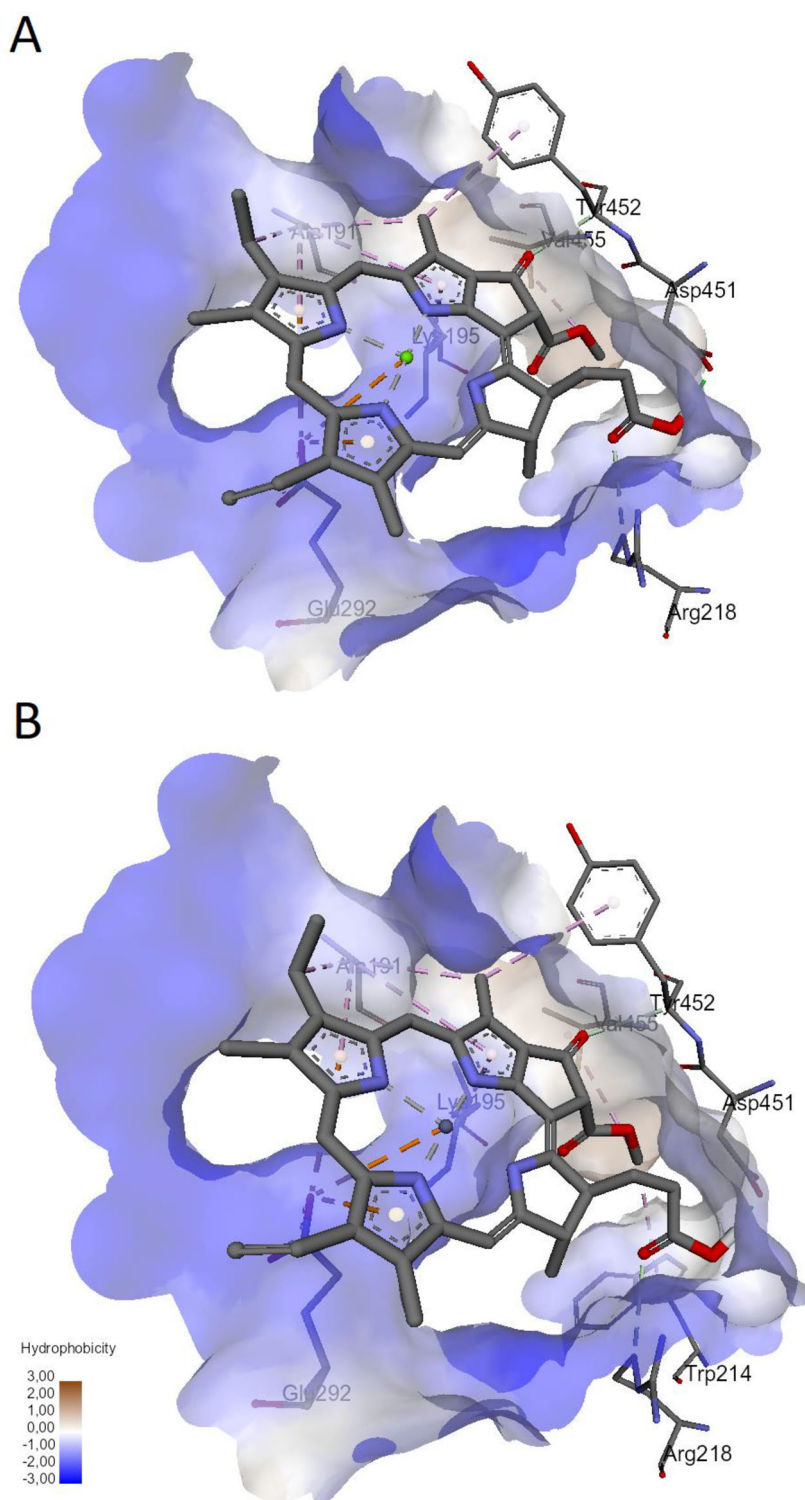
Figure 9. Interactions between the PSs and HSA in the heme site revealed by molecular docking. The positions with the lowest binding energies are shown. (A) Chlide, (B) Zn-Pheide. H-bonds are shown in green and hydrophobic interactions (alkyl, π-alkyl and π-σ) in violet.

interactions of the PSs with the residues within particular binding sites are presented in Figures 9–11.

In Figures 9–11 we show the interactions of Chlide and Zn-Pheide with the heme site and the Sudlow's sites corresponding to the lowest binding energy positions. Additionally, in Table 3 we summarize the main residues involved in the interactions with particular binding sites together with the calculated binding energies. Despite the fact that the lowest energy positions obtained for Chlide and Zn-Pheide largely overlapped (Figure 8), their interactions with the amino acid residues forming each binding site were not the same. Generally, more residues were involved in the
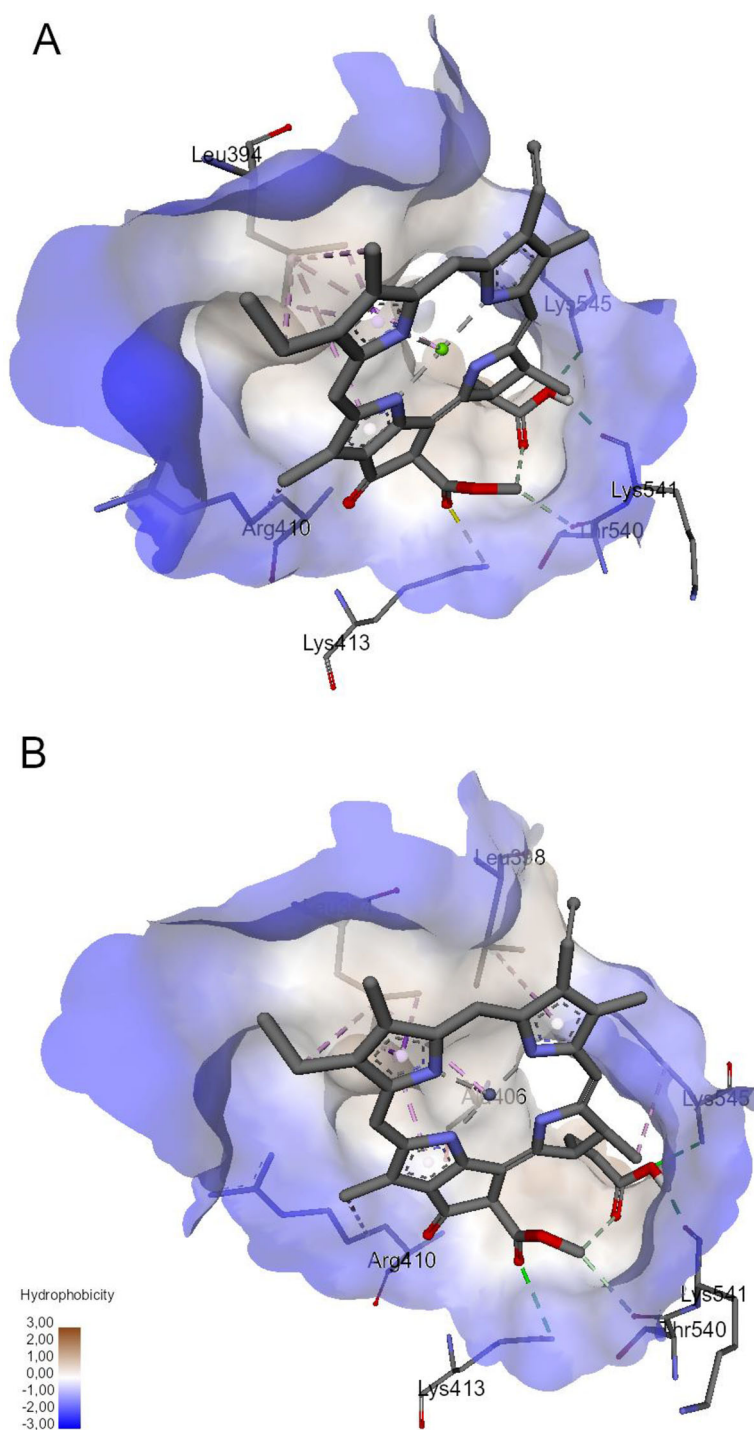
Figure 10. Interactions between the PSs and HSA in Sudlow's site I revealed by molecular docking. The positions with the lowest binding energies are shown. (A) Chlide, (B) Zn-Pheide. H-bonds are shown in green, hydrophobic interactions (alkyl, π-alkyl and π-σ) in violet and π-anion interactions in orange]

interactions with Zn-Pheide than with Chlide, which resulted in lower values of the binding energies obtained for the former in each binding site (Table 3). The only residue interacting with Chlide but not with Zn-Pheide was Lys519, which participated in the H-bond formation in the heme site. Importantly, we did not observe the characteristic axial coordination of His, Met, Lys or Cys residues, which occurs between chlorophylls and proteins of light harvesting

complexes or between heme and apoproteins of hemoglobin, myoglobin or cytochromes (Buchler et al., 1976; Hoober et al., 2007; Lu et al., 2001). Instead, binding of the metal-substituted pheophorbides to HSA seems to be driven predominantly by hydrophobic interactions.

The PSs were found to be buried deeply inside the hydrophobic pockets of the heme site and Sudlow's site I and their binding was stabilized predominantly by alkyl-alkyl π-alkyl

Figure 11. Interactions between the PSs and HSA in Sudlow's site II revealed by molecular docking. The positions with the lowest binding energies are shown. (A) Chlide, (B) Zn-Pheide. H-bonds are shown in green and hydrophobic interactions (alkyl, π-alkyl and π-σ) in violet.

and π-σ interactions. The largest number of hydrophobic interactions was observed for both PSs in the heme site. Amino acid residues involved in these interactions were Leu115, Arg117, Tyr138, Ile142, His146, Phe149, Phe157, Tyr161, Leu185, Arg186, Lys190 for both PSs, and additionally Arg145, Leu154, Leu182 for Zn-Pheide. Compared to the heme site, the number of residues participating in hydrophobic interactions was significantly lower in Sudlow's site I. The residues common for both PSs were in this case Tyr452, Val 455, Ala191 and Lys 195, and for Zn-Pheide additionally Trp214. Direct interaction of Zn-Pheide with Trp214 was

reflected in stronger HSA fluorescence quenching by Zn-Pheide than by Chlide (Figure 5). Only one residue involved in hydrophobic interactions in Sudlow's site II common for both PSs was identified. This was Leu 394. Three additional residues participated in these interactions in the case of Zn-Pheide. These were Leu398, Ala406 and Lys545.

In addition, at the hydrophilic entrances to the binding cavities, hydrogen bonds were formed with the participation of the PS side chains. The residues involved in these interactions were common to both PSs in the Sudlow's sites but differed in the heme site, where only one residue (Lys519)

Table 3. Characteristics of the PS-binding sites in the structure of HSA predicted on the basis of molecular docking.

Compound	Binding site	Main interacting residues	ΔG (kJ/mol)	$K_a/10^6$ (M^{-1})
Chlide	Heme	Leu115, **Arg117**, Tyr138, Ile142, His146, Phe149, Phe157, Tyr161, **Asp183**, Leu185 Arg186, Lys190, **Lys519**	−51.09	410.14
	Sudlow I	Ala191, Lys195, **Arg218**, Glu292, **Asp451**, **Tyr452**, Val455	−34.89	0.76
	Sudlow II	Leu394, Arg410, **Lys413**, **Thr540**, **Lys541**, **Lys545**	−33.68	0.48
Zn-Pheide	Heme	**Arg114**, **Leu115**, Arg117, Tyr138, Ile142, Arg145, His146, Phe149, Leu154, Phe157, Tyr161, Leu182, Leu185, Arg186, **Lys190**, Glu425	−52.43	689.86
	Sudlow I	Ala191, Lys195, Trp214, **Arg218**, Glu292, Asp451, Tyr452, Val455	−35.61	1.01
	Sudlow II	Leu394, Leu398, Arg406, Arg410, **Lys413**, Thr540, Lys541, Lys545	−35.10	0.85

Data obtained using the AutoDock 4.2 and Discovery Studio Visualizer software. Amino acid residues forming hydrogen bonds are written in bold. The residues interacting with only one of the PSs are underlined. The binding affinities (K_a) are calculated for the temperature of 310 K.

formed a H-bond with Chlide but 3 residues (Arg114, Leu115 and Glu425) with Zn-Pheide (Figure 9).

In summary, the results of molecular docking study indicate that the primary binding site for the investigated PSs is the heme site, however the binding of lower affinity is likely to occur in the other sites. Additionally, the binding of Zn-Pheide to HSA is stronger than that of Chlide, showing that a slight structural difference in the form of central metal ion exchange regulates the affinity of chlorophyll derivatives to HSA.

Conclusions

The results obtained in the present study indicate that the heme site, and to a lesser extent Sudlow's sites I and II of HSA are involved in the binding of metal-substituted pheophorbides. The binding to all identified binding sites occurs primarily *via* hydrophobic interactions. The determined binding affinities of both PSs to HSA are much lower than that of heme ($\sim10^8$ M^{-1}) but comparable to that of protoporphyrin IX ($\sim10^5$ M^{-1}), and stronger than that of other plant-derived porphyrin, pheophytin ($\sim10^4$ M^{-1}), at least in one of the binding sites (Chaves et al., 2015; Kamal & Behere, (2005); Sułkowski et al., 2016). Since the identified binding sites are of the same order as that for protoporphyrin IX, it is likely that the investigated PSs may compete with this endogenous PS for binding to HSA. On the other hand, ligands with strong affinities to the Sudlow's sites and the heme site are likely to displace the bound PSs, thus increasing the concentration of their free forms. This can have a profound influence on the bioavailability of the PSs and as a consequence, on their efficacy *in vivo* (Szafraniec & Fiedor, 2021). Additionally, the concentrations of free PSs are likely to increase in patients with hypoalbuminemia, which is a state often associated with cancer (Navalkele et al., 2016; Takaaki et al., 2020). The affinities of binding determined for Zn-Pheide are higher than the corresponding affinities for Chlide, indicating that the central metal noticeably influences the binding. This may explain the previously observed differences in the pharmacokinetics of the investigated compounds and confirm that, similarly to animals, they are also likely to occur in humans (Szafraniec & Fiedor, 2021; Szczygieł et al., 2008).

Disclosure statement

No potential conflict of interest was reported by the authors.

References

ACD/ChemSketch, version 2.1. (2020). Advanced Chemistry Development, Inc. www.acdlabs.com.

Ascenzi, P., Bocedi, A., Notari, S., Menegatti, E., & Fasano, M. (2005). Heme impairs allosterically drug binding to human serum albumin Sudlow's site I. *Biochemical and Biophysical Research Communications*, *334*(2), 481–486. https://doi.org/10.1016/j.bbrc.2005.06.127

Barakat, C., & Patra, D. (2013). Combining time-resolved fluorescence with synchronous fluorescence spectroscopy to study bovine serum albumin-curcumin complex during unfolding and refolding processes. *Luminescence*, *28*(2), 149–155. https://doi.org/10.1002/bio.2354

Baroni, S., Mattu, M., Vannini, A., Cipollone, R., Aime, S., Ascenzi, P., & Fasano, M. (2001). Effect of ibuprofen and warfarin on the allosteric properties of haem-human serum albumin: A spectroscopic study. *European Journal of Biochemistry*, *268*(23), 6214–6220. https://doi.org/10.1046/j.0014-2956.2001.02569.x

Batista, A. N. L., Batista, J. M., Ashton, L., Bolzani, V. S., Furlan, M., & Blanch, E. W. (2014). Investigation of DMSO-induced conformational transitions in human serum albumin using two-dimensional Raman optical activity spectroscopy. *Chirality*, *26*(9), 497–501. https://doi.org/10.1002/chir.22351

BIOVIA. (2021). *Discovery Studio Visualizer, version 2021*. Dassault Systèmes.

Bonnett, R. (2003). Metal complexes for photodynamic therapy. *Comprehensive Coordination Chemistry II*, 945–1003. https://doi.org/10.1016/B0-08-043748-6/09204-5.

Buchler, J. W., Lay, K. L., Smith, P. D., Scheidt, W. R., Rupprecht, G. A., & Kenny, J. E. (1976). Metal complexes with tetrapyrrole ligands. *Journal*

of Organometallic Chemistry., *110*(1), 109–120. https://doi.org/10.1016/S0022-328X(00)90164-5

Carter, D. C., He, X. M., Munson, S. H., Twigg, P. D., Gernert, K. M., Broom, M. B., & Miller, T. Y. (1989). Three-dimensional structure of human serum albumin. *Science (New York, N.Y.)*, *244*(4909), 1195–1198. https://doi.org/10.1126/science.2727704

Chaves, O. A., de, A., Amorim, P. O., Castro, L. H. E., Sant'Anna, C. M. R., De Oliveira, M. C. C., Cesarin-Sobrinho, D., Netto-Ferreira, J. C., & Ferreira, A. B. B. (2015). Fluorescence and docking studies of the interaction between human serum albumin and pheophytin. *Molecules (Basel, Switzerland)*, *20*(10), 19526–19539. https://doi.org/10.3390/molecules201019526

Cui, F., Yan, Y., Zhang, Q., Du, J., Yao, X., Qu, G., & Lu, Y. (2009). Characterization of the interaction between 2′-deoxyuridine and human serum albumin . *Carbohydrate Research*, *344*(5), 642–647. https://doi.org/10.1016/j.carres.2009.01.009

Fiedor, L., Kania, A., Myśliwa-Kurdziel, B., Orzeł, Ł., & Stochel, G. G. (2008). Understanding chlorophylls: Central magnesium ion and phytyl as structural determinants. *Biochimica et Biophysica Acta*, *1777*(12), 1491–1500. https://doi.org/10.1016/j.bbabio.2008.09.005

Ge, F., Chen, C., Liu, D., Han, B., Xiong, X., & Zhao, S. (2010). Study on the interaction between theasinesin and human serum albumin by fluorescence spectroscopy. *Journal of Luminescense*, *130*(1), 168–173. https://doi.org/10.1016/j.jlumin.2009.08.003

Ghisaidoobe, A. B. T., & Chung, S. J. (2014). Intrinsic Tryptophan fluorescence in the detection and analysis of proteins: A focus on Förster resonance energy transfer techniques. *International Journal of Molecular Sciences*, *15*(12), 22518–22538. https://doi.org/10.3390/ijms151222518

Hartwich, G., Fiedor, L., Simonin, I., Cmiel, E., Schäfer, W., Noy, D., Scherz, A., & Scheer, H. (1998). Metal-substituted bacteriochlorophylls. 1. Preparation and influence of metal and coordination on spectra. *Journal of the American Chemical Society*, *120*(15), 3675–3683. https://doi.org/10.1021/ja970874u

Hosainzadeh, A., Gharanfoli, M., Saberi, M. R., & Chamani, J. K. (2012). Probing the interaction of human serum albumin with bilirubin in the presence of aspirin by multi-spectroscopic, molecular modeling and zeta potential techniques: Insight on binary and ternary systems. *Journal of Biomolecular Structure & Dynamics*, *29*(5), 1013–1050. https://doi.org/10.1080/073911012010525029

Hoober, J. K., Eggink, L. L., & Chen, M. (2007). Chlorophylls, ligands and assembly of light-harvesting complexes in chloroplasts. *Photosynth Res*, *94*(2-3), 387–400. https://doi.org/10.1007/s11120-007-9181-1

Jahanban-Esfahlan, A., Davaran, S., Moosavi-Movahedi, A. A., & Dastmalchi, S. (2017). Investigating the interaction of juglone (5-hydroxy-1, 4-naphthoquinone) with serum albumins using spectroscopic and in silico methods. *Journal of the Iranian Chemical Society*, *14*(7), 1527–1540. https://doi.org/10.1007/s13738-017-1094-0

Jahanban-Esfahlan, A., Panahi-Azar, V., & Sajedi, S. (2015). Spectroscopic and molecular docking studies on the interaction between N-acetyl cysteine and bovine serum albumin. *Biopolymers*, *103*(11), 638–645. https://doi.org/10.1002/bip.22697

Jahanban-Esfahlan, A., Panahi-Azar, V., & Sajedi, S. (2016). Interaction of glutathione with bovine serum albumin: Spectroscopy and molecular docking. *Food Chemistry*, *202*, 426–431. https://doi.org/10.1016/j.foodchem.2016.02.026

Jahanban-Esfahlan, A., Roufegarinejad, L., Tabibiazar, M., Lorenzo, J. M., & Amarowicz, R. (2021). Exploring the interactions between caffeic acid and human serum albumin using spectroscopic and molecular docking techniques. *Polish Journal of Food and Nutrition Sciences*, *71*, 69–77. https://doi.org/10.31883/pjfns/133203

Jakubowska, M., Szczygieł, M., Michalczyk-Wetula, D., Susz, A., Stochel, G., Elas, M., Fiedor, L., & Urbanska, K. (2013). Zinc-pheophorbide a-highly efficient low-cost photosensitizer against human adenocarcinoma in cellular and animal models. *Photodiagnosis and Photodynamic Therapy*, *10*(3), 266–277.10.1016/j.pdpdt.2012.12.004. https://doi.org/10.1016/j.pdpdt.2012.12.004

Kamal, J. K. A., & Behere, D. V. (2005). Binding of heme to human serum albumin: Steady-state fluorescence, circular dichroism and optical difference spectroscopic studies. *Indian Journal of Biochemistry & Biophysics*, *42*(1), 7–12.

Kragh-Hansen, U., Chuang, V. T. G., & Otagiri, M. (2002). Practical aspects of the ligand-binding and enzymatic properties of human serum albumin. *Biological & Pharmaceutical Bulletin*, *25*(6), 695–704. https://doi.org/10.1248/bpb.25.695

Lakowicz, J. R. (2006). *Principles of Fluorescence Spectroscopy*. Springer. https://doi.org/10.1007/978-0-387-46312-4.

Lu, Y., Berry, S. M., & Pfister, T. D. (2001). Engineering novel metalloproteins: Design of metal-binding sites into native protein scaffolds. *Chemical Reviews*, *101*(10), 3047–3080. https://doi.org/10.1021/cr0000574

Mazière, J. C., Morlière, P., & Santus, R. (1991). New trends in photobiology. The role of the low density lipoprotein receptor pathway in the delivery of lipophilic photosensitizers in the photodynamic therapy of tumours. *Journal of Photochemistry and Photobiology B: Biology*, *8*(4), 351–360. https://doi.org/10.1016/1011-1344(91)80111-T

Morris, G. M., Huey, R., Lindstrom, W., Sanner, M. F., Belew, R. K., Goodsell, D. S., & Olson, A. J. (2009). AutoDock4 and AutoDockTools4: Automated docking with selective receptor flexibility. *Journal of Computational Chemistry*, *30*(16), 2785–2791.10.1002/jcc.21256. https://doi.org/10.1002/jcc.21256

Navalkele, P., Belgrave, K., Altinok, D., Bhambhani, K., Taub, J. W., & Wang, Z. J. (2016). Hypoalbuminemia associated with neuroblastoma: A single institution experience. *Annals of Pediatrics and Child Health*, *4*, 1–5. https://www.jscimedcentral.com/Pediatrics/pediatrics-4-1115.pdf.

Neese, F., Wennmohs, F., Becker, U., & Riplinger, C. (2020). The ORCA quantum chemistry program package. *The Journal of Chemical Physics*, *152*(22), 224108. https://doi.org/10.1063/5.0004608

Nicoletti, F. P., Howes, B. D., Fittipaldi, M., Fanali, G., Fasano, M., Ascenzi, P., & Smulevich, G. (2008). Ibuprofen induces an allosteric conformational transition in the heme complex of human serum albumin with significant effects on heme ligation. *Journal of the American Chemical Society*, *130*(35), 11677–11688. https://doi.org/10.1021/ja800966t

O'Boyle, N. M., Banck, M., James, C. A., Morley, C., Vandermeersch, T., & Hutchison, G. R. (2011). Open Babel: An open chemical toolbox. *Journal of Cheminformatics*, *3*, 33–14. https://doi.org/10.1186/1758-2946-3-33.

Origin, Version (2021). OriginLab Corporation.

Ouameur, A. A., Marty, R., Supe, E., & Tajmir-Riahi, H. A. (2005). Human serum albumin complexes with chlorophyll and chlorophyllin. *Biopolymers*, *77*(3), 129–136. https://doi.org/10.1002/bip.20173

Poór, M., Li, Y., Kunsági-Máté, S., Petrik, J., Vladimir-Knežević, S., & Kőszegi, T. (2013). Molecular displacement of warfarin from human serum albumin by flavonoid aglycones. *Journal of Luminescense*, *142*, 122–127. https://doi.org/10.1016/j.jlumin.2013.03.056

Roufegarinejad, L., Amarowicz, R., & Jahanban-Esfahlan, A. (2019). Characterizing the interaction between pyrogallol and human serum albumin by spectroscopic and molecular docking methods. *Journal of Biomolecular Structure & Dynamics*, *37*(11), 2766–2775. https://doi.org/10.1080/07391102.2018.1496854

Schrödinger, LLC. (2010). *The PyMOL Molecular Graphics System, Version 1.3*. Schrödinger, LLC.

Sudlow, G., Birkett, D. J., & Wade, D. N. (1975). The characterization of two specific drug binding sites on human serum albumin. *Molecular Pharmacology*, *11*(6), 824–832.

Sudlow, G., Birkett, D. J., & Wade, D. N. (1976). Further characterization of specific drug binding sites on human serum albumin. *Molecular Pharmacology*, *12*(6), 1052–1061. http://molpharm.aspetjournals.org/content/11/6/824.abstract.

Sułkowski, L., Osuch, C., Matyja, M., & Matyja, A. (2020). Hematoporphyrin binding sites on human serum albumin. *Archives of Medical Science-Civilization Diseases*, *5*(1), 1–7. https://doi.org/10.5114/amscd.2020.92722

Sułkowski, L., Pawełczak, B., Chudzik, M., & Maciążek-Jurczyk, M. (2016). Characteristics of the protoporphyrin IX binding sites on human serum albumin using molecular docking. *Molecules*, *21*(11), 1519. https://doi.org/10.3390/molecules21111519

Szafraniec, M. J., & Fiedor, L. (2021). One ring is not enough to rule them all. Albumin-dependent ABCG2-mediated transport of chlorophyll-derived photosensitizers. *European Journal of Pharmaceutical Sciences*, *167*, 106001. https://doi.org/10.1016/j.ejps.2021.106001

Szczygieł, M., Boroń, B., Szczygieł, D., Szafraniec, M., Susz, A., Matuszak, Z., Urbańska, K., & Fiedor, L. (2014). Real-time non-invasive

transdermal monitoring of photosensitizer level in vivo for pharmaco-kinetic studies and optimization of photodynamic therapy protocol. *Journal of Analytical & Bioanalytical Techniques*, *5*, 227. https://doi.org/10.4172/2155-9872.1000227

Szczygieł, M., Urbańska, K., Jurecka, P., Stawoska, I., Stochel, G., & Fiedor, L. (2008). Central metal determines pharmacokinetics of chlorophyll-derived xenobiotics. *Journal of Medicinal Chemistry*, *51*(15), 4412–4418. https://doi.org/10.1021/jm7016368

Takaaki, F., Tokuda, S., Nakazawa, Y., Kurozumi, S., Obayashi, S., Yajima, R., & Shirabe, K. (2020). Implications of low serum albumin as a prognostic factor of long-term outcomes in patients with breast cancer. *In Vivo (Vivo)*, *34*(4), 2033–2036. https://doi.org/10.21873/invivo.12003

Zunszain, P. A., Ghuman, J., Komatsu, T., Tsuchida, E., & Curry, S. (2003). Crystal structural analysis of human serum albumin complexed with hemin and fatty acid. *BMC Structural Biology*, *3*, 6. https://doi.org/10.1186/1472-6807-3-6

Supplementary materials

Calculation of HSA-bound PS fluorescence

For calculation of the HSA-bound fraction of Chlide and Zn-Pheide in the fluorescence enhancement study, we assumed that the fluorescence intensity of a PS measured at a given concentration of HSA is given as:

$$F = F_b \cdot B + F_f \cdot (T - B), \tag{1}$$

where F is the experimentally determined fluorescence at a given concentration of HSA, F_b is the specific molar fluorescence intensity of bound PS, B is the concentration of bound PS, F_f is the specific molar fluorescence intensity of free PS, and T is the total PS concentration (equal to 1 µM in the present study).

The equation (1) can be written as:

$$F = F_b \cdot B + F_f \cdot T - F_f \cdot B, \tag{2}$$

or when we substitute $F_0 = F_f \cdot T$ as a PS fluorescence in the absence of HSA:

$$F = F_b \cdot B + F_0 - \frac{F_0}{T} \cdot B \tag{3}$$

We observed that up to 1 µM of the PSs, their fluorescence signals are linearly dependent on the concentration, therefore F_f has a constant value, which can be easily determined from an appropriate calibration curve.

Thus:

$$\frac{F}{F_0} = \frac{F_b}{F_0} \cdot B + 1 - \frac{1}{T} \cdot B \tag{4}$$

And rearranging yields:

$$\frac{F}{F_0} - 1 = \left(\frac{F_b}{F_0} - \frac{1}{T} \right) \cdot B \tag{5}$$

Therefore:

$$B = \frac{\dfrac{F}{F_0} - 1}{\dfrac{F_b}{F_0} - \dfrac{1}{T}} \tag{6}$$

At sufficiently high HSA concentrations, a saturation of the fluorescence signal was observed. Since upon saturation all the ligand is bound ($B = T$), the maximal obtained fluorescence signal, F_{max}, is equal to:

1

$$F_{max} = F_b \cdot T \, , \tag{7}$$

therefore:

$$F_b = \frac{F_{max}}{T} \, , \tag{8}$$

and:

$$B = \frac{\dfrac{F}{F_0} - 1}{\dfrac{F_{max}}{F_0 \cdot T} - \dfrac{1}{T}} \tag{9}$$

or:

$$B = \frac{\left(\dfrac{F}{F_0} - 1\right) \cdot T}{\dfrac{F_{max}}{F_0} - 1} \tag{10}$$

And the fluorescence of bound ligand fraction, $F(B)$, equals to:

$$F(B) = \frac{\left(\dfrac{F}{F_0} - 1\right) \cdot T}{\dfrac{F_{max}}{F_0} - 1} \cdot F_{max} \tag{11}$$

2

Article

Zinc-Substituted Pheophorbide A Is a Safe and Efficient Antivascular Photodynamic Agent

Milena J. Szafraniec [1,2,*] , Monika Toporkiewicz [2] and Andrzej Gamian [1]

1   Hirszfeld Institute of Immunology and Experimental Therapy, Polish Academy of Sciences, 53-114 Wrocław, Poland; andrzej.gamian@hirszfeld.pl
2   Łukasiewicz Research Network—PORT Polish Center for Technology Development, 54-066 Wrocław, Poland; monika.toporkiewicz@port.lukasiewicz.gov.pl
*   Correspondence: milena.szafraniec@hirszfeld.pl

Abstract: The present study focuses on the photodynamic activity of zinc-substituted pheophorbide a against human endothelial cells. Previously, zinc pheophorbide a has been shown to be a very potent photosensitizer but also a strong albumin binder. Binding to albumin significantly reduces its availability to cancer cells, which may necessitate the use of relatively high doses. Here we show that zinc pheophorbide a is very effective against vascular endothelial cells, even in its albumin-complexed form. Albumin complexation increases the lysosomal accumulation of the drug, thus enhancing its efficiency. Zinc pheophorbide a at nanomolar concentrations induces endothelial cell death via apoptosis, which in many cases is considered a desirable cell death mode because of its anti-inflammatory effect. Additionally, we demonstrate that in comparison to tumor cells, endothelial cells are much more susceptible to photodynamic treatment with the use of the investigated compound. Our findings demonstrate that zinc pheophorbide a is a very promising photosensitizer for use in vascular-targeted photodynamic therapy against solid tumors, acting as a vascular shutdown inducer. It can also possibly find application in the treatment of a range of vascular disorders. Numerous properties of zinc pheophorbide a are comparable or even more favorable than those of the well-known photosensitizer of a similar structure, palladium bacteriopheophorbide (TOOKAD®).

Keywords: zinc pheophorbide a; chlorophyll derivatives; photodynamic therapy; serum albumin; apoptosis; endothelium; HUVEC

1. Introduction

Photodynamic therapy is an evolving modality for the treatment of a range of both neoplastic and non-neoplastic diseases. It involves either the systemic or local administration of a photosensitive drug (photosensitizer, PS) followed by site-specific irradiation with visible light of a specific wavelength. This induces either the electron transfer processes (type I reaction) or a formation of highly reactive singlet oxygen (type II reaction), which destroy a diseased tissue [1,2].

A particular variant of photodynamic therapy is vascular-targeted photodynamic therapy (VTP), which uses a PS accumulated not in tumor tissue itself, but in the surrounding blood vessels. Vascular damage due to VTP results in vessel constriction, blood flow stasis, and thrombus formation, which consequently blocks the supply of oxygen and nutrients, causing tumor necrosis [3]. The advantages of VTP over traditional photodynamic therapy include: (1) the use of hydrophilic PSs, which, due to their short retention time, do not generate adverse photosensitization of a patient; (2) the rapid localization of a PS in endothelium; (3) the availability of molecular oxygen required for a photochemical reaction; (4) the amplified effect on tumor cells resulting from the supply of multiple tumor cells through a single vessel [3,4]. Currently, three vascular-targeted photosensitizers, namely palladium bacteriopheophorbide (TOOKAD®), its water-soluble derivative padeliporfin

(WST11), and verteporfin (Visudyne®), are approved for clinical use [5,6]. Nevertheless, new vascular-targeted PSs with increased selectivity and efficacy are still being sought. Their design often includes the usage of different types of targeting moieties, such as peptides, antibodies, or nanocarrier systems, which allow acting on specific molecular pathways [3,7].

Pheophorbide a is a natural product of chlorophyll a breakdown, formed via its demetallation and the removal of phytol. Zinc pheophorbide a (Zn-Pheide, Figure 1) is a semi-synthetic derivative of pheophorbide a with a much higher water solubility compared to its precursor [8]. It possesses excellent photodynamic properties, including strong light absorption in the therapeutic window of human tissue, low dark toxicity, and high efficiency of reactive oxygen species generation [8–12]. Zinc pheophorbide a has already been shown to exert a very strong photodynamic effect against human adenocarcinoma and mouse melanoma in vivo [10,11]. On the other hand, however, in our previous studies we showed that Zn-Pheide binds strongly to albumin, which significantly impairs its uptake by tumor cells, thus reducing it efficacy [13,14]. Considering that, we hypothesized that the strong photodynamic effect of Zn-Pheide observed in vivo might be due to its high activity against tumor vessels endothelium, since endothelial cells are known to express albumin-binding receptors potentially involved in the uptake of PS–albumin complexes. The most thoroughly characterized albumin receptor is gp60 (albondin), which initiates the process of the caveolin-mediated endocytosis of albumin, in which caveolin-1 plays the major role [15].
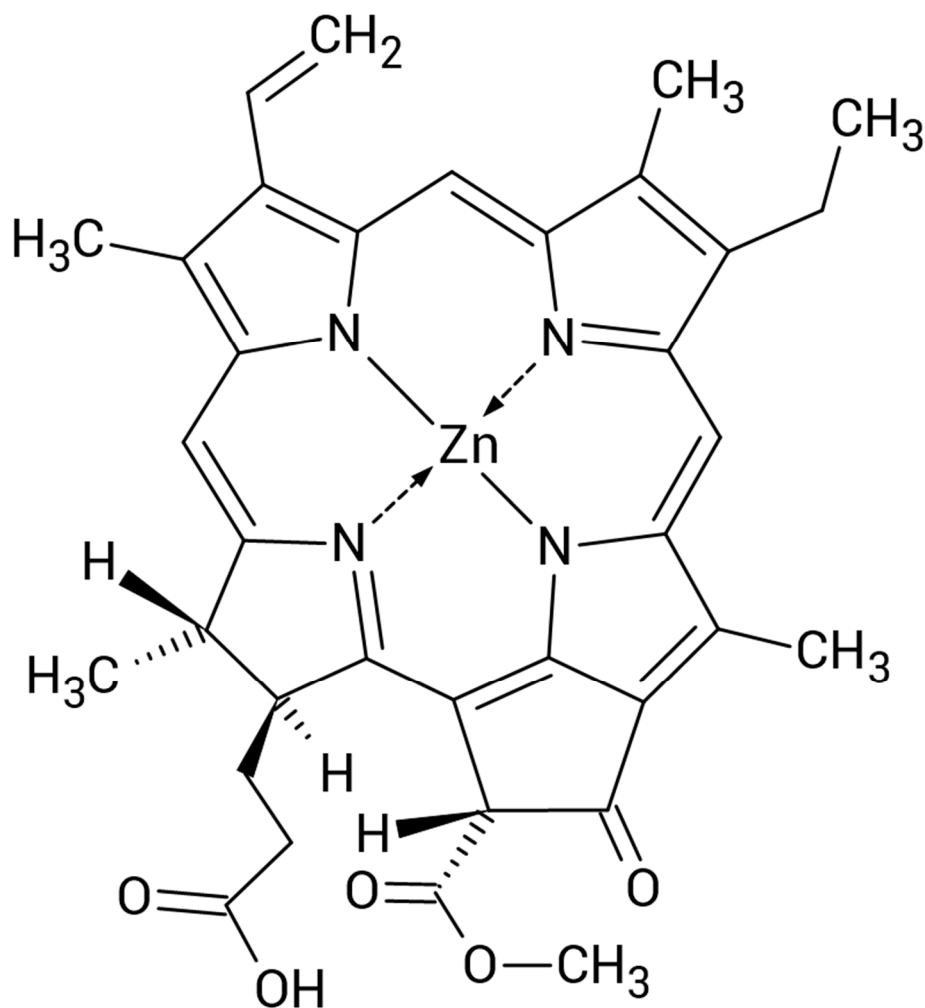

Figure 1. Chemical structure of zinc pheophorbide a.

In light of the above, a question arose whether the Zn-Pheide–albumin complex is recognized by gp60 and internalized via caveolin-1-mediated endocytosis, similarly to free albumin and albumin-bound paclitaxel (Abraxane®) [15–17]. Moreover, given the antioxidant properties of albumin, we also considered whether the possible uptake of the PS in its albumin-complexed form would affect its photodynamic activity [18]. Revealing a photodynamic potential of Zn-Pheide against endothelial cells would make it a candidate for a vascular-targeted PS, applicable not only in the treatment of solid tumors but also several vascular anomalies, such as hemangiomas, venous and arteriovenous malformations, as well as capillary malformations known as port-wine stains [19,20].

The aim of the present study was therefore to investigate the photodynamic activity of Zn-Pheide against human endothelial cells, particularly in the context of its naturally occurring complexation with serum albumin and transport via the breast cancer resistance protein (BCRP, ABCG2), which are interrelated [13]. The experiments were carried out using human umbilical vein endothelial cells (HUVECs), being one of the most commonly used model systems to study vascular biology in vitro and shown to perform the transcytosis of albumin via the gp60 receptor and caveolin-1 protein [21]. We evaluated the impact of binding to albumin on the cellular accumulation, localization, and efflux of the PS, as well as on the photodynamic effect induced with its application. In addition, we compared HUVEC cells with human breast carcinoma cells (MCF-7) in terms of their susceptibility to Zn-Pheide-mediated photodynamic treatment (PDT), particularly in the context of the binding of the PS to albumin. Furthermore, we investigated the type of cell death induced by Zn-Pheide both in the presence and absence of albumin. Additionally, based on literature reports, we compared the photophysical and pharmacokinetic parameters of Zn-Pheide with those of other PSs of similar structure used in VTP, thus assessing the applicability of the former in the VTP of cancer and other diseases.

2. Results

The experiments on the MCF-7 and HUVEC cell lines with the use of Zn-Pheide were initiated by determining the dark cytotoxicity of the PS. The results of these assays are presented in Figure S1 (Supplementary Materials). The PS at a concentration of 1 µM with a 3 h incubation was found to be nontoxic to both lines, therefore this concentration or lower concentrations were used in subsequent studies.

In our previous studies, we observed that at a human serum albumin (HSA) concentration 250 times higher than the concentration of Zn-Pheide, saturation occurs, i.e., Zn-Pheide is completely bound to HSA [14]. Therefore, we compared the accumulation and the corresponding PDT effect induced by Zn-Pheide in MCF-7 and HUVEC cells, both in the absence of albumin and at its saturating concentration. The results of these experiments are shown in Figure 2A,B. In the absence of albumin, the accumulation of Zn-Pheide in MCF-7 and HUVEC cells was similar (Figure 2A). At the saturating concentration of HSA, in turn, the level of Zn-Pheide was significantly decreased in both cell lines, although the HUVECs accumulated roughly a two-fold higher amount of the PS than MCF-7. The photodynamic effect induced by 1 µM Zn-Pheide in MCF-7 cells at the applied PDT conditions was completely abolished in the presence of HSA (Figure 2B). On the other hand, in the case of HUVECs, as much as 80% of the cells were killed when Zn-Pheide was complexed with HSA.

The observed decrease in accumulation of Zn-Pheide in the presence of HSA could be due to HSA–PS complex formation as well as the efflux of Zn-Pheide via the BCRP (ABCG2) transporter, which is significantly increased in the presence of albumin [13]. To evaluate the involvement of BCRP in the regulation of the PS level in both cell lines, the expression of this transporter was determined at the mRNA level by quantitative real-time PCR. The expression of BCRP was found to be two-fold lower in HUVECs than in MCF-7 cells (Figure 2C).
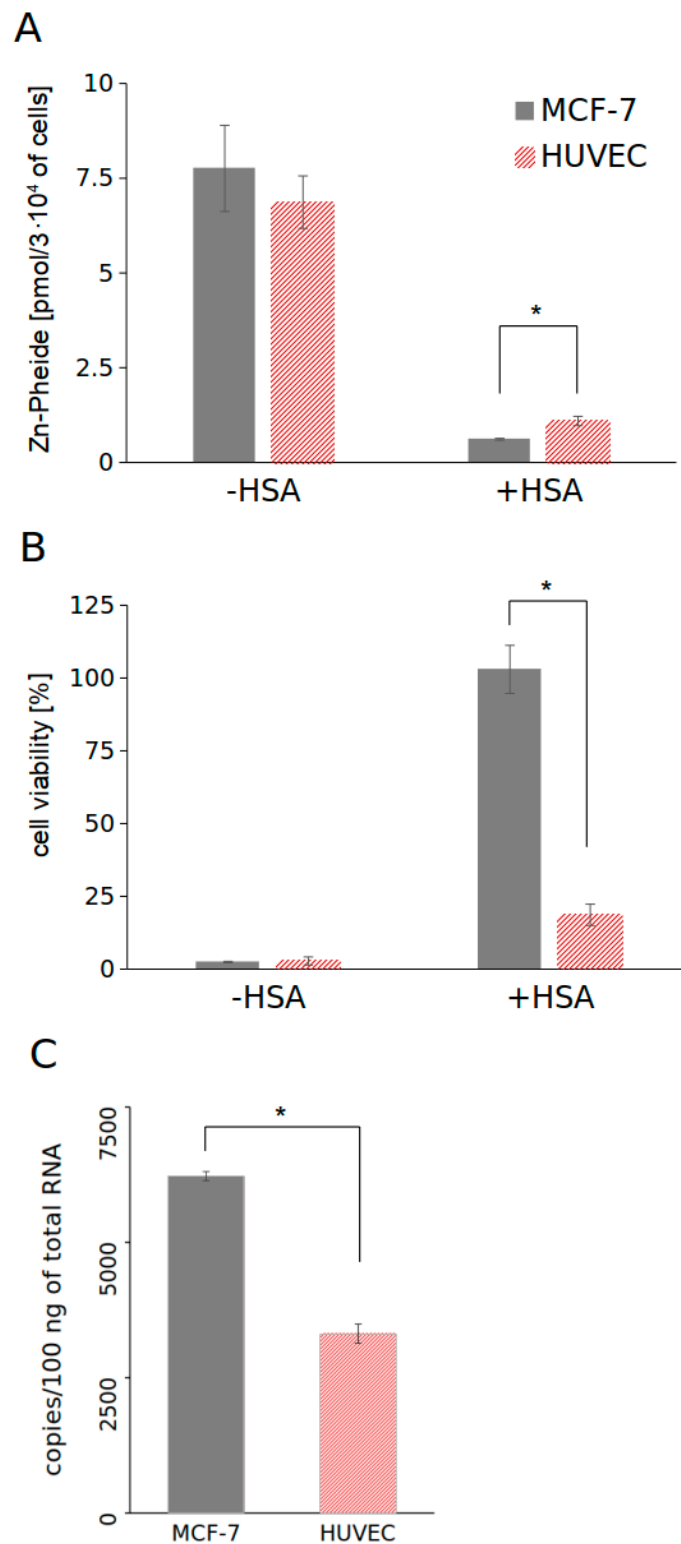
Figure 2. Comparison of cellular accumulation of Zn-Pheide (**A**), cell viability after Zn-Pheide-induced PDT (**B**), and expression of the *ABCG2* gene (**C**) in MCF-7 and HUVEC cells. Cellular accumulation of the PS and cell viability after PDT were measured in the presence and absence of HSA (250 µM). The concentration of Zn-Pheide in both experiments was equal to 1 µM. Expression of BCRP was determined by quantitative real-time PCR. Data are presented as mean ± SD, $n = 3$. Significant differences between HUVECs and MCF-7 cells are indicated by asterisks (*), $p < 0.05$.

Lower expression of BCRP in HUVECs compared to MCF-7 cells is undoubtedly one of the factors determining the stronger photodynamic effect observed in these cells in the presence of HSA. However, other HSA-independent factors may also contribute to the higher susceptibility of the former cell line to Zn-Pheide-mediated PDT. To explain this, we examined the photodynamic effect induced with the use of a range of Zn-Pheide concentrations in both cell lines in the absence of HSA and plotted the dose–response curves (Figure 3). Different concentrations of the PS were applied to the cells in order to show the expected sigmoidal shape of the curves.
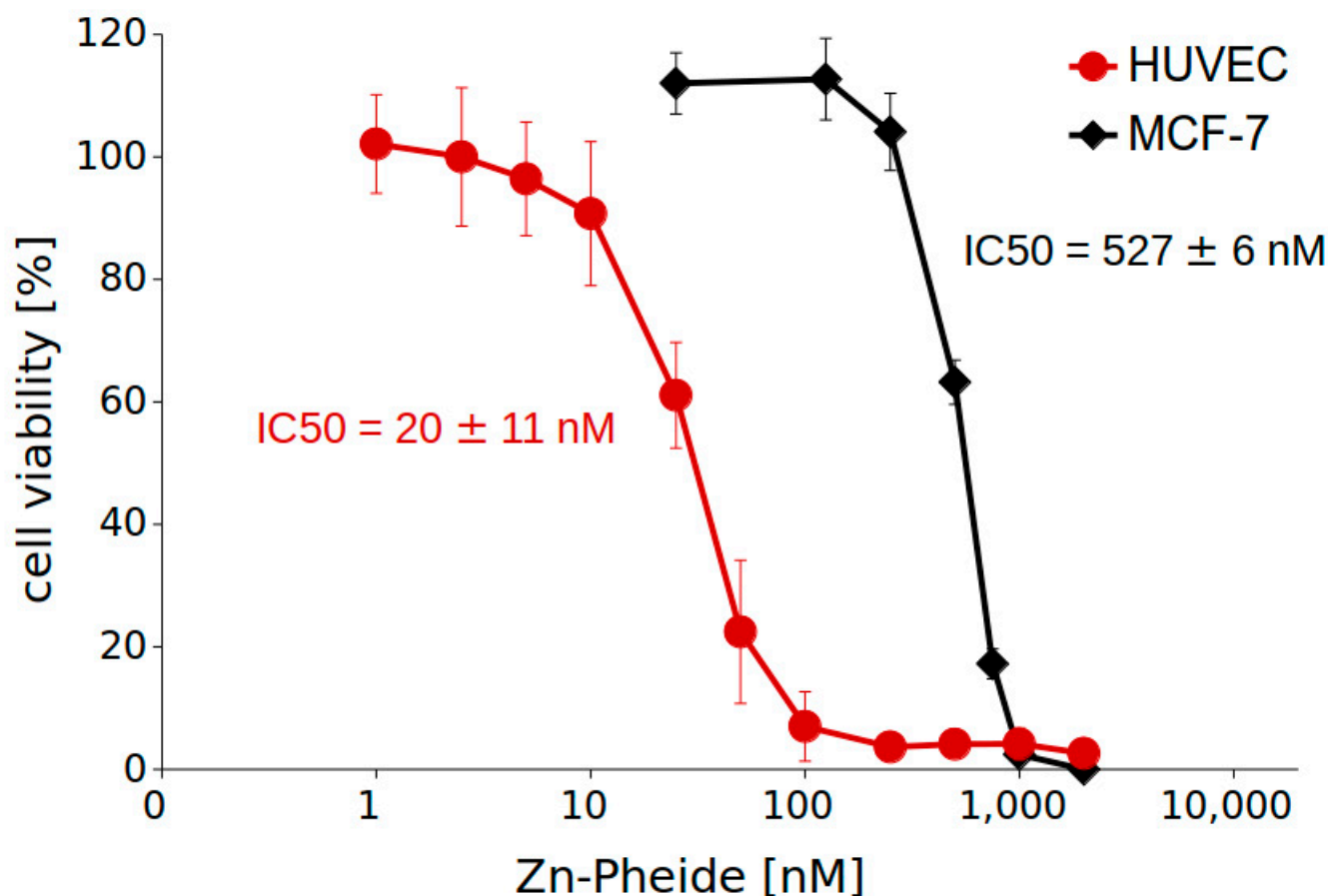
Figure 3. Dose–response curves of MCF-7 and HUVEC cells treated with Zn-Pheide (see the text for details). Cell viability was determined by MTT assay. The results are shown as mean ± SD, *n* = 3.

We found that HUVECs were much more susceptible to Zn-Pheide-induced PDT than MCF-7 cells, regardless of the PS complexation with HSA. The IC50 value was an order of magnitude lower for the former than for the latter cell line. Additionally, a higher slope was observed for MCF-7 than for HUVECs, showing that the cytotoxicity of Zn-Pheide towards the latter cell line increases relatively slowly with increasing concentration of the PS.

At high concentrations of HSA (250 μM), required for the complete binding of 1 μM Zn-Pheide, the uptake of the PS–HSA complex by the HUVEC cells might be difficult to identify, because at such conditions a significant fraction of gp60 will be occupied by free albumin. Therefore, we investigated the accumulation of Zn-Pheide in HUVECs at concentrations as low as 50 nM, and accordingly adjusted the concentrations of HSA, ranging from 10 nM to 12.5 μM. We observed that in the range of HSA concentrations from 0 to 1 μM, the accumulation of Zn-Pheide remained unchanged, while higher concentrations of the protein significantly reduced the PS level (Figure 4, grey bars). The photodynamic effect, in turn, increased with the increasing concentration of HSA, leading to a decrease in cell survival from 30% in the absence of HSA to 4% at 200 and 1000 nM of the protein, and

then gradually decreased (Figure 4, black dots). This shows that the HSA–PS complex is internalized into the cells and its absorption causes an increase in the photodynamic activity of Zn-Pheide, probably due to the alteration of its cellular localization. Unfortunately, direct visualization of the PS in caveolae was infeasible, since it required permeabilization of the cells, which in turn caused the PS release.
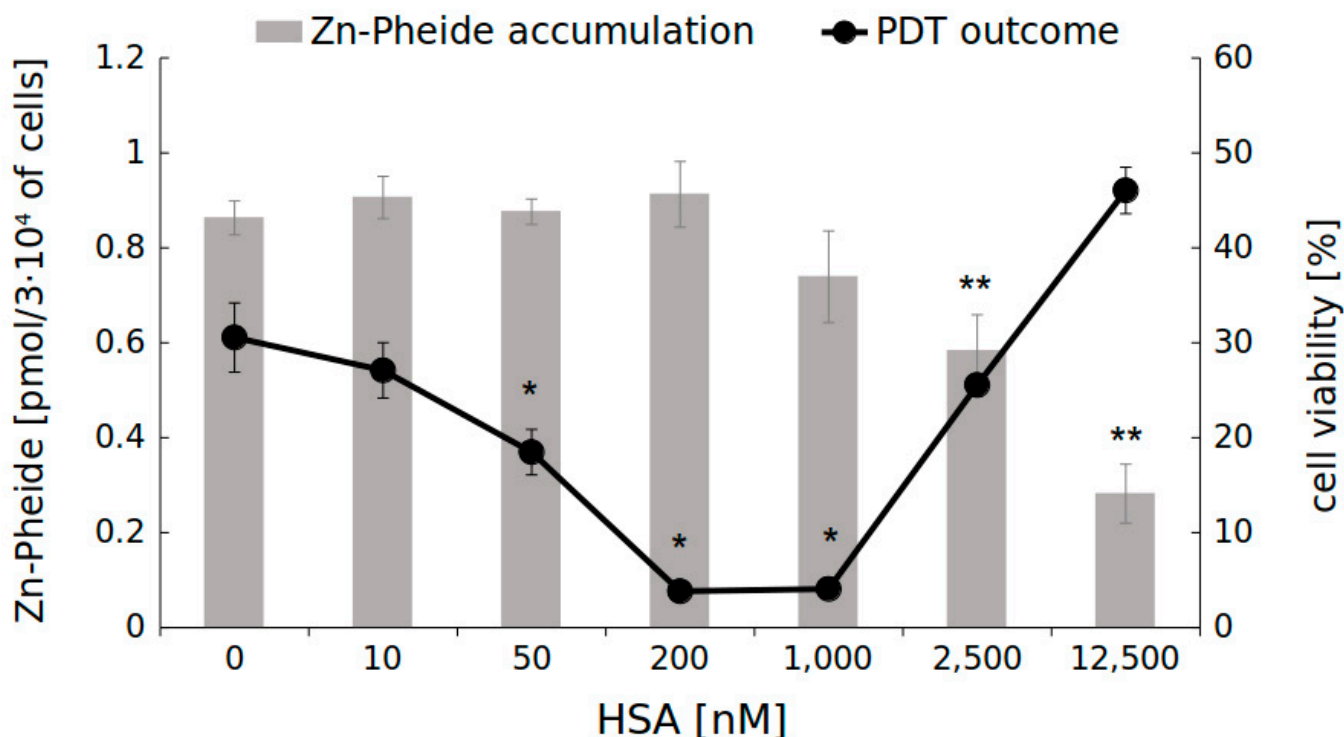

Figure 4. Accumulation of Zn-Pheide (50 nM) in HUVEC cells and the corresponding photodynamic effect at various concentrations of HSA. The results are presented as mean $\pm$ SD, $n = 3$. Single asterisks (*) indicate significant differences in cell viability compared to HSA-free cells ($p < 0.05$). Double asterisks (**) indicate significant differences in Zn-Pheide level compared to HSA-free cells ($p < 0.05$).

To evaluate the impact of HSA on the cellular localization of Zn-Pheide, we conducted a confocal microscopy study, the results of which are shown in Figures 5 and S2 (Supplementary Materials). We observed a statistically significant increase in the lysosomal localization of Zn-Pheide in the presence of HSA compared to HSA-free conditions, while the mitochondrial localization of the PS remained unchanged. It should be noted that the increase in the lysosomal localization of Zn-Pheide could probably be greater at lower concentrations of the PS and HSA than used in the microscopic experiment, because in this case a smaller fraction of gp60 would be occupied by free HSA. However, such an experiment was not feasible to perform, since the detection of the PS by confocal microscopy required sufficiently high concentrations. Interestingly, we observed that in the absence of HSA, the fluorescence emitted by Zn-Pheide inside the cells appeared almost uniformly distributed in the covered area, while in the presence of HSA it was in the form of dots of varying intensity. This effect causes a visual impression that the PS colocalization with mitochondria is enhanced by HSA (Figure 5A, right panel), which, as shown by correlation analysis (Figure S2), was not the case.
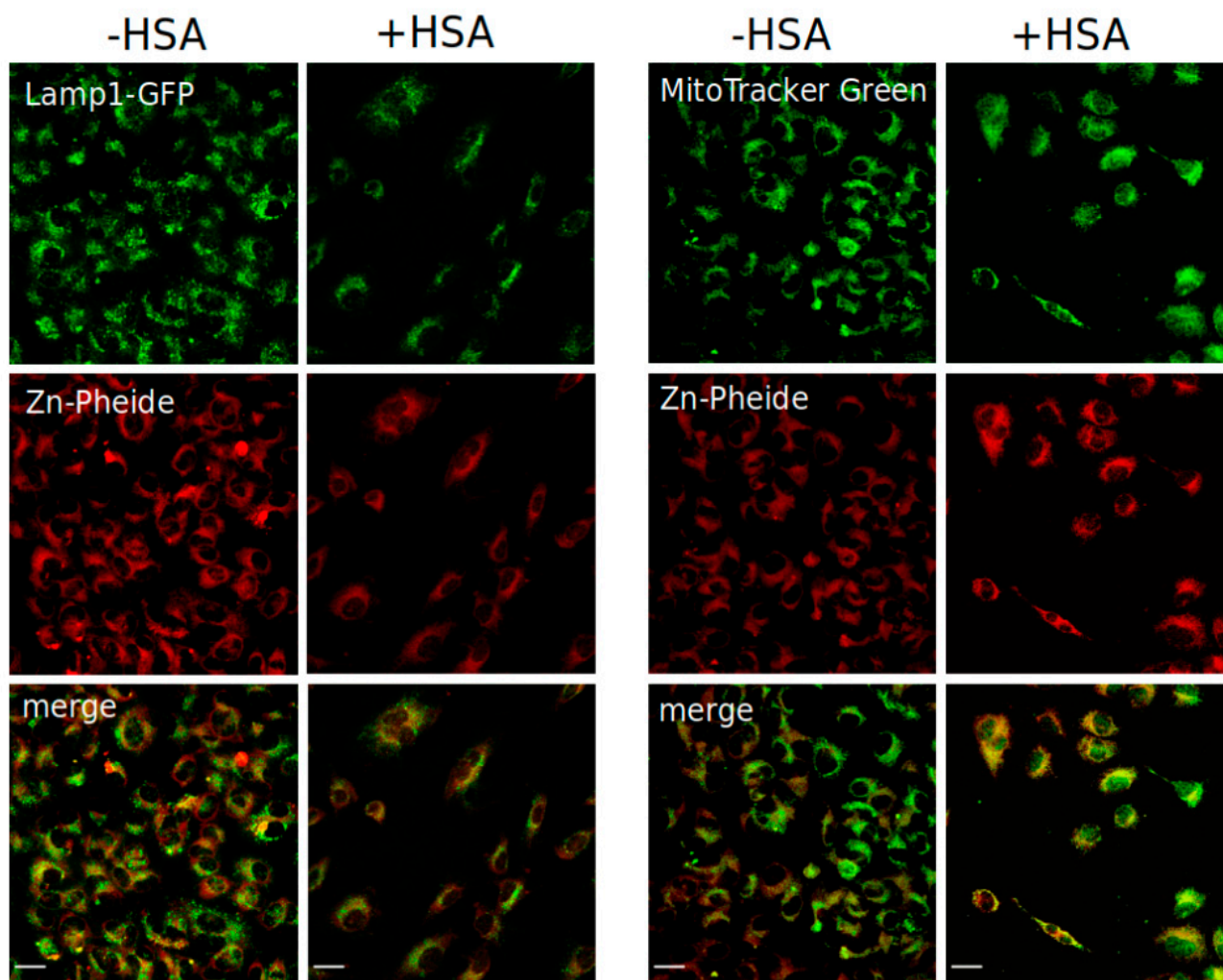
Figure 5. Colocalization analysis performed by confocal microscopy. The HUVEC cells stained with the CellLight™ Lysosomes-GFP, BacMam 2.0 reagent (fusion construct of Lamp1 and GFP) and Zn-Pheide (**left panel**), or with MitoTracker™ Green and Zn-Pheide (**right panel**), in the absence and presence of HSA. Maximum intensity projections of the representative 3D fluorescent images are shown. The scale bars represent 25 µm.

Once inside the endothelial cell, Zn-Pheide can leave it in two ways: either via BCRP, when it is in its free form, or by exocytosis, when it is either aggregated or complexed with albumin. Except for BCRP, probably no other transporter is involved in the efflux of free Zn-Pheide, as described in our previous paper [13]. At the same time, HUVEC cells cultured on plates are very imperfect models of the human endothelium, since they are unable to perform the transcytosis of albumin, which requires free space at both the luminal and abluminal sides of the cell [22]. Therefore, we conducted an experiment using HUVECs cultured on transwell inserts to enable the removal of the PS from both sides of the cells. After 3 h of incubation with the PS–HSA complex, the PS-containing medium was removed and replaced with fresh medium, either serum-free or supplemented with 2% fetal bovine serum. The cells were allowed for Zn-Pheide transport for the next 3 h and then illuminated, as described in the Materials and Methods section. The viability of cells that exported the PS to the serum-containing medium turned out to be significantly higher than that of the cells that were deprived of serum during the transport period (Figure 6). The presence of the BCRP inhibitor, quercetin, however, restored the cell susceptibility to PDT, decreasing their viability to the level only slightly higher compared to the FBS-free cells (Figure 6).
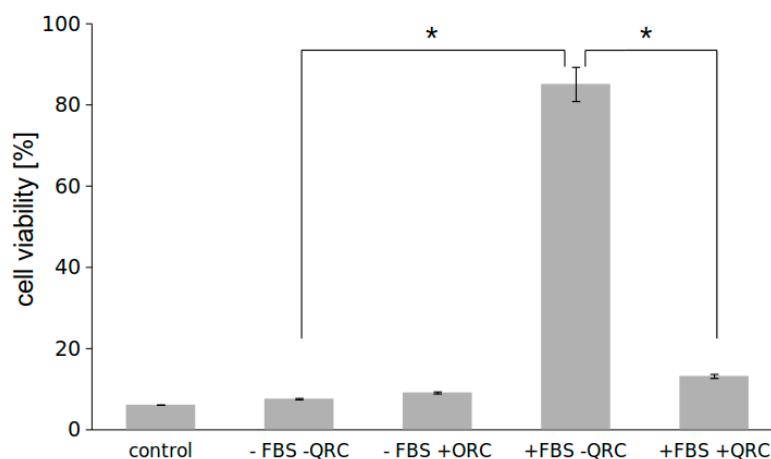
Figure 6. Viability (assessed by MTT assay) of HUVEC cells cultured on membrane inserts and allowed for the efflux of Zn-Pheide to either serum-depleted (-FBS) or serum-containing (+FBS) medium, in the presence or absence of quercetin (QRC). Cells that were not given time to remove the PS were indicated as control. Data are presented as mean ± SD from 3 inserts. Asterisks indicate significant differences between the groups, (*) indicates significant differences in cell viability between the groups, $p < 0.05$.

We compared the morphology of HUVEC cells subjected to PDT after the incubation with 1 μM Zn-Pheide in the presence and absence of 250 μM HSA. In the cells treated with the Zn-Pheide–HSA complex, we observed a characteristic apoptotic morphology, including cell shrinkage, loss of adhesion, and the formation of apoptotic bodies (Figure 7E). When HSA was absent, in turn, the characteristic features of necrosis were observed, such as the increase in cell volume and plasma membrane blebbing (Figure 8B). These features were observed as early as 30 min after the PDT. After longer periods following PDT, we observed a significant shrinkage and detachment of the cells treated with the Zn-Pheide–HSA complex, while the cells treated solely with Zn-Pheide attached firmly to the culture vessel and appeared swollen, with plasma membrane blebs (Figure 7C). Importantly, no difference was observed between the control cells incubated with the PS in the dark with and without HSA (Figure 7A,D).
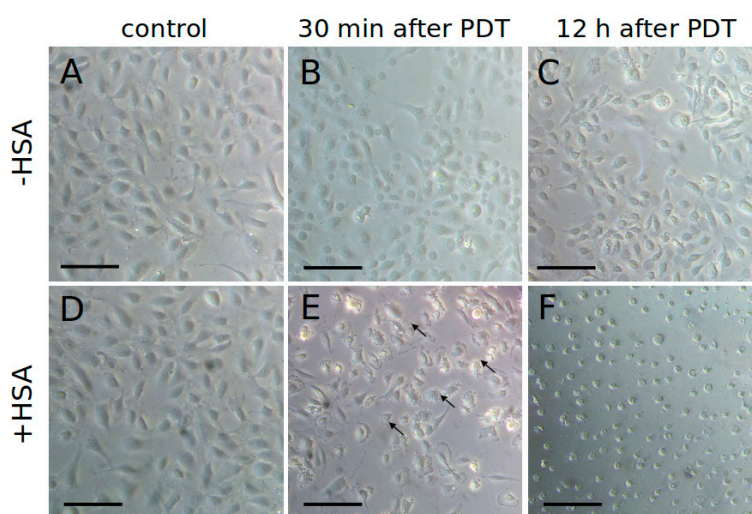

Figure 7. Morphology of HUVEC cells 30 min or 12 h after PDT. The cells accumulated Zn-Pheide (1 μM) in the absence (**A**–**C**) or presence (**D**–**F**) of HSA (250 μM). The control cells were incubated in the dark. The arrows indicate the apoptotic bodies formed after PDT performed in the presence of HSA. The scale bars represent 50 μm.

The observed differences in the morphology of PDT-subjected cells prompted us to confirm the type of cell death with additional methods: flow cytometric analysis with Annexin V/propidium iodide staining and confocal microscopy study after the staining of the nuclei with Hoechst 33342. In order to examine whether albumin has a direct effect on the type of cell death, or if its role is limited to the decrease of the PS absorption, in these experiments we included three groups of cells. The first group was incubated with 1 μM Zn-Pheide without HSA, the second with 100 nM Zn-Pheide also without HSA, and the third with 1 μM Zn-Pheide in the presence of 250 μM HSA. We chose the concentration of 100 nM, since it resulted in a similar intracellular level of Zn-Pheide, as in the case of the incubation performed with 1 μM Zn-Pheide in the presence of 250 μM HSA (data not shown). Additionally, the corresponding controls were prepared by the treatment of the cells with either HSA-free or HSA-containing culture medium with the appropriate concentration of DMSO. Since no visible differences were observed between these controls, we only present the results obtained for the cells incubated in the presence of HSA.

Staining with Hoechst revealed the shrinkage of nuclei (pyknosis) and chromatin condensation in the cells subjected to PDT after the incubation with 100 nM Zn-Pheide or 1 μM Zn-Pheide in the presence of HSA (Figure 8C,D). Counting the cells in which chromatin condensation was observed gave the same result of 66% apoptotic nuclei in both groups. Intranuclear chromatin condensation was widespread with a variable distribution. In some nuclei, clumps of chromatin were visible over their entire surface, while in others they were mostly adjacent to the nuclear membrane. These features were much less prominent in the cells treated with 1 μM Zn-Pheide (Figure 8B).
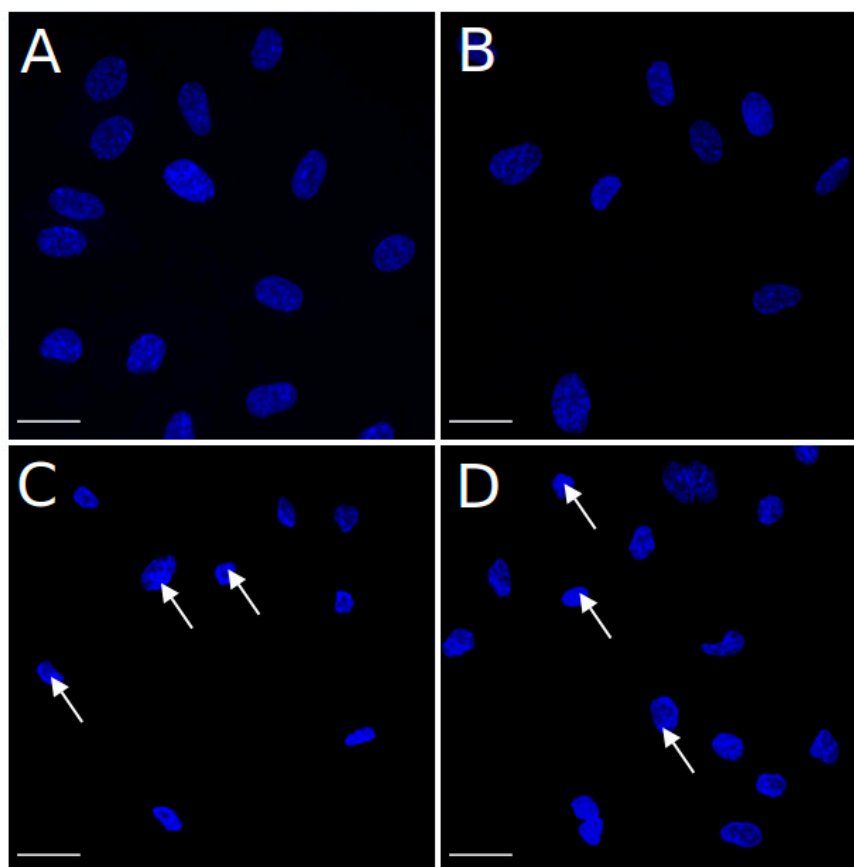

Figure 8. The HUVEC cells stained with Hoechst 33,342 to visualize the morphology of nuclei after PDT. (**A**) Control cells, (**B**) cells treated with 1 μM Zn-Pheide without HSA, (**C**) cells treated with 100 nM Zn-Pheide without HSA, and (**D**) cells treated with 1 μM in the presence of 250 μM HSA. The staining was performed 30 min after PDT. The arrows indicate the areas of condensed chromatin. The scale bars represent 25 μm.

The apoptotic/necrotic effect occurring as a consequence of the Zn-Pheide-induced PDT was further validated by cytometric analysis with Annexin V/propidium iodide double staining. Since, in the cytometric assay, similarly as in the nuclear staining assay, there was virtually no difference between the control samples prepared by incubating the cells in HSA-containing and HSA-free medium, we only present the result for the former control sample. In the group treated with 1 μM Zn-Pheide without serum, the majority of the cells were identified as late apoptotic/necrotic and very few living cells were present (Figure 9B). In contrast, among the cells treated with 100 nM Zn-Pheide or with the Zn-Pheide–HSA complex, a higher percentage of early apoptotic than late apoptotic/necrotic cells was observed (Figure 9C,D). Additionally, in the gate with low signal from both fluorophores, which is identified as living cells, the fluorescence of Annexin V is higher than in the control group. This suggests that these cells are likely to undergo apoptosis in a short period of time.
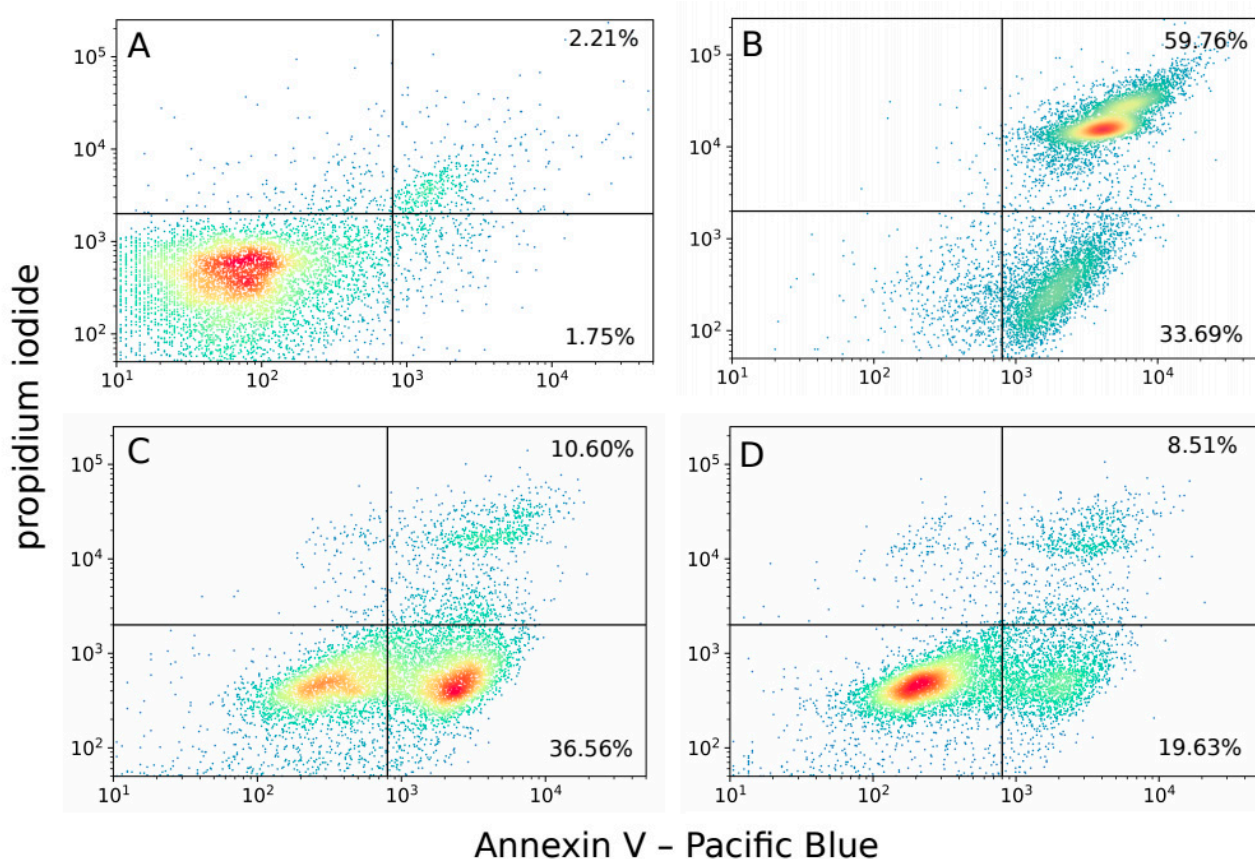

Figure 9. Flow cytometry analysis of HUVEC cells death mode after Zn-Pheide-induced PDT. The cells were stained with Pacific Blue-conjugated Annexin V and propidium iodide (PI), 30 min after irradiation. (**A**) Control cells, (**B**) cells treated with 1 μM Zn-Pheide without HSA, (**C**) cells treated with 100 nM Zn-Pheide without HSA, and (**D**) cells treated with 1 μM in the presence of 250 μM HSA. The percentage of cells undergoing early apoptosis (Annexin V—positive, PI—negative) and late apoptosis/necrosis (double-positive) is given.

Interestingly, a higher percentage of early apoptotic cells was observed in the group treated with 100 nM Zn-Pheide than with the Zn-Pheide–HSA complex (Figure 9C,D), suggesting that the process of apoptosis occurs more rapidly in the former group. We suspected that this effect might result from differential pro- and antiapoptotic gene expression between these groups. Therefore, the expression of *BAX*, *BCL2*, and *CASP3* genes at the mRNA level was analyzed in HUVECs after Zn-Pheide-induced PDT. Gene expression was assessed 30 min after PDT using quantitative real-time PCR. In the group of cells treated with 1 μM Zn-Pheide in the presence of HSA, we observed an increase in the expression of

BAX and *CASP3*, while the expression of *BCL2* remained unchanged (Figure 10). In contrast, the cells treated solely with 100 nM Zn-Pheide showed a decrease in expression of all three genes. Importantly, increased levels of *BAX* and *CASP3* mRNA were recorded in the control cells incubated in serum and the HSA-free medium, but not in the HSA-containing medium. This effect most likely results from the previously confirmed protective activity of albumin towards endothelial cells from apoptosis [23,24]. Importantly, in the cytometric study, we did not observe an increased number of apoptotic or necrotic cells in the HSA-free control compared to the HSA-containing control (data not shown). However, an increased expression of the *BAX* gene in the former may render these cells more susceptible to apoptosis, which consequently occurs more rapidly in the HSA-deprived cells than in the HSA-containing cells (Figure 9 C,D). This experiment shows that intracellular albumin has no effect on the PDT-induced expression of the analyzed genes, but pre-PDT serum starvation accelerates the induction of apoptosis.
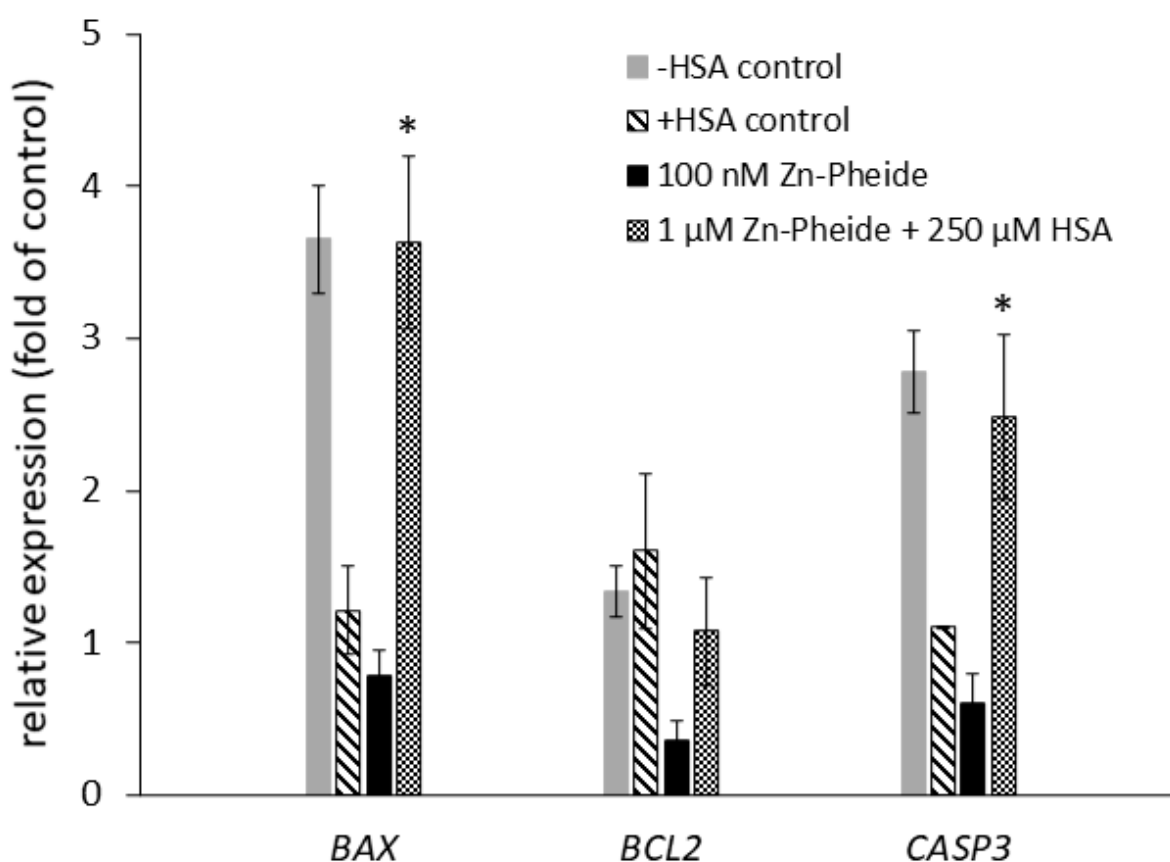

Figure 10. Relative quantification using real-time quantitative PCR of mRNA expression of *BAX*, *BCL2*, and *CASP3* genes in HUVEC cells upon Zn-Pheide-induced PDT. Data are shown as mean ± SD (*n* = 4). * *p* < 0.05 compared to HSA-containing control.

3. Discussion

In the present study, we investigated the photodynamic effect induced with Zn-Pheide against HUVEC cells, including the type of cell death, particularly in the context of the binding of this PS to HSA. We found that Zn-Pheide induces a dose-dependent photodynamic effect in HUVECs with an IC50 value close to 20 nM, which is about 25-fold lower than the corresponding value for MCF-7 cells. At nanomolar concentrations, Zn-Pheide induces the death of HUVECs by apoptosis. The concentration of Zn-Pheide equal to 100 nM, which induces apoptotic cell death, at the same time kills almost 100% of the cells. Therefore, it is possible that the conditions of PDT can be adjusted to induce the death of the majority of endothelial cells by apoptosis. For comparison, low concentrations of

Zn-Pheide (below 125 nM) had no effect on the viability of MCF-7 cells. In turn, increasing the concentration above this threshold leads to a rapid decrease in MCF-7 cell viability, which is observed as a steep dose–response curve. This difference in the susceptibility to Zn-Pheide-mediated PDT is interesting, particularly regarding that, in the case of a widely known photosensitizer, Photofrin, already approved for clinical use, equal sensitivity of endothelial and tumor cells to PDT was observed [25]. We hypothesize that the resistance of MCF-7 cells to Zn-Pheide-induced apoptosis may be, similarly as it is in the case of other treatment types, due to the lack of caspase-3 expression and a persistent PDT-induced cell cycle arrest in the phase G2 [26–28]. Caspase-3 is considered the most important effector caspase, responsible for the cleavage of several proteins and DNA fragmentation [29,30]. Although other caspases have been reported to function in lieu of the lack of caspase-3, the efficiency of this substitution varies for different treatment types [31,32]. It should be noted that the MCF-7 response to Zn-Pheide-mediated PDT is similar as those of other cancer cells [10]. This means that the high susceptibility to Zn-Pheide-mediated PDT in general distinguishes endothelial cells from cancer cells, and thus makes the first ones a good target for treatment. In light of the above, possibly the previously observed excellent therapeutic effects achieved with Zn-Pheide were due to the vascular shutdown effect rather than the direct killing of tumor cells [10,11].

Apart from the concentration of a PS, its cellular localization is also a factor determining the type of PDT-induced cell death mode. It has been shown that PSs accumulating in mitochondria induce a faster apoptotic effect than those localized in lysosomes or cell membranes [33,34]. Possibly, this can also be the reason for a fast apoptosis observed in the HUVECs. Previous studies on the cellular localization of Zn-Pheide showed that, in cancer cells, it does not colocalize with mitochondria, whereas in the HUVECs, its mitochondrial localization, though relatively low, was observed [10].

We found that HSA-bound Zn-Pheide enters HUVEC cells, which promotes its lysosomal localization, thereby increasing its photodynamic activity. The protein component of the complex is most likely degraded in lysosomes, whereas free Zn-Pheide can be transported outside the cell as long as free albumin is present in the environment. The HSA–Zn-Pheide complex can be internalized into the cells via the gp60 receptor (albondin), but possibly also other receptors present on endothelial cells, such as gp18 or gp30. The latter two receptors are believed to be scavenger receptors, which bind modified albumin molecules and direct it for degradation [35]. Since HSA undergoes slight conformational changes upon Zn-Pheide binding, it seems likely that these receptors are involved in its internalization, after which the protein component of the complex is degraded in lysosomes [14]. On the other hand, however, since the uptake of Zn-Pheide significantly decreases at high concentrations of HSA, the involvement of gp60 cannot be excluded. It is also important to note that, even at the saturating concentration of HSA, Zn-Pheide is likely to enter the cells in its free form, which occurs transiently within the equilibrium of its binding to HSA. It should be noted that the effect induced by Zn-Pheide in cancer patients will be probably strictly dependent on their serum albumin level. In hypoalbuminemia, which is a condition commonly encountered in patient with solid tumors, the cellular level of Zn-Pheide may be higher, and thus the photodynamic effect stronger, possibly leading to necrosis rather than apoptosis of endothelium [36,37].

In the transport-PDT study using HUVECs cultured on membrane inserts, a significant difference in viability was observed between the cells transporting Zn-Pheide to the serum-free and serum-containing medium. This allows to conclude on the way of the PS removal from the cells. There is no reason to assume that the transcytosis of albumin requires the presence of serum in the abluminal space. At the same time, the transport of Zn-Pheide was significantly accelerated by serum. This suggests that Zn-Pheide is effluxed from the cells predominantly in its free form, via BCRP, since this type of transport is accelerated in the presence of serum/albumin [13]. Thus, Zn-Pheide present inside HUVECs is probably predominantly in its free form. This can be an effect of HSA degradation in lysosomes, as

well as the uptake of the PS in its free form, which occurs transiently within the equilibrium of its binding to albumin.

Zinc pheophorbide a is structurally similar to another PS, palladium bacteriopheophorbide (Pd-BPheide, WST09), known under its trade name TOOKAD®. Palladium bacteriopheophorbide is a derivative of bacteriochlorophyll a, isolated from the photosynthetic bacteria *Rhodovolum sulfidophilum* [38]. TOOKAD®, together with its water soluble derivative, padeliporfin (WST11, TOOKAD® Soluble), are now approved in Europe and Israel for the VTP of low-risk prostate cancer [5]. TOOKAD® has a strong light absorption ($\varepsilon \sim 10^5$ M^{-1} cm^{-1}) in the near infrared region (λ = 763 nm), lying in the so-called therapeutic window of human tissue. In comparison, Zn-Pheide shows a similar absorption in its Q_y band, which is, however, localized at shorter wavelengths ($\lambda_{max} \sim 670$ nm) [9]. This gives Pd-BPheide a slight advantage over Zn-Pheide, since the light of higher wavelengths penetrates deeper into tissues [39]. TOOKAD® is cleared from the circulation within hours and its soluble derivative within minutes [40,41]. The rapid clearance of these PSs can be considered an advantage in terms of patient safety; however, their retention time might be too short to perform several irradiations upon a single PS injection, which is possible with Zn-Pheide (mean $t_{1/2}$ = 44 h) [42].

The quantum yield of singlet oxygen generation (Φ_Δ) by TOOKAD® has been shown to reach 1 in organic solvents and 0.5 in TX-100 micelles. The aqueous environment, in turn, significantly reduced its singlet oxygen yield, instead promoting the generation of superoxide and hydroxyl radicals [43]. TOOKAD® Soluble in water did not generate even traces of singlet oxygen [44]. In comparison, Φ_Δ of Zn-Pheide was equal to 0.49 in ethanol, 0.54 in F-127 micelles, 0.39 in DPPC, and 0.13 in water [45]. Superoxide anion generated by Zn-Pheide was also detected in water containing 5% of DMSO [46]. Similar values of Φ_Δ in micelles suggest that both PSs will be equally efficient in the generation of singlet oxygen in biological membranes. In the cytoplasm (water), in turn, TOOKAD® will act almost solely via the type I reaction, and Zn-Pheide via both type I and type II.

Solubility in water, expressed by the octanol/water partition coefficient, is similar for TOOKAD® (24) and Zn-Pheide (32) [38,41]. The former, however, is believed to require a nonionic surfactant, Cremophor, at the stage of administration, while the latter was administered to animals both with and without Cremophor, giving satisfactory treatment results in both cases [11]. This could result from a higher affinity of Zn-Pheide to serum proteins, and possibly also lipoproteins, which promotes its disaggregation and at the same time increases its retention time.

Although the exchange of the Mg ion for the Zn ion increases the stability of chlorophylls, Zn-Pheide shows a relatively high yield of photobleaching in water (0.55). This value is significantly decreased in ethanol (0.01) [45]. In comparison, the photobleaching of TOOKAD® was also observed in methanol and acetone [47]. Complexation with albumin is likely to increase the photostability of both PSs, as was similarly observed for hematoporphyrin [48]. Moreover, since Zn-Pheide has a stronger bind to albumin than Pd-BPheide, the complexation of the former may increase its stability to a greater extent. This hypothesis, however, requires experimental confirmation.

Both Pd-BPheide and Zn-Pheide can be monitored in vivo for their proper dosimetry [11,49]. In the case of the former, it is, however, more difficult due to the very weak fluorescence and the low affinity to albumin, since the fluorescent signal from the albumin-bound PS is enhanced, as we showed for Zn-Pheide [14]. An additional factor that hinders the monitoring of TOOKAD® is its very short retention time, which, in the case of Zn-Pheide, is much longer [42].

To the best of our knowledge, the interaction of WST09 and WST11 with BCRP has not been analyzed. Since these PSs are derived from a natural compound of a tetrapyrrole structure (bacteriochlorin), they are possibly ABCG2 substrates. However, as long as this hypothesis is not confirmed, the BCRP inhibitors cannot be used to prolong their retention time in tissues.

Experiments similar to those performed in the present study were conducted for WST11 with the usage of the murine endothelial cell line H5V. The LC50 value of WST11 determined in the absence of serum at the 2 h incubation time and the light dose of 12 J/cm^2 was as high as 1 μM [41]. In comparison, the LC50 value of Zn-Pheide against HUVECs was only 20 nM at 3 h accumulation time and the light dose of 2 J/cm^2.

It has been shown that WST11, similarly to Zn-Pheide, is partially incorporated into the cells via receptor-dependent endocytosis. However, given that the association constant of WST11 to albumin ($K_a \sim 10^4$ M^{-1}) is two orders of magnitude lower than the corresponding value for Zn-Pheide, the role of albumin in trafficking the PS into the endothelium is probably more significant for the latter. Similarly, as in the case of Zn-Pheide, both the serum and the pure albumin accelerated the removal of WST11 from the cells. This indicates that WST11 leaves the cells in its free form, possibly via BCRP [13,41].

A drawback of bacteriochlorophyllide-based PSs is their high production cost [50]. This does not apply to Zn-Pheide, which is produced from chlorophyll a, available in virtually unlimited quantities, and which does not require complex chemical modifications [10].

In summary, since the applicability of a PS for therapy is determined by a number of features, it is difficult to state unequivocally whether Zn-Pheide is superior to TOOKAD® in terms of its application in VTP. Undoubtedly, however, it possesses several characteristics that make it a noteworthy candidate for a potential use in both the vascular-targeted treatment of solid tumors, as well as a range of vascular abnormalities.

4. Materials and Methods

4.1. Photosensitizer

Zinc pheophorbide a (Zn-Pheide) was obtained from pheophorbide a (Cayman Chemical, Ann Arbor, MI, USA) via direct metalation with zinc acetate in methanol at 50 °C and purified, as described earlier [10]. Purity of the compound according to HPLC measurement was at least 96%. The concentration of Zn-Pheide was determined spectrophotometrically in ethanol, using the extinction coefficients at the Q_y band equal to 71,500 M^{-1} cm^{-1}. Aliquots of the PS were stored dry at −20 °C under nitrogen atmosphere. For each experiment, fresh solutions of the PS were prepared by dissolving them in appropriate volumes of DMSO. All experiments were performed under dim light to avoid degradation of the PS and uncontrolled photodamage of the cells.

Complex of the PS with HSA was prepared by addition of the PS stock solution in DMSO to solution of albumin in PBS, pH 7.4, and incubation at room temperature for 10 min to reach the binding equilibrium.

4.2. Cell Lines

Human umbilical vein endothelial cells (HUVECs) pooled from multiple donors were obtained from PromoCell (Heidelberg, Germany). The cells were cultured in the endothelial cell growth medium (ECM, PromoCell, Heidelberg, Germany) supplemented with 2% fetal bovine serum (FBS), 4 μL/mL endothelial cell growth supplement, 0.1 ng/mL epidermal growth factor, 1 ng/mL basic fibroblast growth factor, 90 μg/mL heparin, and 1 μg/mL hydrocortisone. The human breast carcinoma cell line MCF-7 was obtained from the American Type Culture Collection (ATCC, Manassas, VA, USA). The cells were maintained in Dulbecco's modified Eagle's medium (DMEM, Thermo Fisher Scientific, Waltham, MA, USA) supplemented with 10% (*v/v*) FBS, 2 mM glutamine, 1 mM sodium pyruvate, penicillin (100 units/mL), and streptomycin (100 μg/mL). Both cell lines were cultured at 37 °C in a humidified atmosphere of 5% CO_2.

4.3. Photodynamic Treatment and Cell Viability Assays

Cytotoxicity of Zn-Pheide, both in the dark and after irradiation, was determined by MTT assay. For cytotoxicity studies, 3×10^4 cells were seeded onto 96-well plates. After an overnight growth, the cells were incubated in the dark for 3 h with Zn-Pheide at various concentrations. Control cells were incubated with the appropriate concentration

of DMSO (below 0.5%) without the PS. For PDT, the cells were rinsed with PBS, covered with HBSS, and illuminated with 2 J/cm^2 delivered by a LED illuminator equipped with a 600 nm cut-off filter. After that, they were covered with complete culture medium and incubated for another 24 h. Then, 0.5 mg/mL MTT (3-(4,5-dimethylthiazol-2-yl)-2,5-diphenyltetrazolium bromide), (Carl Roth, Karlsruhe, Germany) was added to each well, and the cells were incubated for another 3 h. The precipitated formazan crystals were dissolved in an ethanol/DMSO mixture (*v/v*, 1:1) and the absorbance of the solutions at 570 nm was measured using a SpectraMax i3 plate reader (Molecular Devices, San Jose, CA, USA). The signal from the treated cells was compared to that of the vehicle-only control cells (100%) to calculate the percentage viability. All experiments were performed in triplicates. Dose–response curves were fitted and IC50 values determined in Origin 2021 [51].

4.4. Cellular Localization of Zn-Pheide

Cellular localization of Zn-Pheide in HUVEC cells in the presence or absence of HSA was assessed by confocal microscopy using single organelle staining. Lysosomes were labelled using CellLight™ Lysosomes-GFP, BacMam 2.0 reagent (Thermo Fisher Scientific, Waltham, MA, USA) according to the manufacturer's protocol. Then, the cells were incubated with either 0.5 μM Zn-Pheide alone for 2 h or with 1 μM Zn-Pheide and 250 μM HSA overnight. After removal of the PS, mitochondria were stained with 100 nM Mito-Tracker™ Green (Thermo Fisher Scientific, Waltham, MA, USA) for 45 min. Then, the cells were washed with PBS and fixed with 4% paraformaldehyde in PBS at room temperature for 10 min. Confocal images were collected using an upright confocal microscope Leica SP8. Stacks of confocal 12-bit images with a voxel size of 0.186 × 0.186 × 0.999 μm were acquired using oil 40× objective (HC PL APO CS2 40×/1.3 OIL). The organelle markers were excited with laser 488 nm, while the Zn-Pheide was excited with laser 647 nm. The emission was collected in the range 495–590 nm for the organelle markers, and 643–730 nm for Zn-Pheide. The acquisition was performed in sequential mode. Colocalization analysis was performed using the JACoP plugin tool in Fiji ImageJ to calculate the Pearson's correlation coefficients [52,53].

4.5. Efflux Assay

The HUVECs were seeded onto PET ThinCert® cell culture inserts with 0.4 μm pores (Greiner Bio-One, Kremsmünster, Austria, cat. no. 665640) at a density of 10^5 of cells per insert and left for attachment. Next day, Zn-Pheide at a concentration of 1 μM in the presence of 250 μM HSA was applied to both top and bottom chambers. After 3 h of incubation, the PS-containing medium was replaced with either serum-free or complete ECM medium (containing 2% FBS) in both chambers. The cells were incubated for the next 3 h for the PS efflux and then irradiated with 2 J/cm^2 of red light. Control (100% viability) cells were prepared by incubation of the cells without Zn-Pheide and with or without serum, respectively. Additional control, for assessment of the PS efflux rate, was prepared by illuminating the cells right after the incubation with PS-HSA complex, without the transport period. The experiments were performed in triplicates and in the presence or absence of BCRP inhibitor, quercetin, at a concentration of 100 μM. The viability of the cells was examined by MTT assay 24 h after the PDT.

4.6. Hoechst Staining Assay

The HUVEC cells were seeded onto 10 mm glass slides (approximately 2.5 × 10^4 cells per well) and cultured overnight. Photodynamic treatment was performed after 3 h of cell treatment either with sole 1 μM and 100 nM Zn-Pheide in serum-free culture medium or 1 μM Zn-Pheide in the presence of 250 μM HSA. Control cells were incubated in serum-free ECM medium, with or without 250 μM HSA, containing an appropriate concentration of DMSO. Thirty minutes after the PDT, the cells were fixed with 4% paraformaldehyde for 10 min at room temperature, washed twice with PBS, and stained with 5 μg/mL Hoechst 33,342 for 10 min at room temperature. Then, they were washed again, mounted onto

microscope slides, and imaged using an inverted confocal microscope Zeiss Cell Observer. Stacks of confocal 16-bit images with a voxel size of $0.167 \times 0.167 \times 0.24$ μm were acquired using oil $40\times$ objective (Plan Apochromat $40\times/1.4$ OIL DIC (UV) Vis-IR M27), exposure time 100 ms, and depth of focus 0.72 μm. Hoechst 33,342 was excited with laser 405 nm. The emission was collected using filters: RQFT 405/488/568/647 and BP 450/50 nm. ImageJ (Fiji) was used for image analysis [52].

4.7. Analysis of Cell Death Mode by Flow Cytometry

The HUVEC cells were seeded onto a 6-well plate (2.5×10^5 cells per well) and cultured overnight. Next day, PDT was performed after 3 h of cell treatment with either sole 1 μM and 100 nM Zn-Pheide in serum-free culture medium or 1 μM Zn-Pheide in the presence of 250 μM HSA. Control cells were incubated in serum-free ECM medium, with or without 250 HSA, containing an appropriate concentration of DMSO. Heat-treated cells (55 °C for 20 min) served as a positive control. Thirty minutes after the PDT, the cells were harvested by trypsinization, washed with PBS, and suspended in Annexin V-binding buffer (10 mM HEPES pH 7.4, 140 mM NaCl, 2.5 mM CaCl$_2$) at a density of 10^6 cells/mL. The cells were stained with Annexin V, Pacific Blue™ conjugate (Thermo Fisher Scientific) and propidium iodide (BD Biosciences, Franklin Lakes, NJ, USA) for 15 min at room temperature. Then, after 5-fold dilution with Annexin V-binding buffer, the cells were analyzed using a BD FACSCanto II flow cytometer. Data were processed using the BD FACSDiva 8.0.1 and FlowCal software [54].

4.8. Quantitative Real-Time PCR

For the analysis of pro- and antiapoptotic genes expression in PDT-subjected cells, HUVECs were seeded on a 6-well plate (3×10^5 cells per well) and cultured overnight. Next day, the cells were treated with either 100 nM Zn-Pheide in serum-free medium or with 1 μM Zn-Pheide in the presence of 250 μM HSA, for 3 h. Control cells were incubated in serum-free ECM medium, with or without 250 μM HSA, containing an appropriate concentration of DMSO (below 0.5%). Then, the cells were irradiated as described earlier. Thirty minutes after the PDT, total RNA was isolated from the cells using the GeneMATRIX Universal RNA kit (EURx, Gdańsk, Poland). The RNA concentration was measured using a NanoDrop 8000 spectrophotometer (Thermo Fisher Scientific). Reverse transcription was performed using the NG dART RT kit (EURx, Gdańsk, Poland) with oligo(dT) primer. Quantitative real time PCR was performed using the iProof™ High-Fidelity DNA Polymerase (Bio-Rad, Hercules, CA, USA), together with SYBR Green dye (Sigma-Aldrich, St. Louis, MO, USA) and the primers listed in Table 1. The analysis was performed using a Rotor Gene Q thermocycler (Qiagen, Hilden, Germany). The relative fold change in the mRNA expression of the target gene was quantified using the $2^{-\Delta\Delta Ct}$ method. Glyceraldehyde 3-phosphate dehydrogenase (GAPDH) was used as a housekeeping gene. Nontreated cells were used as a calibrator for quantification.

Table 1. Primers used for quantitative real-time PCR.

Gene	Forward Primer Sequence (5′→3′)	Reverse Primer Sequence (5′→3′)
BAX	AGTGGCAGCTGACATGTTTT	GGAGGAAGTCCAATGTCCAG
BCL2	GCCCTGTGGATGACTGAGTA	GGCCGTACAGTTCCACAAAG
CASP3	TGTGAGGCGGTTGTGGAAGAGT	AATGGGGGAAGAGGCAGGTGCA
GAPDH	CGGAGTCAACGGATTTGGTCGTAT	AGCCTTCTCCATGGTGGTGAAGAC

For the determination of ABCG2 expression at the mRNA level, total RNA was isolated from untreated MCF-7 and HUVEC cells and reverse transcription was performed as described above. Quantitative real-time PCR was performed using human ABCG2-specific TaqMan® system (Thermo Fisher Scientific). The expression was determined by the absolute quantification using a standard curve generated on the basis of an ABCG2 gene containing plasmid construct.

4.9. Statistical Analysis

To assess statistical significance of differences between two sets of data, the two-sided unpaired Student's *t*-test was conducted in Origin 2021. The *p*-values < 0.05 were considered statistically significant as indicated by asterisks.

5. Conclusions

In the present study, the in vitro effects of Zn-Pheide-based PDT on human umbilical vein endothelial cells (HUVECs) were determined through viability and cell death mode assays. We compared HUVECs with MCF-7 cells in terms of their susceptibility to Zn-Pheide-induced PDT, showing that the 50% inhibitory concentration (IC50) is roughly 25 times lower for the former line. We have also shown that nanomolar concentrations of Zn-Pheide combined with low doses of light effectively kill HUVECs by apoptosis, whereas concentrations as low as 1 μM induce their death primarily by necrosis. Additionally, we found that albumin-complexed Zn-Pheide enters HUVECs and increases the efficacy of PDT, probably by directing the PS to lysosomes. Based on photodynamic experiments performed with the use of culture inserts, we also showed that albumin complexed with Zn-Pheide is apparently degraded in HUVECs, whereas free Zn-Pheide can leave the cells via BCRP-mediated transport.

Additionally, we compared Zn-Pheide with a clinically approved photosensitizer, TOOKAD®, in terms of their photophysical and pharmacokinetic properties, showing that the former may serve as a valuable alternative to the latter.

The results obtained contribute to a better understanding of the mechanism of action of Zn-Pheide and demonstrate that it is a promising PS for the VTP of solid tumors and possibly a range of vascular anomalies.

Supplementary Materials: The following supporting information can be downloaded at: https://www.mdpi.com/article/10.3390/ph15020235/s1, Figure S1. Dark cytotoxicity of Zn-Pheide against MCF-7 and HUVEC cells in the absence of albumin; Figure S2. Correlation analysis of Zn-Pheide colocalization in lysosomes and mitochondria in the absence and presence of HSA; Figure S3. Absorption and emission spectra of Zn-Pheide recorded in ethanol; Figure S4. Positive controls included in the experiments.

References

1. Juarranz, Á.; Jaén, P.; Sanz-Rodríguez, F.; Cuevas, J.; González, S. Photodynamic therapy of cancer. Basic principles and applications. *Clin. Transl. Oncol.* **2008**, *10*, 148–154. [CrossRef] [PubMed]
2. Dougherty, T.J. An Update on Photodynamic Therapy Applications. *J. Clin. Laser Med. Surg.* **2002**, *20*, 3–7. [CrossRef] [PubMed]
3. Mashayekhi, V.; Op't Hoog, C.; Oliveira, S. Vascular targeted photodynamic therapy: A review of the efforts towards molecular targeting of tumor vasculature. *J. Porphyr. Phtalocyanines* **2019**, *23*, 1229–1240. [CrossRef] [PubMed]
4. Ezleen, E.; Benachour, H.; Barberi-Heyob, M.; Frochot, C.A.H.; Guillemin, F.; Vanderesse, R. Vascular-Targeted Photodynamic Therapy (VTP). *Adv. Cancer Ther.* **2011**, *10*, 681–688. [CrossRef]
5. Azzouzi, A.R.; Barret, E.; Moore, C.M.; Villers, A.; Allen, C.; Scherz, A.; Muir, G.; De Wildt, M.; Barber, N.J.; Lebdai, S.; et al. TOOKAD® Soluble vascular-targeted photodynamic (VTP) therapy: Determination of optimal treatment conditions and assessment of effects in patients with localised prostate cancer. *BJU Int.* **2013**, *112*, 766–774. [CrossRef]

6. Mellish, K.J.; Brown, S.B. Verteporfin: A milestone in opthalmology and photodynamic therapy. *Expert Opin. Pharmacother.* **2001**, *2*, 351–361. [CrossRef]

7. Olivo, M.; Lucky, R.B.S.S.; Dendukuri, N.; Thong, P.S.-P. Targeted Therapy of Cancer Using Photodynamic Therapy in Combination with Multi-faceted Anti-Tumor Modalities. *Pharmaceuticals* **2010**, *3*, 1507–1529. [CrossRef]

8. Gerola, A.P.; Tsubone, T.M.; Santana, A.; De Oliveira, H.P.M.; Hioka, N.; Caetano, W. Properties of chlorophyll and derivatives in homogeneous and microheterogeneous systems. *J. Phys. Chem. B* **2011**, *115*, 7364–7373. [CrossRef]

9. Gerola, A.P.; Semensato, J.; Pellosi, D.S.; Batistela, V.R.; Rabello, B.R.; Hioka, N.; Caetano, W. Chemical determination of singlet oxygen from photosensitizers illuminated with LED: New calculation methodology considering the influence of photobleaching. *J. Photochem. Photobiol. A Chem.* **2012**, *232*, 14–21. [CrossRef]

10. Jakubowska, M.; Szczygieł, M.; Michalczyk-Wetula, D.; Susz, A.; Stochel, G.; Elas, M.; Fiedor, L.; Urbanska, K. Zinc-pheophorbide a-Highly efficient low-cost photosensitizer against human adenocarcinoma in cellular and animal models. *Photodiagn. Photodyn. Ther.* **2013**, *10*, 266–277. [CrossRef]

11. Szczygieł, M.; Boroń, B.; Szczygieł, D.; Szafraniec, M.; Susz, A.; Matuszak, Z.; Urbańska, K.; Fiedor, L. Real-time Non-invasive Transdermal Monitoring of Photosensitizer Level in vivo for Pharmacokinetic Studies and Optimization of Photodynamic Therapy Protocol. *J. Anal. Bioanal. Technol.* **2014**, *5*. [CrossRef]

12. Gerola, A.P.; Costa, P.F.A.; de Morais, F.A.P.; Tsubone, T.M.; Caleare, A.O.; Nakamura, C.V.; Brunaldi, K.; Caetano, W.; Kimura, E.; Hioka, N. Liposome and polymeric micelle-based delivery systems for chlorophylls: Photodamage effects on Staphylococcus aureus. *Colloids Surf. B Biointerfaces* **2019**, *177*, 487–495. [CrossRef] [PubMed]

13. Szafraniec, M.J.; Fiedor, L. One ring is not enough to rule them all. Albumin-dependent ABCG2-mediated transport of chlorophyll-derived photosensitizers. *Eur. J. Pharm. Sci.* **2021**, *167*, 106001. [CrossRef] [PubMed]

14. Szafraniec, M.J. Interactions of chlorophyll-derived photosensitizers with human serum albumin are determined by the central metal ion. *J. Biomol. Struct. Dyn.* **2021**. [CrossRef]

15. Vogel, S.M.; Minshall, R.D.; Pilipović, M.; Tiruppathi, C.; Malik, A.B. Albumin uptake and transcytosis in endothelial cells in vivo induced by albumin-binding protein. *Am. J. Physiol.-Lung Cell. Mol. Physiol.* **2001**, *281*, L1512–L1522. [CrossRef]

16. Miele, E.; Spinelli, G.P.; Miele, E.; Tomao, F.; Tomao, S. Albumin-bound formulation of paclitaxel (Abraxane® ABI-007) in the treatment of breast cancer. *Int. J. Nanomed.* **2009**, *4*, 99–105. [CrossRef]

17. Chatterjee, M.; Ben-Josef, E.; Robb, R.; Vedaie, M.; Seum, S.; Thirumoorthy, K.; Palanichamy, K.; Harbrecht, M.; Chakravarti, A.; Williams, T.M. Caveolae-mediated endocytosis is critical for albumin cellular uptake and response to albumin-bound chemotherapy. *Cancer Res.* **2017**, *77*, 5925–5937. [CrossRef]

18. Taverna, M.; Marie, A.-L.; Mira, J.-P.; Guidet, B. Specific antioxidant properties of human serum albumin. *Ann. Intensive Care* **2013**, *3*, 4. [CrossRef]

19. Jerjes, W.; Upile, T.; Hamdoon, Z.; Mosse, C.A.; Akram, S.; Morley, S.; Hopper, C. Interstitial PDT for vascular anomalies. *Lasers Surg. Med.* **2011**, *43*, 357–365. [CrossRef]

20. Zhang, Q.; Li, Z.H.; Li, Y.Y.; Shi, S.J.; Zhou, S.W.; Fu, Y.Y.; Zhang, Q.; Yang, X.; Fu, R.Q.; Lu, L.C. Hypericin-photodynamic therapy induces human umbilical vein endothelial cell apoptosis. *Sci. Rep.* **2015**, *5*, 18398. [CrossRef]

21. Tiruppathi, C.; Finnegan, A.; Malik, A.B. Isolation and characterization of a cell surface albumin-binding protein from vascular endothelial cells. *Proc. Natl. Acad. Sci. USA* **1996**, *93*, 250–254. [CrossRef] [PubMed]

22. Chanthick, C.; Kanlaya, R.; Kiatbumrung, R.; Pattanakitsakul, S.N.; Thongboonkerd, V. Caveolae-mediated albumin transcytosis is enhanced in dengue-infected human endothelial cells: A model of vascular leakage in dengue hemorrhagic fever. *Sci. Rep.* **2016**, *6*, 31855. [CrossRef] [PubMed]

23. Zoellner, H.; Höfler, M.; Beckmann, R.; Hufnagl, P.; Vanyek, E.; Bielek, E.; Wojta, J.; Fabry, A.; Lockie, S.; Binder, B.R. Serum albumin is a specific inhibitor of apoptosis in human endothelial cells. *J. Cell Sci.* **1996**, *109*, 2571–2580. [CrossRef] [PubMed]

24. Russell, F.D.; Hamilton, K.D. Nutrient deprivation increases vulnerability of endothelial cells to proinflammatory insults. *Free Radic. Biol. Med.* **2014**, *67*, 408–415. [CrossRef] [PubMed]

25. Moore, R.B.; Xiao, Z.; Tulip, J.; Chapman, J.D. A comparison of susceptibility to photodynamic treatment between endothelial and tumor cells in vitro and in vivo. *Photodiagn. Photodyn. Ther.* **2007**, *4*, 160–169. [CrossRef]

26. Devarajan, E.; Sahin, A.A.; Chen, J.S.; Krishnamurthy, R.R.; Aggarwal, N.; Brun, A.M.; Sapino, A.; Zhang, F.; Sharma, D.; Yang, X.H.; et al. Down-regulation of caspase 3 in breast cancer: A possible mechanism for chemoresistance. *Oncogene* **2002**, *21*, 8843–8851. [CrossRef]

27. Essmann, F.; Engels, I.H.; Totzke, G.; Schulze-Osthoff, K.; Jänicke, R.U. Apoptosis resistance of MCF-7 breast carcinoma cells to ionizing radiation is independent of p53 and cell cycle control but caused by the lack of caspase-3 and a caffeine-inhibitable event. *Cancer Res.* **2004**, *64*, 7065–7072. [CrossRef]

28. Jänicke, R.U.; Engels, I.H.; Dunkern, T.; Kaina, B.; Schulze-Osthoff, K.; Porter, A.G. Ionizing radiation but not anticancer drugs causes cell cycle arrest and failure to activate the mitochondrial death pathway in MCF-7 breast carcinoma cells. *Oncogene* **2001**, *20*, 5043–5053. [CrossRef]

29. Jänicke, R.U.; Sprengart, M.L.; Wati, M.R.; Porter, A.G. Caspase-3 is required for DNA fragmentation and morphological changes associated with apoptosis. *J. Biol. Chem.* **1998**, *273*, 9357–9360. [CrossRef]

30. Jänicke, R.U. MCF-7 breast carcinoma cells do not express caspase-3. *Breast Cancer Res. Treat.* **2009**, *117*, 219–221. [CrossRef]

31. Yang, X.H.; Sladek, T.L.; Liu, X.; Butler, B.R.; Froelich, C.J.; Thor, A.D. Reconstitution of caspase 3 sensitizes MCF-7 breast cancer cells to doxorubicin- and etoposide-induced apoptosis. *Cancer Res.* **2001**, *61*, 348–354. [PubMed]

32. Yang, S.; Zhou, Q.; Yang, X. Caspase-3 status is a determinant of the differential responses to genistein between MDA-MB-231 and MCF-7 breast cancer cells. *Biochim. Biophys. Acta-Mol. Cell Res.* **2007**, *1773*, 903–911. [CrossRef] [PubMed]

33. Kessel, D.; Luo, Y.; Deng, Y.; Chang, C.K. The role of subcellular localization in initiation of apoptosis by photodynamic therapy. *Photochem. Photobiol.* **1997**, *65*, 422–426. [CrossRef] [PubMed]

34. Kessel, D.; Luo, Y. Mitochondrial photodamage and PDT-induced apoptosis. *J. Photochem. Photobiol. B Biol.* **1998**, *42*, 89–95. [CrossRef]

35. Schnitzer, J.E. Update on the cellular and molecular basis of capillary permeability. *Trends Cardiovasc. Med.* **1993**, *3*, 124–130. [CrossRef]

36. Prinsen, B.H.C.M.T.; De Sain-Van Der Velden, M.G.M. Albumin turnover: Experimental approach and its application in health and renal diseases. *Clin. Chim. Acta* **2004**, *347*, 1–14. [CrossRef]

37. Soeters, P.B.; Wolfe, R.R.; Shenkin, A. Hypoalbuminemia: Pathogenesis and Clinical Significance. *J. Parenter. Enter. Nutr.* **2019**, *43*, 181–193. [CrossRef]

38. Scherz, A.; Salomon, Y.; Brandis, A.; Scheer, H. Palladium-Substituted Bacteriochlorophyll Derivatives and Use Thereof. International Patent Application No. PCT/IL1999/000673, 15 June 2000.

39. Clement, M.; Daniel, G.; Trelles, M. Optimising the design of a broad-band light source for the treatment of skin. *J. Cosmet. Laser Ther.* **2005**, *7*, 177–189. [CrossRef]

40. Koudinova, N.V.; Pinthus, J.H.; Brandis, A.; Brenner, O.; Bendel, P.; Ramon, J.; Eshhar, Z.; Scherz, A.; Salomon, Y. Photodynamic therapy with Pd-Bacteriopheophorbide (TOOKAD): Successful in vivo treatment of human prostatic small cell carcinoma xenografts. *Int. J. Cancer* **2003**, *104*, 782–789. [CrossRef]

41. Mazor, O.; Brandis, A.; Plaks, V.; Neumark, E.; Rosenbach-Belkin, V.; Salomon, Y.; Scherz, A. WST11, A Novel Water-soluble Bacteriochlorophyll Derivative; Cellular Uptake, Pharmacokinetics, Biodistribution and Vascular-targeted Photodynamic Activity Using Melanoma Tumors as a Model. *Photochem. Photobiol.* **2005**, *81*, 342. [CrossRef]

42. Szczygieł, M.; Urbańska, K.; Jurecka, P.; Stawoska, I.; Stochel, G.; Fiedor, L. Central metal determines pharmacokinetics of chlorophyll-derived xenobiotics. *J. Med. Chem.* **2008**, *51*, 4412–4418. [CrossRef]

43. Vakrat-Haglili, Y.; Weiner, L.; Brumfeld, V.; Brandis, A.; Salomon, Y.; Mcllroy, B.; Wilson, B.C.; Pawlak, A.; Rozanowska, M.; Sarna, T.; et al. The Microenvironment Effect on the Generation of Reactive Oxygen Species by Pd−Bacteriopheophorbide. *J. Am. Chem. Soc.* **2005**, *127*, 6487–6497. [CrossRef] [PubMed]

44. Ashur, I.; Goldschmidt, R.; Pinkas, I.; Salomon, Y.; Szewczyk, G.; Sarna, T.; Scherz, A. Photocatalytic generation of oxygen radicals by the water-soluble bacteriochlorophyll derivative WST1l, noncovalently bound to serum albumin. *J. Phys. Chem. A* **2009**, *113*, 8027–8037. [CrossRef]

45. Gerola, A.P.; Santana, A.; França, P.B.; Tsubone, T.M.; De Oliveira, H.P.M.; Caetano, W.; Kimura, E.; Hioka, N. Effects of metal and the phytyl chain on chlorophyll derivatives: Physicochemical evaluation for photodynamic inactivation of microorganisms. *Photochem. Photobiol.* **2011**, *87*, 884–894. [CrossRef] [PubMed]

46. Szczygieł, M. *Characteristics of Metallochlorophyllides Interactions with Tumor Cells and Animal Organism in the Context of Photodynamic Therapy*; Jagiellonian University: Kraków, Poland, 2009.

47. Handoko, Y.A.; Rondonuwu, F.S.; Limantara, L. The Photosensitizer Stabilities of Tookad® on Aggregation, Acidification, and Day-light Irradiation. *Procedia Chem.* **2015**, *14*, 474–483. [CrossRef]

48. Sułkowski, L.; Matyja, A.; Osuch, C.; Matyja, M. Stability of spectrofluorimetric spectra of hematoporphyrin–serum albumin complexes: In Vitro study. *Arch. Med. Sci.-Civiliz. Dis.* **2021**, *6*, 18–21. [CrossRef]

49. Weersink, R.A.; Bogaards, A.; Gertner, M.; Davidson, S.R.H.; Zhang, K.; Netchev, G.; Trachtenberg, J.; Wilson, B.C. Techniques for delivery and monitoring of TOOKAD (WST09)-mediated photodynamic therapy of the prostate: Clinical experience and practicalities. *J. Photochem. Photobiol. B Biol.* **2005**, *79*, 211–222. [CrossRef]

50. Yang, C.H.; Huang, K.S.; Wang, Y.T.; Shaw, J.F. A review of bacteriochlorophyllides: Chemical structures and applications. *Molecules* **2021**, *26*, 1293. [CrossRef]

51. *Origin*, Version 2021; OriginLab Corporation: Northampton, MA, USA, 2021.

52. Schindelin, J.; Arganda-Carreras, I.; Frise, E.; Kaynig, V.; Longair, M.; Pietzsch, T.; Preibisch, S.; Rueden, C.; Saalfeld, S.; Schmid, B.; et al. Fiji: An open-source platform for biological-image analysis. *Nat. Methods* **2012**, *9*, 676–682. [CrossRef]

53. Bolte, S.; Cordelières, F.P. A guided tour into subcellular colocalization analysis in light microscopy. *J. Microsc.* **2006**, *224*, 213–232. [CrossRef]

54. Castillo-Hair, S.M.; Sexton, J.T.; Landry, B.P.; Olson, E.J.; Igoshin, O.A.; Tabor, J.J. FlowCal: A User-Friendly, Open Source Software Tool for Automatically Converting Flow Cytometry Data from Arbitrary to Calibrated Units. *ACS Synth. Biol.* **2016**, *5*, 774–780. [CrossRef] [PubMed]

Zinc-substituted pheophorbide a is a safe and efficient antivascular photodynamic agent

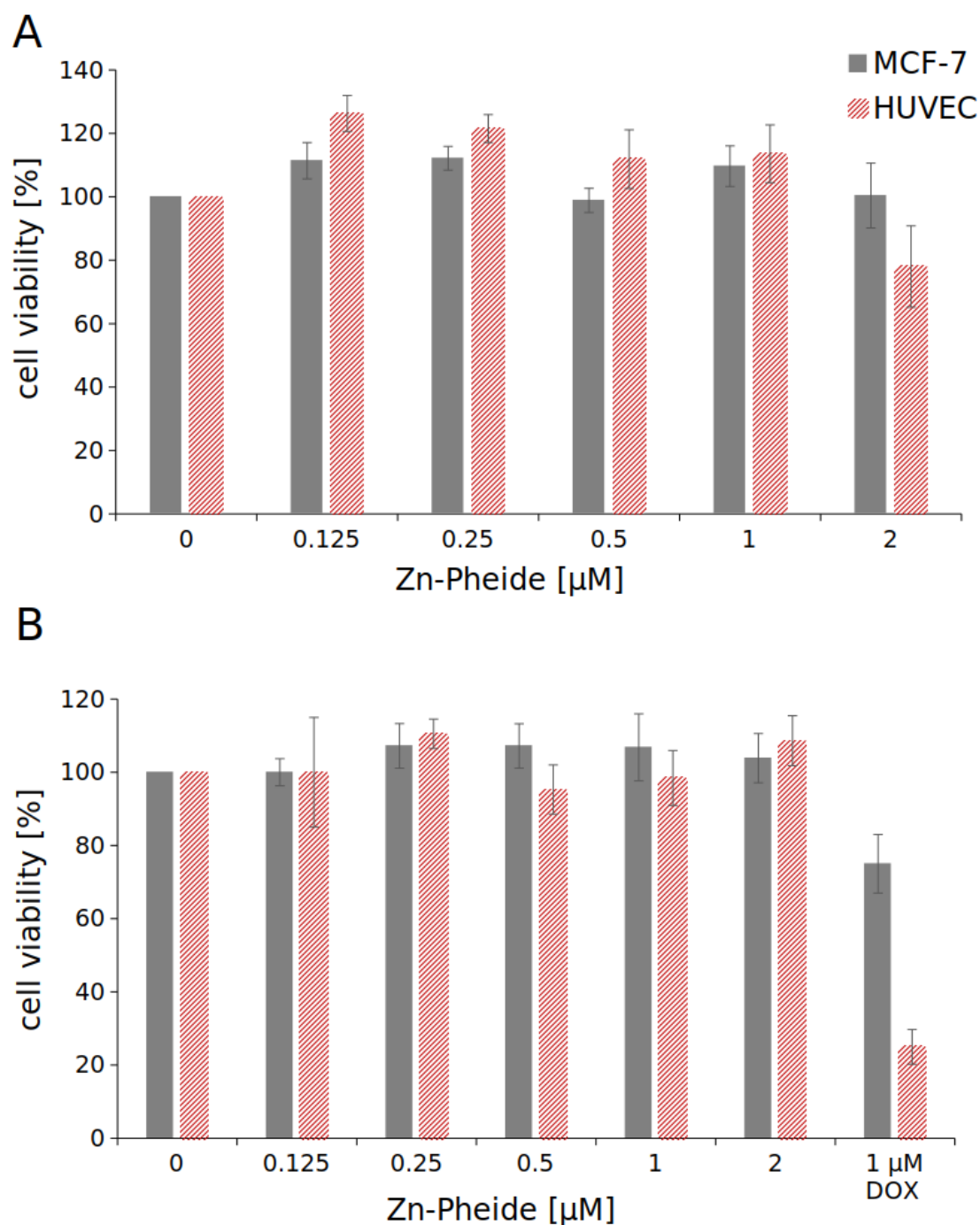Milena J. Szafraniec, Monika Toporkiewicz, Andrzej Gamian

Figure S1. Dark cytotoxicity of Zn-Pheide against MCF-7 and HUVEC cells in the absence of albumin (A) and in the presence of 250 µM HSA (B). Cells treated with appropriate concentration of DMSO without the PS served as negative controls and were assigned 100% viability. Cells treated with doxorubicin (DOX) at a concentration of 1 µM served as positive controls. Analysis performed by MTT assay after 3 h of incubation. The results are shown as mean ± SD, n= 3.
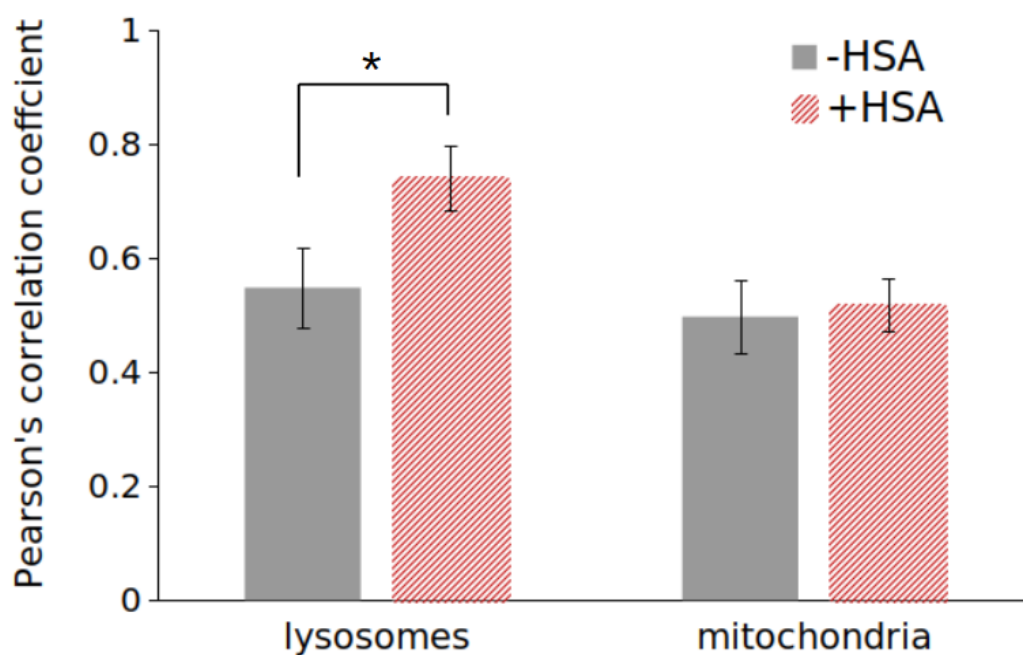
Figure S2. Correlation analysis of Zn-Pheide colocalization in lysosomes and mitochondria in the absence and presence of HSA. The graph shows the Pearson's correlation coefficients determined with the JACoP plugin from the ImageJ software. Significant differences between HSA-free and HSA-containing samples were indicated by asterisk (*), $p < 0.05$.
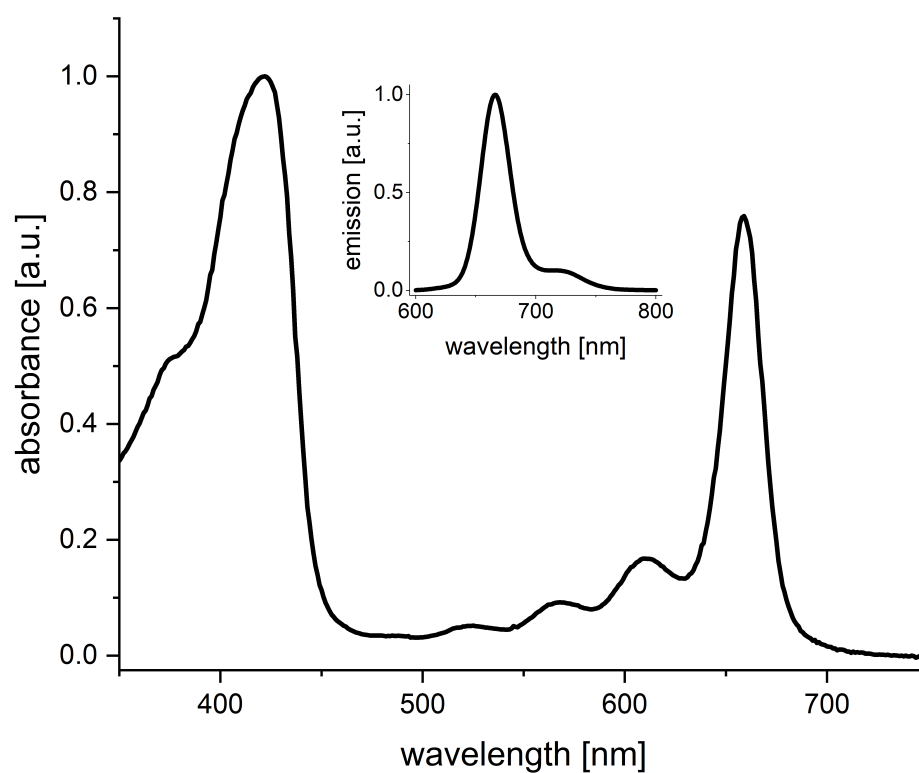

Figure S3. Absorption and emission (inset) spectra of Zn-Pheide recorded in ethanol. The emission spectrum was measured after excitation in the Soret band (430 nm).
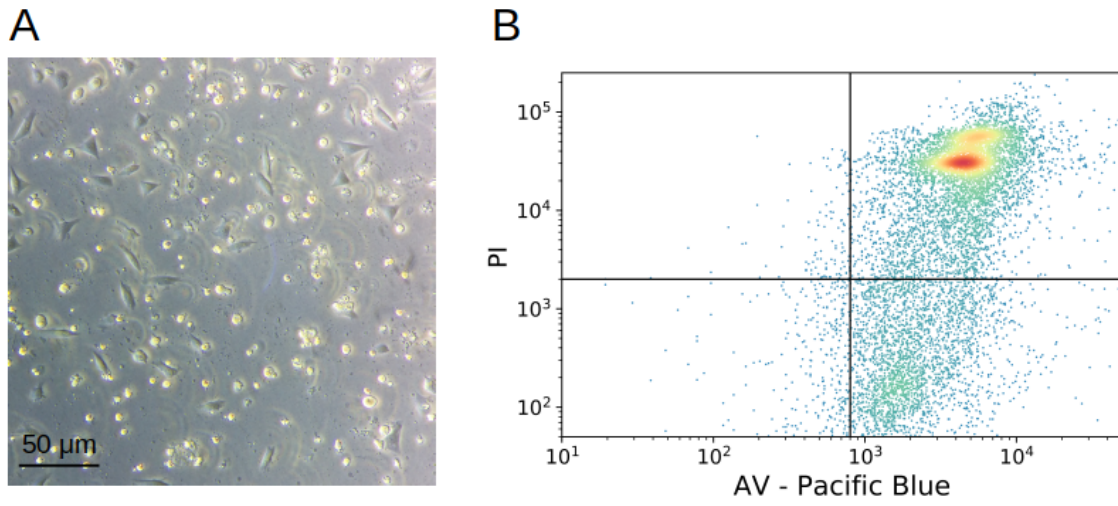
Figure S4. Positive controls included in the experiments: (A) HUVEC cells treated with 1 μM doxorubicin for 24 h, (B) Annexin V/PI staining of heat-treated HUVEC cells (incubation at 55°C for 20 min).